Title
Inorganic Nanostructures for Energy Storage Applications

Author
Kim, Hyungseok

Publication Date
2015

Peer reviewed|Thesis/dissertation

UNIVERSITY OF CALIFORNIA

Los Angeles

Inorganic Nanostructures for Energy Storage Applications

A dissertation submitted in partial satisfaction of the requirements for the degree Doctor of Philosophy in Materials Science and Engineering

by

Hyungseok Kim

2015

ABSTRACT OF THE DISSERTATION

Inorganic Nanostructures for Energy Storage Applications

by

Hyungseok Kim

Doctor of Philosophy in Materials Science and Engineering

University of California, Los Angeles, 2015

Professor Bruce Dunn, Chair

Pseudocapacitive energy storage is a promising energy storage mechanism which can lead to both high energy density and high power density. Based on current lithium ion battery technology, achieving high rate energy storage with high capacity is a very important challenge and pseudocapacitive materials are good candidates to solve this problem. The first part of this dissertation addresses two material systems for pseudocapacitive energy storages. The realization of pseudocapacitance in these materials is done by changing their physical properties. In the first system, MoO_3, we created oxygen vacancies to modify the electrically insulating nature of MoO_3. The effects of oxygen vacancies on the structural and electrochemical properties are examined. In the second system, MoO_2, we synthesized nanoparticles to overcome diffusion limitations in the charge storage of bulk MoO_2. The slow kinetics in bulk materials are generally from its size

as well as from the phase transition during lithium insertion. Size-dependent electrochemical behavior in MoO_2 are investigated and the use of reduced graphene oxide to solve the surface oxidation problem is demonstrated. The last part of the dissertation involves sodium ion batteries. Sodium ion batteries are promising not only because sodium ions have similar electrochemical intercalation properties as those of lithium, but also sodium is one of the most abundant elements on earth. However, sodium has certain intrinsic limitations such as being less electropositive than lithium and slow kinetics from its relatively large ion size. These features have limited the development of sodium ion batteries. In order to overcome these intrinsic limitations, we synthesized $Na_{1.5}VPO_{4.8}F_{0.7}$ nanoparticles and the synthesis and electrochemical properties of this material were examined.

The dissertation of Hyungseok Kim is approved.

Sarah Tolbert

Vidvuds Ozolins

Laurent Pilon

Bruce Dunn, Committee Chair

University of California, Los Angeles

2015

To my Parents, Chul-Ho Kim and Im-Soon Wang and

my Wife, Hye-Sung Yun and my Daughter, Irene Kim

TABLE OF CONTENTS

LIST OF FIGURES

LIST OF TABLES

ACKNOWLEDGEMENT

Firstly, I would like to express my sincere gratitude to my advisor Professor Bruce Dunn for his wonderful mentorship over the past 5 years. I was very new to the field of electrochemistry and energy storage when I joined the group and his continuous and generous support during my Ph.D study enable to complete several projects. His guidance helped me in all the time of research and writing of this thesis. I could not have imagined having a better advisor and mentor for my Ph.D study.

Through Prof. Dunn I have had the chance to collaborate with a number of faculty members at UCLA, including my dissertation committee: Prof. Vidvuds Ozolins, Prof. Sarah H. Tolbert, and Prof. Laurent Pilon. Thank you for your time and assistance in evaluating my dissertation.

I thank my current and previous labmates in the Dunn Lab who helped make this research possible: Dr. Jonathan Fang, Dr. Emilie Perre, Dr. Ryan Maloney Dr. Enrico Della Gaspera, Dr.Jongwoung (Jason) Kim, Dr. Daniel Membreno, Dr. Guillaume Muller, Dr. Esther Lan, Dr. Xavier Petrissans, Dr. Peter Malati, Dr. Nicolas Cirigliano, Dr. Veronica Augustyn, Dr. Wade Richardson, Dr. Danielle Casillas, Dr. Leland Smith, Jesse Ko, Rita Blaik, Chun-Han (Matt) Lai, Joy Trujillo, Janet Hur, Kumpei Kobayashi, David Ashby, Dean Cheikh, Dan Wilkinson, Jonathan Lau, Andrew Siordia, and Nick Ware. Dr. Emilie Perre, Dr. Enrico Della Gaspera, and Dr. Jongwoung (Jason) Kim taught the basics of inorganic synthesis and electrochemistry during my first and second year. Dr. Guillaume Muller and Dr. Xavier Petrissans worked with me and they showed great passion to their research and I could learn those attitude from them.

I would also like to my collaborators in other group: John Cook and Hao Lin. John Cook have worked with me in several projects and without his supportive help, I could not make my research projects complete. Hao Lin did significant contribution to reduced MoO_{3-x} work with his great simulation skill.

I cannot thank enough to my family in South Korea. My parents instilled in me that endless learning and hardworking were great things. Their endless support and prays always give me a strength and confidence. I am profoundly indebted for my wife's devotion for supporting me during my study. She was a happy virus that makes me feel happy every time. My little baby, Irene Kim, also gave me great happiness with her beautiful smile.

VITA

1999 - 2006	B.S in Materials Science and Engineering Yonsei University, Seoul, South Korea
2006 - 2009	M.S in Materials Science and Engineering Yonsei University, Seoul, South Korea
2010	Research Associate Korea Institute of Science and Technology Seoul, South Korea
2010 – 2015	Graduate Student Researcher Department of Materials Science and Engineering University of California, Los Angeles

PUBLICATIONS AND PRESENTATIONS

1. J. B. Cook*, H.-S. Kim*, Y. Yan, J. S. Ko, B. Dunn, S. H. Tolbert "Mesoporous MoS_2 as a transition metal dichalcogenide exhibiting pseudocapacitive Li and Na-ion charge storage" (*equal contribution) *Adv. Energy Mater*. **2015**, Submitted,

2. J. B. Cook, H.-S. Kim, Y. Yan, J. Ko, B. Dunn, S. H. Tolbert, "Nanoporous MoS_2 as an electrode material exhibiting high levels of pseudocapacitive charge storage with both Li and Na-ions" *ECS meeting*, Jul **2015**, Glasgow, Scotland **(Poster presentation)**

3. H.-S. Kim, J. Cook, S. H. Tolbert, B. Dunn, "The development of pseudocapacitive properties in nanosized-MoO_2" *J. Electrochem. Soc.* **2015**, 162, A5083

4. G. Muller, J. Cook, H.-S. Kim, S. H. Tolbert, B. Dunn, "High performance pseudocapacitor based on 2D layered metal chalcogenide nanocrystals" *Nano Lett.* **2015**, 15, 1911

5. J.-M. Park, H.-W. Jung, Y. W. Chang, H.-S. Kim, M.-J. Kang, J.-C. Pyun, "Chemiluminescence lateral flow immunoassay based on Pt nanoparticle with peroxidase activity" *Anal. Chim. Acta* **2015**, 853, 360

6. H.-S. Kim, J. B. Cook, L. Smith, S. H. Tolbert, B. Dunn, "Structural and pseudocapacitive properties of reduced α-MoO_{3-x}" *MRS Spring*, Apr **2014**, San Francisco, CA **(Oral presentation)**

7. H.-S. Kim, J. Cho, S.-Y. Jang, Y.-W. Song, "Nonlinearity-preserved graphene/PVAc composite in optical deposition for fiber mode-locked lasers" *OFC/NFOEC*, Mar **2011**, Los Angeles, CA **(Oral presentation)**

8. H.-S. Kim, J. Cho, S.-Y. Jang, Y.-W. Song, "Deformation-immunized optical deposition of graphene for ultrafast pulsed lasers" *Appl. Phys. Lett.* **2011**, 98, 021104

9. H.-S. Kim, Y. M. Jang, J. H. Lee, Y.-W. Song "Physically exfoliated graphene for nonlinear pulse formation of fiber lasers" *5th Advanced Materials and Nanotechnology (AMN)*, Feb **2011**, Wellington, New Zealand **(Poster presentation)**

10. Y. M. Jang, H.-S. Kim, J. H. Lee, Y.-W. Song, "Multilayered graphene efficiently formed by mechanical exfoliation for nonlinear saturable absorbers in fiber mode-locked lasers", *Appl. Phys. Lett.* **2010**, 97, 211102

11. H.-S. Kim, H. Ko, M.-J. Kang, J.-C. Pyun, "Highly sensitive rapid test kit with chemiluminescence signal bands", *Biochip J.* **2010**, 4, 155

12. H.-S. Kim, J.-C. Pyun, "Hyper sensitive strip test with chemi-luminescence signal band", *Procedia Chem.* **2009**, 1, 1043

13. H.-S. Kim, J.-C. Pyun, "Hyper sensitive rapid test with chemiluminescence signal band" *Eurosensors*, Sep **2009**, Lausanne, Switzerland **(Poster presentation)**

14. H.-S. Kim, J.-C. Pyun, "CdS_xSe_{1-x} nanowire photosensor for the detection of chemiluminescence by luminol and horseradish peroxidase" *NanoBio Seoul*, Oct **2008**, Seoul, Korea **(Poster presentation)**

15. H.-S. Kim, J. G. Park, J. H. Park, J.-C. Pyun, "Synthesis of CdS_xSe_{1-x} alloy nanowires and fabrication of photosensor" *Korea Ceramic Society Spring Symposium*, Apr **2008**, Seoul, Korea **(Oral presentation)**

16. H.-S. Kim, H.-M. Kim, "Bio-interactive strategies on prosthesis surfaces and beyond" *KIST Europe-Yonsei University Nano Bio Workshop*, Sep **2006**, Saarbrucken, Germany **(Oral presentation**

Chapter 1. Introduction and objectives

Global warming and decreasing fossil fuel reserves coupled with increasing demand is forcing us to develop sustainable and renewable energy production and storage technologies[3]. In order to store electrical energy produced by solar or wind power, the development of grid scale energy storage technology is crucial. In addition, to meet the demand of safety and long life time, energy storage devices for consumer electronics as well as for long range electrical vehicles, require the development of new technology for rechargeable electrochemical energy storage (EES) systems. Several energy storage technologies have been developed, but only a few of them are commercialized. The most successful EES system is rechargeable lithium ions batteries (LIBs). LIBs have been used in a wide range of applications from portable electronic systems, to electrical vehicles, and even grid applications because LIBs offer design capabilities with its simple structure as well as high energy density. However, to meet the increasing power consumption in electronic systems and to enable electrical vehicles with ranges of 500 km, the energy density of LIBs needs to be improved. Another problem with LIB technology is low power density due to charge storage mechanisms that rely on solid-state diffusion. (Figure 1.1) Although the development of quick charging technology enables charging in a short time, it decreases the cycle life of LIBs. Much effort has been dedicated to the development of high power LIBs without compromising energy density. Electrochemical capacitors are a promising class of energy storage materials with high power and long term stability. As shown Figure 1.1, electrochemical capacitors (ECs,), also known as 'supercapacitors', are bridging the gap between conventional capacitors and LIBs. Carbon based ECs have higher power density and better long term cyclability (>100,000 cycles), but because the stored charge is surface limited, the energy density is low and substantially less than that of Li-ion batteries. However, pseudocapacitive

energy storage combines the attractive properties of batteries and ECs, potentially leading to energy storage materials with both high power density and high energy density. This disruptive technology has attracted considerable interest from both academia and industry. High power density combined with energy densities near that of batteries (~ 250 Wh/Kg) can be realized by carefully engineering material compositions and specific nanoscale architecture. Pseudocapacitive charge storage consists of faradaic reactions at the surface or near the surface of nanostructured materials. Since the solid-state diffusion distances are reduced significantly, the reaction rates are increased significantly. The development of these properties in several materials has been explored through a variety of techniques which are described in the first and second material systems in this dissertation.

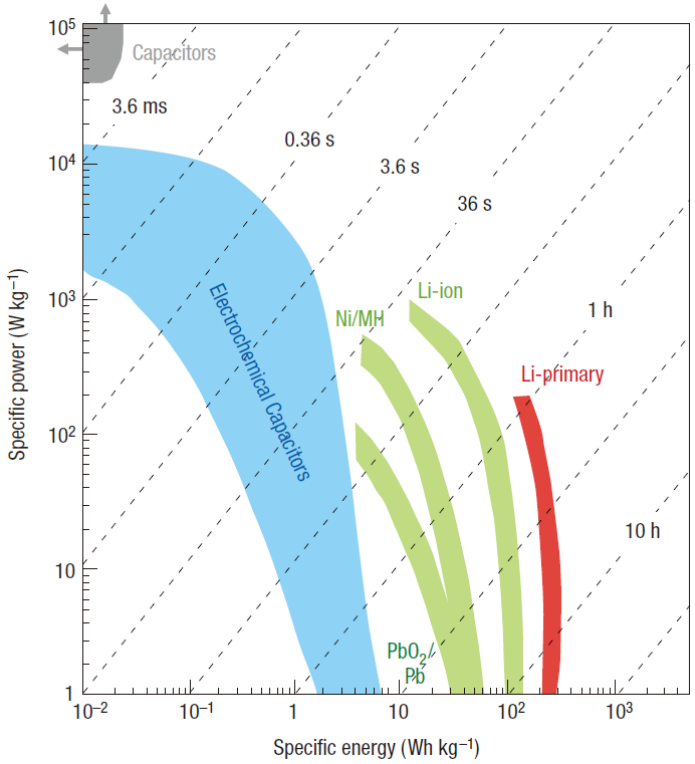

Figure 1.1. Ragone plot showing specific power vs. specific energy density for various electrical energy storage systems[1].

The first system to be discussed is orthorhombic MoO_3, which has been studied extensively as a battery material. In this research, we created oxygen vacancies to increase the low electrical conductivity of this material. Non-stoichiometric MoO_3 was synthesized by one-step microwave hydrothermal synthesis. The effects of oxygen defects on the MoO_3 structure and the resulting pseudocapacitive behavior were studied by using various techniques.

The second system discussed in this dissertation is monoclinic MoO_2, a metallic conductor, which has been extensively studied as a conversion-type lithium ion battery anode. In this study, we synthesized MoO_2 nanoparticles to suppress the phase transformation during lithium insertion and de-insertion. The electrochemical properties of hydrothermally synthesized MoO_2 nanoparticles were investigated, and compared with the electrochemical properties of micron-sized MoO_2. We found that surface oxidation reduced the electronic conductivity in this reduced metal oxide which hinders fast kinetics. The surface resistance was addressed by anchoring the MoO_2 to reduced graphene oxide (RGO), which served as a conductive medium. Synthetic details and electrochemical performance of thin and thick electrodes of MoO_2-RGO composites were investigated.

The third part of this dissertation involves the synthesis of cathode materials for sodium ion batteries. Sodium ion batteries (SIBs) have been studied since 1970s, and the abundance of materials resources and similarity with lithium makes this system attractive to replace current LIBs technology[2]. However, due to intrinsic limitations such as a lower electropositive potential and slow kinetics because of ion size larger than lithium ions, SIBs have been considered mostly for grid storage applications. In order to overcome these limitations, we decided to investigate $Na_{1.5}VPO_{4.8}F_{0.7}$, a system which is attractive for its high redox potential (~ 3.8 V vs. Na/Na^+). In order to improve the kinetics of this material$Na_{1.5}VPO_{4.8}F_{0.7}$ nanoparticles were synthesized. We

used a two-step process in which a modified Pechini method was used to form the phase while hydrothermal synthesis served to incorporate fluorine ions and decrease the particle sizes. The structural and electrochemical properties of $Na_{1.5}VPO_{4.8}F_{0.7}$ nanoparticles were investigated and a full cell was fabricated with an Sb anode to evaluate device performance.

Chapter 2. Pseudocapactive properties of reduced MoO_{3-x}

Chapter 2.1. Introduction

Electrochemical energy storage (EES) continues to be an exceedingly active field for research and development because of application areas ranging from portable electronics to electrification of transportation to coupling with renewable energy sources for powering the electrical grid[5]. Both batteries and electrochemical capacitors involve electrochemical mechanisms, albeit different ones, which determine their respective energy storage and power characteristics[6]. Electrical double layer capacitors (EDLCs), also known as supercapacitors, offer higher power, shorter charging times and longer cycle life than lithium-ion batteries. The low energy density of carbon-based EDLCs, however, limits this technology. To improve upon energy density, researchers have begun to investigate another mechanism for capacitive energy storage known as pseudocapacitance where charge storage occurs via Faradaic charge transfer at the surface or near the surface of the material[7]. The alluring feature for pseudocapacitance is the prospect of increasing energy density without compromising the high power or cycle life of carbon-based EDLCs. A number of transition metal oxides, both in aqueous and non-aqueous electrolytes, have been shown to exhibit pseudocapacitance or at least to exhibit electrochemical signatures which are representative of pseudocapacitance. The latter often occurs with nanoscale materials because of short diffusion distances[8]. Thus in this chapter our study is focused on the development of pseudocapacitive properties to achieve high energy density and high power density. For this, we choose orthorhombic MoO_3 as a first model system because of its high theoretical capacity and layered structure.

Chapter 2.2. Technical background

Chapter 2.2.1. Intercalation pseudocapacitance

Pseudocapacitance was demonstrated through the discovery that hydrated RuO_2[9] and MnO_2[10] undergo faradaic surface reactions. More recently, Tolbert and Dunn et al. have described a related process called 'intercalation pseudocapacitance'[11, 12, 13]. In this process, there is the insertion of ions into the van der Waals (vdWs) gaps or 1d-tunnels within a metal oxide host. However, rather than being diffusion controlled, the transport of these ions in the solid appear capacitive. Most battery electrode materials that rely on this insertion type mechanism undergo a phase change which is typically a slow process. Such phase transitions are generally a negative occurrence in batteries and can be responsible for poor reversibility especially at high rates. However, in certain cases ion diffusion into the bulk is quite fast, occurring without a phase transformation and leading to charge storage which is capacitive in nature. Although this process involves redox reactions as occurs in a battery, the electrochemical features are different as follows[13]: (1) The peaks are generally broad and peak separations are very small in cyclic voltammetry experiments and (2) The voltage hysteresis is small with sloped voltage profiles in galvanostatic charge/discharge profiles. Intercalation pseudocapacitance was first demonstrated in the previous study[11] of mesoporous crystalline α-MoO_3. In this study a crystalline α-MoO_3 stored more than two times higher capacity than amorphous α-MoO_3. This result clearly showed that crystalline α-MoO_3 stores charges in the bulk as well as on the surface. In addition kinetic analysis showed that almost 70 % of stored charge was capacitive in crystalline α-MoO_3. This fast rate capability mainly came from the nanoscale architecture of mesoporous film providing short diffusion pathway for electrons and ions and more importantly iso-oriented nature of material. Orthorhombic Nb_2O_5 (T-Nb_2O_5) showed similar intercalation pseudocapacitive

behavior[12]. Although T-Nb_2O_5 does not have vdWs gaps, the structure can be described as a tunnel structure. The T-Nb_2O_5 showed high rate capability without phase transformation. The capacity of 430 F/g was achieved in a charging time of one minute for the thin film sample. Even with thick electrodes[14] (40 μm-thick, 1.2 mg/cm^2) the material could store 380 F/g. As shown in the above examples, we can develop intercalation pseudocapacitive properties by modify physical properties such as the crystal structure and size of materials.

Chapter 2.2.2. Molybdenum trioxide (MoO_3)

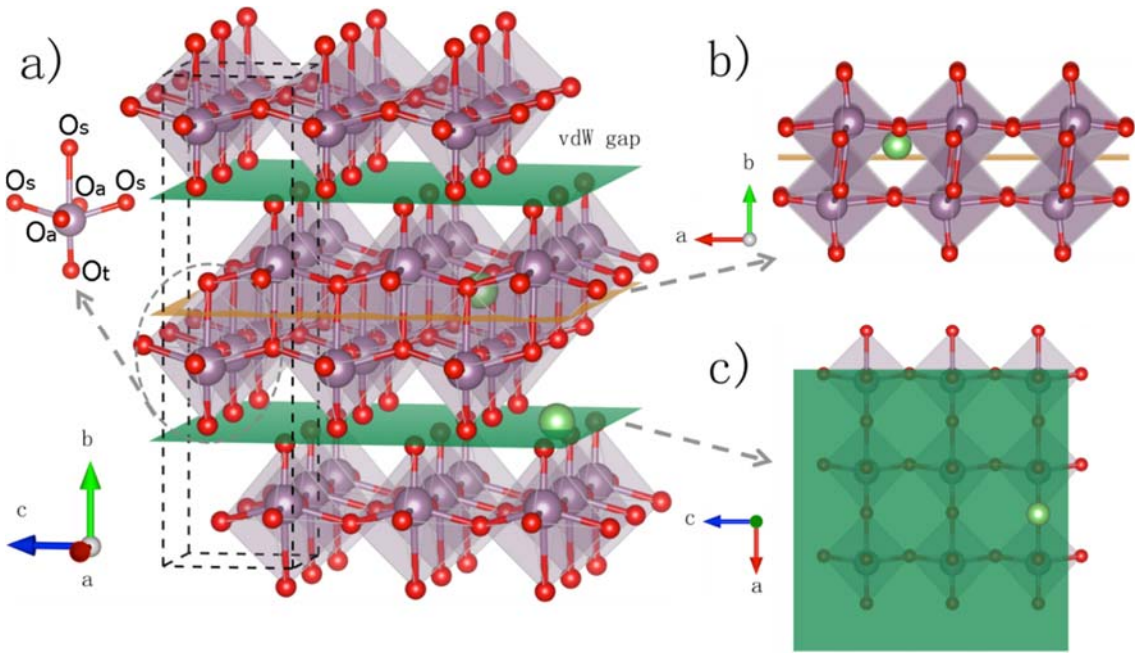

Figure 2.1. (a) Structure of the orthorhombic α-MoO_3 (b) the intralayers site and (c) the interlayer site for lithium intercalation (Figures from Hao Lin)

MoO_3 is has been well investigated for various applications. It has been used as a catalyst[15], and as a component in photochromic and electrochromic devices[16] , gas sensors[17], and energy storage applications[11, 18, 19, 20]. MoO_3 has three polymorphs: hexagonal MoO_3, monoclinic

MoO_3, and orthorhombic MoO_3 (α-MoO_3). α-MoO_3 is thermodynamically the most stable phase[20]. Thus, α-MoO_3 has been an attractive cathode material for lithium intercalation with its layered structure and it can achieve a theoretical capacity of 1080 C/g from the insertion of 1.5 moles of lithium ions per mole of Mo into the van der Waals (vdWs) gap[21, 22, 23]. The crystal structure of α-MoO_3 (shown in Figure 2.1) belongs to the orthorhombic *Pbnm* space group. This structural framework consists of a bilayer network of edge-sharing MoO_6 octahedra (shown in grey in Figure 2.1). The bilayers are stacked along the *b* direction and bonded with adjacent layers by van der Waals forces. There are three types of oxygen anions in the structure. The first type, called the "terminal oxygen O_t", results in a Mo-O_t bond which points perpendicular to the van der Waals gap (shown in green in Figure 2.1). The second type, labelled as O_a, forms asymmetric bonds with two Mo ions in the *a* direction, while the third type, referred to as "symmetric oxygen (O_s)", has three-fold symmetry which leads to the formation of two short bonds with two Mo ions in [001] direction and one longer bond with a Mo ions in [010] direction. However, α-MoO_3 has low electronic conductivity and undergoes an irreversible structural change during lithiation. These limitations lead to slow kinetics and poor long term cycling[21, 24]. In order to overcome these problems, several approaches have been explored including pre-lithiation of MoO_3 and ammonizing MoO_3[25, 26]. Pre-lithiation of MoO_3 increases the vdWs gap thereby leading to better electrochemical cycling stability at the expense of specific capacity because of its reduced oxidation state[25]. Ammonolyzed MoO_3 shows higher electronic conductivity than MoO_3, cycling for 50 cycles at 200 mAh/g at 1C. The capacity, however, decreased significantly at increased charging rates; at 10C the capacity fell below 75 mAh/g[26]. These studies suggest that while widening the vdWs gap and increasing the intrinsic electronic conductivity of MoO_3 may provide partial solutions to the limitations of MoO_3, the synthesis of

these materials requires several additional processing steps. Furthermore, better electrochemical stability and high rate capability are still necessary for an effective electrode material.

Chapter 2.2.3. The effect of oxygen vacancies in oxide materials

One viable route for overcoming the low electrical conductivity of MoO_3 is through the introduction of oxygen vacancies[27, 28]. With transition metal oxides, this approach has been shown to improve the electronic conductivity by increasing the polaron carrier concentration[29]. Oxygen vacancies can act as shallow donors and thereby increase the carrier concentration[30]. There have been only a limited number of studies which explore the effect of oxygen non-stoichiometry and enhanced electronic conduction on energy storage properties. In a study of TiO_2 nanotubes[31], hydrogenated TiO_2, which contains oxygen vacancies, exhibited significantly higher areal capacity (3.24 mF cm^{-2}) than untreated TiO_2 nanotubes (0.026 mFcm^{-2}) or air annealed TiO_2 nanotubes (0.08 mF cm^{-2}). The hydrogenated material also displayed good long-term cycling (3.1 % capacitance loss after 10,000 cycles) as a result of the improved electrical conductivity. Oxygen vacancies in nanoparticles of TiO_2,[32] produced by thermal treatment in a reducing atmosphere (5% H_2/95% Ar) led to materials whose capacity at high rates was significantly better than stoichiometric TiO_2 nanoparticles (130 mAh/g vs. 27 mAh/g at 10C). In prior research carried out oxygen deficient on MoO_3, the presence of oxygen vacancies lead to an increase the interlayer distance.[29] In addition, Mai et al. showed that interlayer expansion in lithiated MoO_3 exhibited improved electrochemical stability[25].

Chapter 2.3. Experimental

2.3.1. Reduced MoO_{3-x} synthesis

Reduced MoO_{3-x} - Reduced MoO_{3-x} was synthesized by microwave hydrothermal synthesis. Anhydrous $MoCl_5$ (270 mg, Strem Chemicals) was dissolved in ethanol (5ml) and deionized (DI) water (15 ml) and 0.25 ml nitric acid (HNO_3, 70%, Sigma-Aldrich) was added in this solution with stirring. The prepared solution was transferred into the 25 ml size microwave reaction vessel and placed in the microwave synthesis system (Discover SP, CEM Corporation). The sample was heated with 200 W up to 180 °C and kept for 15 min at this temperature. During the synthesis, the pressure was maintained at around 180 psi. The resulting deep blue colored solution was centrifuged (5000 rpm for 5 min) and washed 3 times with DI water and ethanol and dried in the vacuum for 24 hr. For the preparation of partly reduced and fully oxidized sample, as synthesized powders were annealed at 150 °C for 2 hr and at 400 °C for 1 hr, respectively.

2.3.2. Material characterization

Basic characterization - The phase of each MoO_3 sample was identified by X-ray diffraction (Rigaku Miniflex II) using Cu–Kα (λ=1.54 Å) radiation. Brunauer-Emmett-Teller (BET) surface area measurements were performed by using nitrogen adsorption isotherms at 77 K using a gas adsorption analyzer (Micromeritics ASAP 2010). The particle size and shape of MoO_3 were characterized by transmission electron microscopy (TEM; T12, FEI) and scanning electron microscopy (SEM; Nova NanoSEM 230, FEI).

Powder XRD for peak position shift - Powder X-ray diffraction was performed in a PANalytical X'Pert Pro operating with Cu Kα (λ = 1.5418 Å) using a 0.008° step size, a voltage

of 45kV, and a current of 40mA. Samples were prepared from a mixture of MoO_3 and 9.1% (w/w) standard silicon. After the composite was well mixed in an agate mortar, and a thin layer was packed onto a quartz slide for measurement. The silicon (111) reflection at 28.44° 2Θ and the (220) reflection at 47.29° were used as reference peaks.

TGA and XPS for the oxygen vacancy concentration - The oxidation state of as synthesized reduced MoO_{3-x} was confirmed by Thermogravimetric analysis (TGA) and X-ray photoelectron spectroscopy (XPS). TGA was performed in either air or argon atmosphere using a TA SDT Q600 analyzer at a heating rate of 10 °C/min. XPS analysis was performed using a Kratos Axis Ultra DLD with a monochromatic Al (Kα) radiation source. The charge neutralizer filament was used to control charging of the sample, 20 eV pass energy was used with a 0.05 eV step size, and scans were calibrated using the C 1s peak shifted to 284.8 eV. The samples were etched with a Ar beam (raster size 5 mm x 5 mm) for 30 seconds. The integrated area of the peaks was found using the CasaXPS software, and atomic ratios were also found using this software. The atomic sensitivity factors used were from the Kratos library within the Casa software.

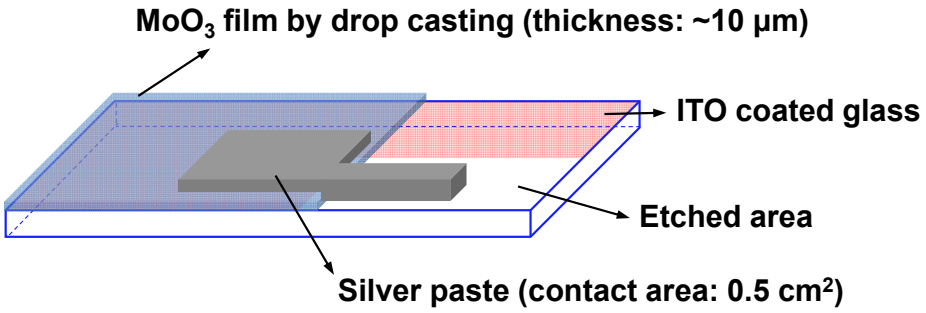

Figure 2.2. Schematic figure of setup for bulk electrical conductivity measurement of reduced MoO_{3-x}, partly reduced MoO_3, and fully oxidized MoO_3.

Electronic conductivity measurement - For the bulk electrical conductivity measurement, MoO_3 powder was deposited on the ITO coated glass (~ 10 μm thinkness) which had been partially etched. Contacts were made to the top and bottom of the sample, the latter coming from the ITO bottom contact. Electrical resistivity was measured by a Solartron 1287 potentiostat and electronic conductivity was calculated from the measured resistivity using the following equation.

$$\boldsymbol{k = \frac{t}{R \times A}} \qquad \text{eq. 2.1}$$

'*k*' is electrical conductivity of material, 't' is sample thickness, 'A' is contact area, 'R' is resistivity of sample.

Electrochemical analysis - Electrochemical measurements were carried out in a three-electrode cell using the MoO_3 thin films as the working electrode. To prepare the working electrode, the different MoO_3 nanobelts (= 40 μg) were suspended in ethanol and drop cast on O_2 plasma treated stainless steel current collector (1 cm^2 area). The weight of active material was measured by a microbalance. 1 molar $LiClO_4$ in propylene carbonate was used as electrolyte and lithium metal foils were used as reference and counter electrodes. Cyclic voltammetry was performed between 1.5 and 3.5 V vs. Li^+/Li using a PAR EG&G 273A Potentiostat. All electrochemical measurements were performed in an argon filled glovebox.

Ex situ XPS - For the *ex situ* XPS experiment, reduced MoO_{3-x} and fully oxidized MoO_3 working electrodes were lithiated and de-lithiated by using cyclic voltammetry. After 5 cycles at 10 mV/s to stabilize the working electrode, the sample was cycled at 5 mV/s to the specific potential. The cycled working electrodes were removed from the cell, washed with dimethyl carbonate (DMC) and dried overnight in the argon filled glove box. These electrodes were loaded on the XPS sample holder in the glove box and sealed in the XPS transfer chamber.

Ex situ XRD – *Ex situ* X-ray diffraction (XRD) was performed in a Bruker Discover D8 operating with Cu Kα (λ = 1.5418 Å) using a 0.035° step size, a voltage of 40kV, and a current of 40mA. For the sample preparation, reduced MoO_{3-x} and fully oxidized MoO_3 were galvanostatically discharged and charged at a C/5 rate. The cycled electrodes were washed in dimethyl carbonate and dried for 24 hours. The samples were sealed in 64 μm polyimide tape to prevent exposure to the environment. All preparation of the ex *situ* samples were performed in an Ar-filled glove box with O_2 below 1ppm.

Chapter 2.4. Results and discussion

Structural characterization

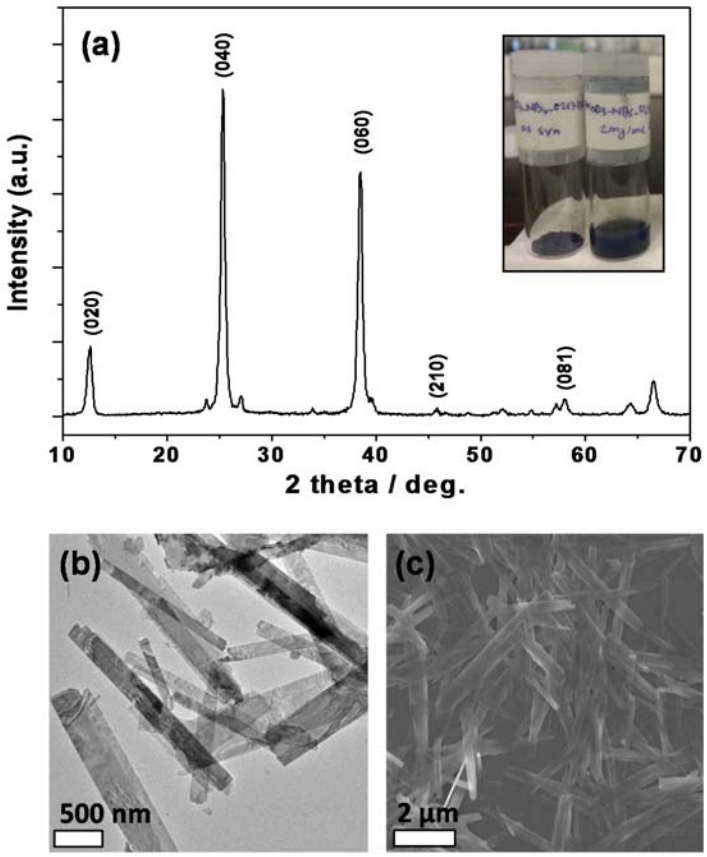

Figure 2.3. (a) XRD pattern and blue-colored powder (inset) of as synthesized reduced MoO_{3-x}, (b) TEM image, and (c) SEM image of reduced MoO_{3-x} nanobelts.

Reduced MoO_{3-x} was prepared by microwave activated hydrothermal synthesis. The use of microwaves has been shown to increase reaction kinetics as microwave radiation penetrates deep within the material and provides uniform heating[33]. This method has been applied to the synthesis of several Li-ion battery electrode materials including $LiFePO_4$ and $LiMnO_2$[34, 35, 36]. Although this specific synthetic route has not been reported previously for MoO_3, hydrothermal synthesis methods have been reported[23, 37]. However, the previously reported experiments required much longer reaction times (several hours to days) and did not lead to the formation of oxygen vacancies. In the current work, the synthesis of reduced MoO_{3-x} was completed in 15 min at 170 °C and also resulted in a non-stoichiometric MoO_3 material. The X-ray diffraction (XRD) pattern for the as-synthesized material is shown in Figure 2.3(a). The major reflections can be indexed with a *Pbnm* space group corresponding to α-MoO_3, in good agreement with JCPDS NO. 35-0609.

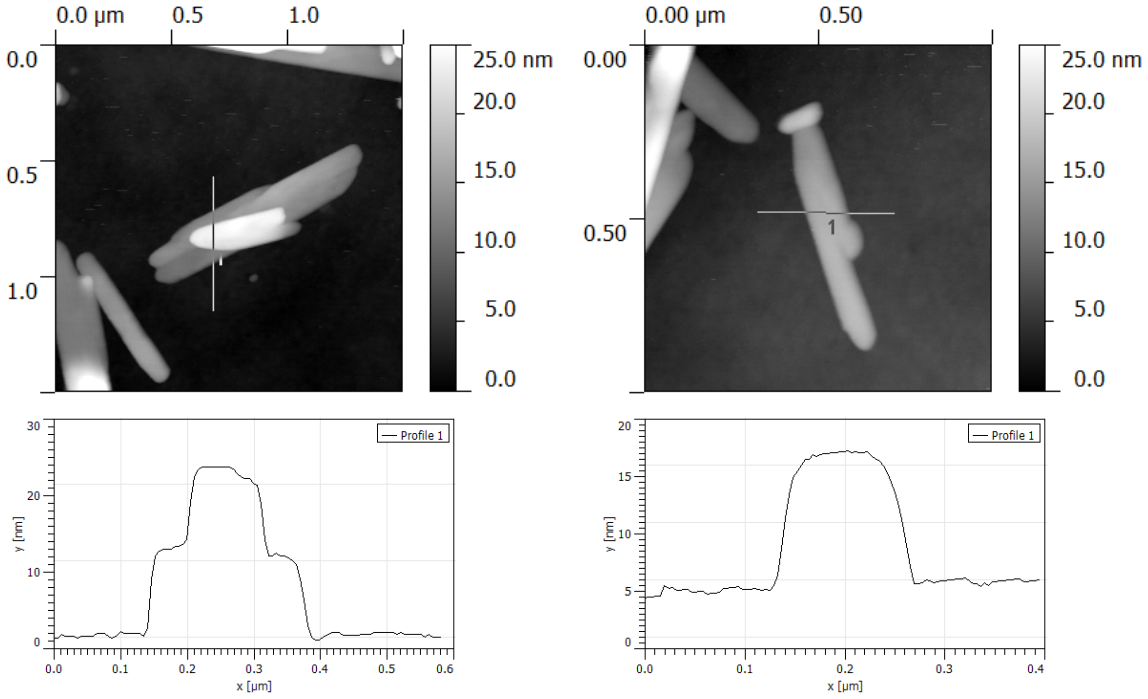

Figure 2.4. AFM analysis on the reduced MoO_{3-x}. Images (top) and height analysis on the selected parts (bottom) are presented.

The strong diffraction intensity for the (020), (040), and (060) peaks indicates that the as-synthesized α-MoO_3 powders preferentially orient along the [0b0] direction. Since MoO_3 is light blue, it is surprising that the color of as-synthesized α-MoO_3 was deep blue (inset in Figure 2.3(a)). This indicated that as-synthesized MoO_3 was reduced during the synthesis treatment. The shape and size of reduced MoO_{3-x} were confirmed by transmission electron microscopy (TEM) (Figure 2.3(b)) and scanning electron microscopy (SEM) (Figure 2.3(c)). The MoO_{3-x} materials are in the form of nanobelts which are 100 to 500 nm in width and 3 ~ 5 μm in length. The thickness of individual MoO_{3-x} nanobelts was determined by atomic force microscopy (AFM) to be about 10 nm (Figure 2.4.).

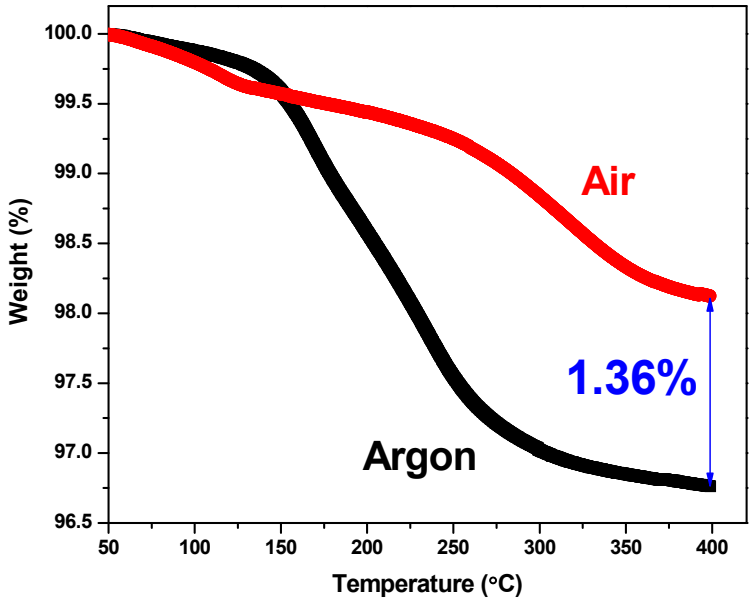

Figure 2.5. TGA analysis on reduced MoO_{3-x} in air and argon with a flow of 100 ml/min

The oxygen vacancy concentration of reduced MoO_{3-x} was characterized using thermogravimetric analysis (TGA) and X-ray photoelectron spectroscopy (XPS) (Figures 2.5. and 2.6.). The TGA experiment was carried out on reduced MoO_{3-x} by ramping up to 400 °C at 10 °C/min with 100 ml/min gas flow of either argon or air. TGA of reduced MoO_{3-x} (Figure 2.5.)

indicates that the reduced material reacts with oxygen upon heating leading to a lower mass loss compared to the TGA in Argon. The concentration of oxygen vacancies can be calculated from the difference in weight decrease between the two TGA experiments. From these calculations, we estimate that the composition of the reduced molybdenum oxide corresponds to $MoO_{2.87}$. To complement these calculations, XPS was used to characterize the oxidation state of molybdenum. The surface of reduced MoO_{3-x} has a significant amount of Mo^{5+} which is still observed even after a significant amount of Argon plasma etching (Figure 2.6.). The calculated stoichiometries based on the XPS spectra for molybdenum and oxygen atoms are $MoO_{2.91}$ and $MoO_{2.83}$ for surface and bulk (i.e., after etching), respectively. These values are comparable to that determined from TGA experiments. These results establish that the oxygen vacancies are not limited to the surface, and that they extend throughout the bulk of the material.

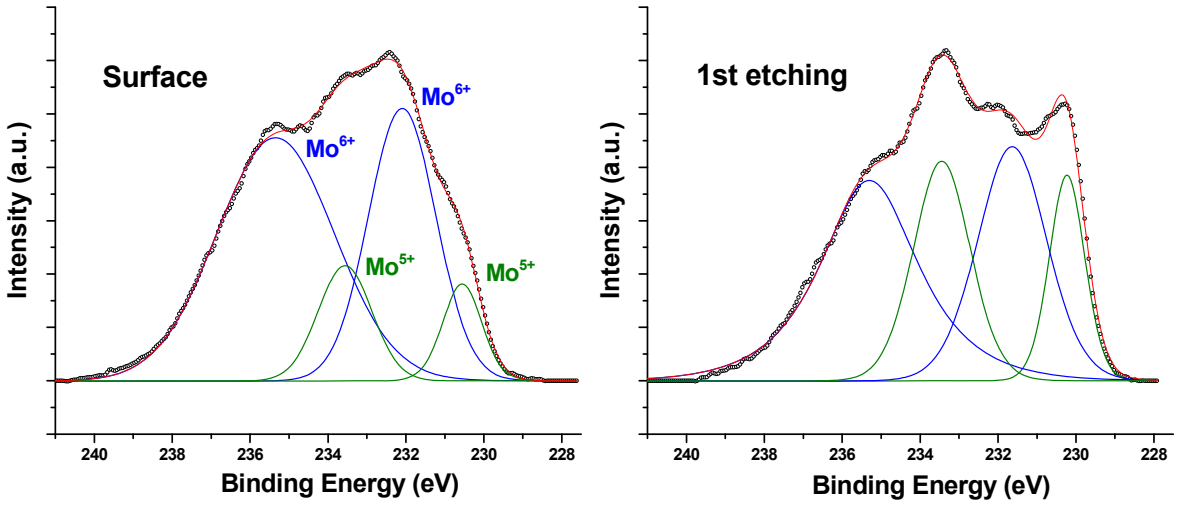

Figure 2.6. XPS data of the as-synthesized reduced MoO_{3-x} nanobelts before and after argon plasma etching. Argon plasma etching was used to differentiate the surface of reduced MoO_{3-x} nanobelts from the bulk.

In order to understand the influence of oxygen vacancies on electrochemical behavior, the reduced MoO_{3-x} was subjected to different heat treatments to partially or fully oxidize the MoO_3. Heating in air at 150 °C for 2 hr produced partly reduced MoO_3 (light blue color), while heating at 400 °C for 1 hr produced the fully oxidized MoO_3 (white color). After heat treatment, the phase of each material was confirmed by XRD to have the α-MoO_3 structure (Figure 2.7(a)). The morphologies of the three samples were characterized by TEM before and after heat treatment (Figure 2.7(b-d)). No significant change from the nanobelt morphology was evident. Brunauer-Emmett-Teller (BET) surface areas of these samples were determined to be 24, 25, and 15 m^2/g for the reduced, partly reduced, and fully oxidized MoO_3, respectively. The relatively small difference in surface areas is not likely to affect the electrochemistry of MoO_3.

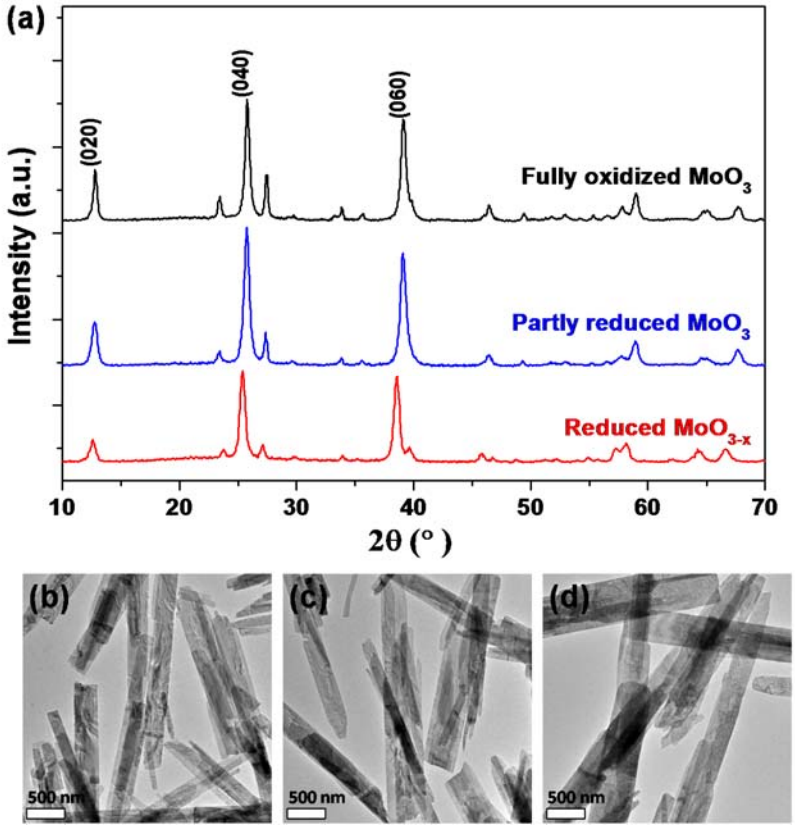

Figure 2.7. (a) XRD patterns of reduced MoO_3-x, partly reduced MoO_3, and fully oxidized MoO_3 and TEM images of (b) reduced MoO_{3-x}, (c) partly reduced MoO_3, and (d) fully oxidized MoO_3.

Electrochemical behavior

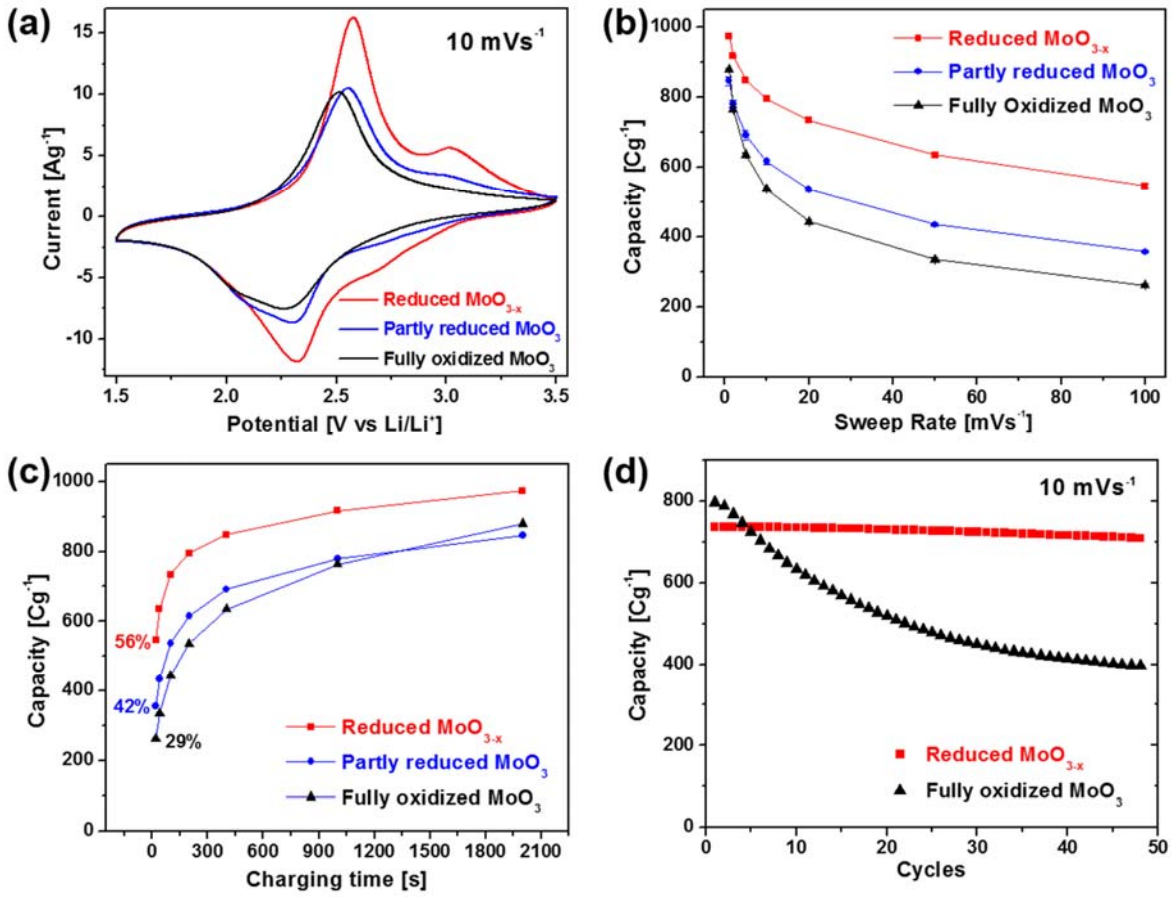

Figure 2.8. Electrochemistry of reduced MoO_{3-x}, partly reduced, and fully oxidized MoO_3: (a) Cyclic voltammetry (at 10 mVs^{-1} in 1M $LiClO_4$ in PC), (b) specific capacity depending on the sweep rate, (c) specific capacity versus charging time, and (d) cyclability test between fully oxidized MoO_3 and reduced MoO_{3-x}

Cyclic voltammetry (CV) was used to compare the electrochemical properties of reduced MoO_{3-x} and fully oxidized MoO_3. There are two distinguishable lithium intercalation sites as shown in Figure 2.1 for the α-MoO_3 system. The 'interlayer site' is located between two octahedral bilayers while the 'intralayer site', is in the one dimensional tunnel ([001] direction) within the bilayer sheets. Charge storage for MoO_3 occurs mainly by the insertion of lithium ions

into the interlayer site to form lithiated MoO_3 (Li_xMoO_3, $x_{max} = 1.5$)[21] leading to a maximum capacity of 1080 C/g.

$$MoO_3 + xLi^+ + xe^- \rightarrow Li_xMoO_3 \qquad \text{eq. 2.2}$$

Sweep voltammetry measurements were used to characterize the electrochemical properties. As described in the Experimental section, these experiments used flooded three-electrode cells in which the working electrode was a thin film (40 μg/cm^2) of either reduced MoO_{3-x}, partly reduced MoO_{3-x} or fully oxidized MoO_3 with lithium metal reference and counter electrodes. These electrodes contained no carbon or binder so that the electrochemical properties of the different oxides were determined directly. This is a good way to investigate the fundamental properties of material because the data we collected is only from our active materials. The results show that reduced MoO_{3-x} has a higher capacity and faster kinetics compared to the other MoO_3 nanobelt materials. At a sweep rate of 100 mV/s, which corresponds to a charging time of 20 seconds, reduced MoO_{3-x} stores ~ 550 C/g while the capacity for the other materials is < 400 C/g at this sweep rate (Figure 2.8 (b, c)). This fast response underscores the capacitive nature of charge storage in reduced MoO_{3-x}. In addition, the cycling behavior of reduced MoO_{3-x} is more stable than that of fully oxidized MoO_3 (Figure 2.8 (d)). After 50 cycles at 10 mV/s, the capacity has decreased around 5% in contrast to the 50% decay exhibited by the oxidized MoO_3. The initial capacity drop in fully oxidized MoO_3 is well known electrochemical behavior of MoO_3 with lithium. This cyclability test shows that by introducing oxygen vacancies it is possible to improve the cycling stability of α-MoO_3, a feature which has been a significant limitation in the application of this material in electrochemical devices.

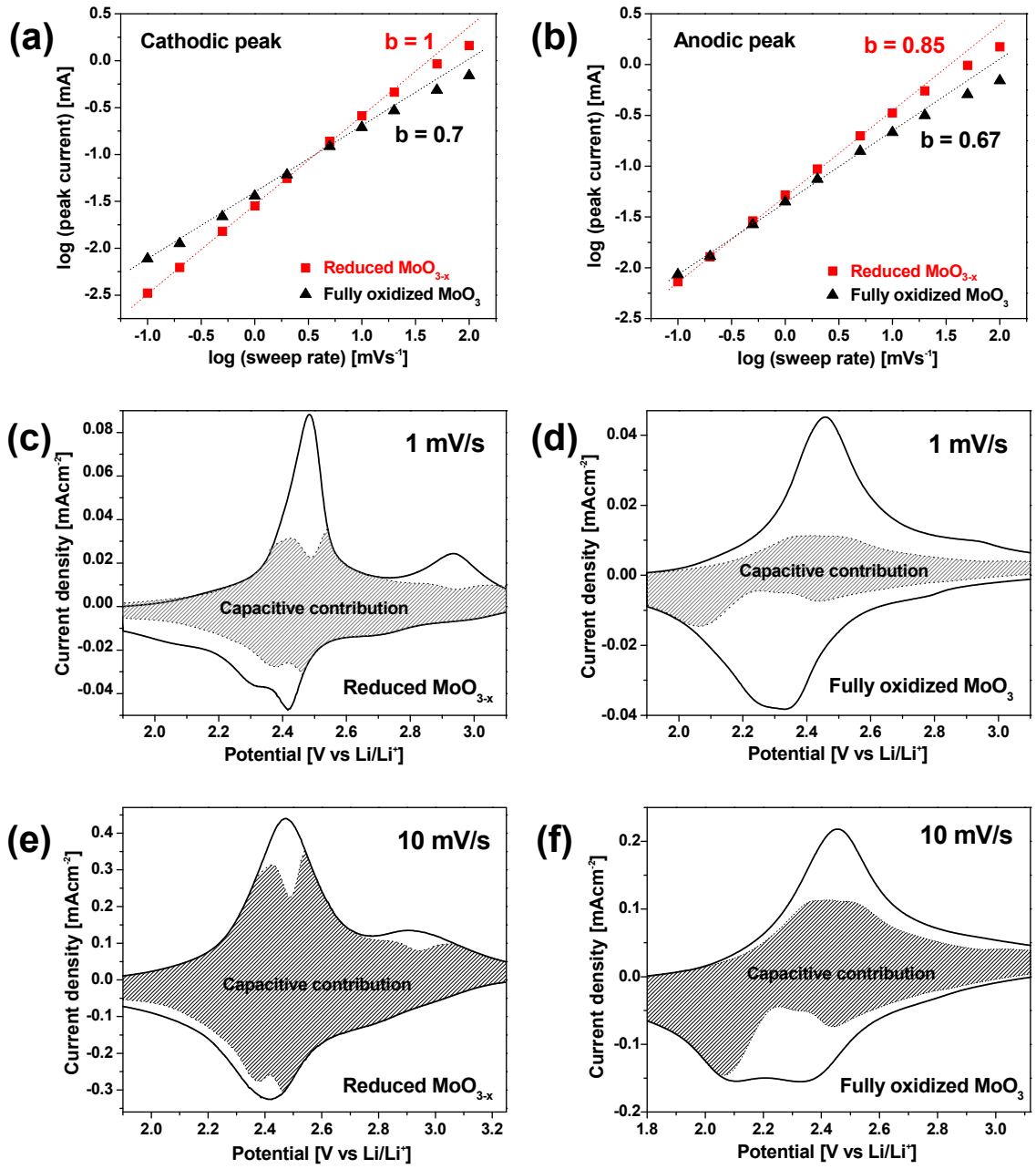

Figure 2.9. Kinetic analysis of reduced MoO_{3-x} and fully oxidized MoO_3 using power law relationship: b-values from (a) cathodic peaks and (b) anodic peaks. Capacitive charge storage contribution in (c, d) reduced MoO_{3-x} at 1 mV/s (75 %) and 10 mV/s (88 %) and (c) fully oxidized MoO_3 at 1 mV/s (37 %) and 10 mV/s (67 %)

Sweep voltammetry also provides greater insight regarding the difference in charge storage kinetics. In Figure 2.9 (a, b), the log (i) vs. log (ν) plot for the cathodic and anodic peaks at ~ 2.5 V (vs. Li/Li^+) shows that the current dependence on sweep rate, ν, is given by the relation:[38]

$$i = a\, v^b \qquad \text{eq. 2.3}$$

A *b*-value of 0.5 indicates that the current is controlled by semi-infinite diffusion while $b = 1$ indicates that the current is surface controlled[39]. For reduced MoO_{3-x}, the *b*-value is ~ 1 for cathodic peak and ~ 0.85 for anodic peak in the sweep rate range from 0.1 to 20 mV/s, indicating the capacitor-like nature of the kinetics. Prior research has shown that this behavior is one of the characteristic features of pseudocapacitance[40]. In contrast, fully oxidized MoO_3 exhibits values ~ 0.7 for cathodic and ~ 0.67 for anodic peak over this same range of sweep rates, indicating that charge storage is affected by diffusion processes. The increased level of pseudocapacitive charge storage for reduced MoO_{3-x} is also shown using an analysis where the current response to a fixed potential, *i*(V), is a combination of capacitor-like and diffusion-controlled behaviors[41]:

$$i(V) = k_1\, v + k_2\, v^{1/2} \qquad \text{eq. 2.4}$$

By determining both k_1 and k_2 values, it is possible to calculate, as a function of potential, the fraction of current contributed by diffusion-controlled intercalation processes and that arising from capacitor-like processes. The data shown in Figure 2.9 (c-f) indicate that capacitor-like charge storage in reduced MoO_{3-x} occurs to a much greater extent (75 % vs 37 % at 1 mV/s and

88 % vs. 76 % at 10 mV/s) than charge storage in fully oxidized MoO_3. It is interesting to note that in prior work with mesoporous films of MoO_3, a comparable fraction of capacitive storage, ~70 %, was obtained[6]. In that case, however, the morphology of the mesoporous architecture, 10 nm thick walls of MoO_3, leads to a greater level of capacitor-like response. In summary, the sweep voltammetry measurements show that reduced MoO_{3-x} exhibits higher capacity and faster kinetics than either partly reduced MoO_{3-x} or fully oxidized MoO_3.

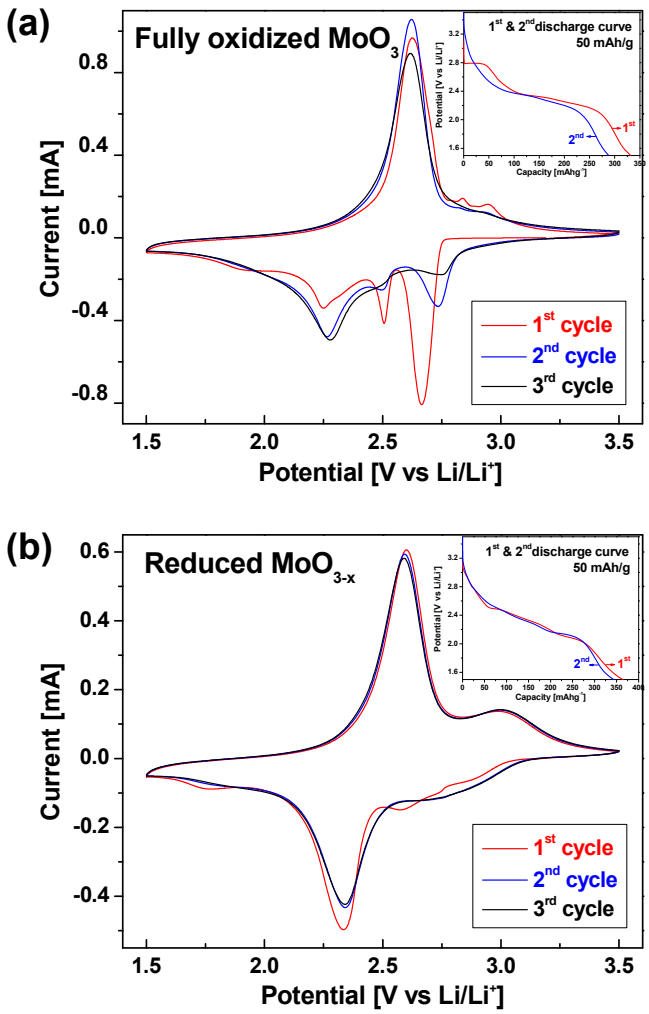

Figure 2.10. Comparison of first three cycles of cyclic voltammetry at 10 mV/s, and galvanostatic discharge curve (insets) in (a) reduced MoO_{3-x}, and (b) fully oxidized MoO_3

The voltammetric sweeps for the reduced MoO_{3-x} display two interesting differences compared to those of the fully oxidized MoO_3. It is well known that MoO_3 exhibits an irreversible peak on lithiation during its first cycle as shown in Figure 2.10 (a). This irreversibility is attributed to trapping of Li^+ in intralayer spaces of α-MoO_3 and leads to poor electrochemical reversibility[22, 24, 42]. However, the cyclic voltammetry of reduced MoO_{3-x} does not display these irreversible peaks as the first, second, and third cycles were almost identical (Figure 2.10 (b)). The galvanostatic discharge curves are consistent with this behavior (see insets for Figures 2.10 (a,b)). The fully oxidized MoO_3 exhibits a plateau during its first cycle which disappears during the second cycle while reduced MoO_{3-x} displays no such plateau, indicating that no structural change is occurring on cycling. Thus, reduced MoO_{3-x} retains its capacity on cycling while the capacity decreases continuously for fully oxidized MoO_3 because of the structural rearrangement and the likely trapping of Li^+ (Figure 2.8).

A second feature in the voltammetry which is influenced by the presence of oxygen vacancies is the addition of a distinctive peak at ~3.0 V during de-intercalation (Figure 2.8 (a) and Figure 2.10 (b)). This peak does not occur in the fully oxidized MoO_3. In order to explain the existence of this additional peak, the intercalation energies for the interlayer and intralayer sites were calculated by DFT for both reduced MoO_{3-x} and fully oxidized MoO_3. In fully oxidized MoO_3, the values for the interlayer and intralayer sites (see Figure 2.1 (b, c)) were 3.25 and 3.21 eV, respectively. That is, the energy difference between the two types of sites is negligible. The similarity in intercalation energy for these sites leads to one main peak in the CV for fully oxidized MoO_3.

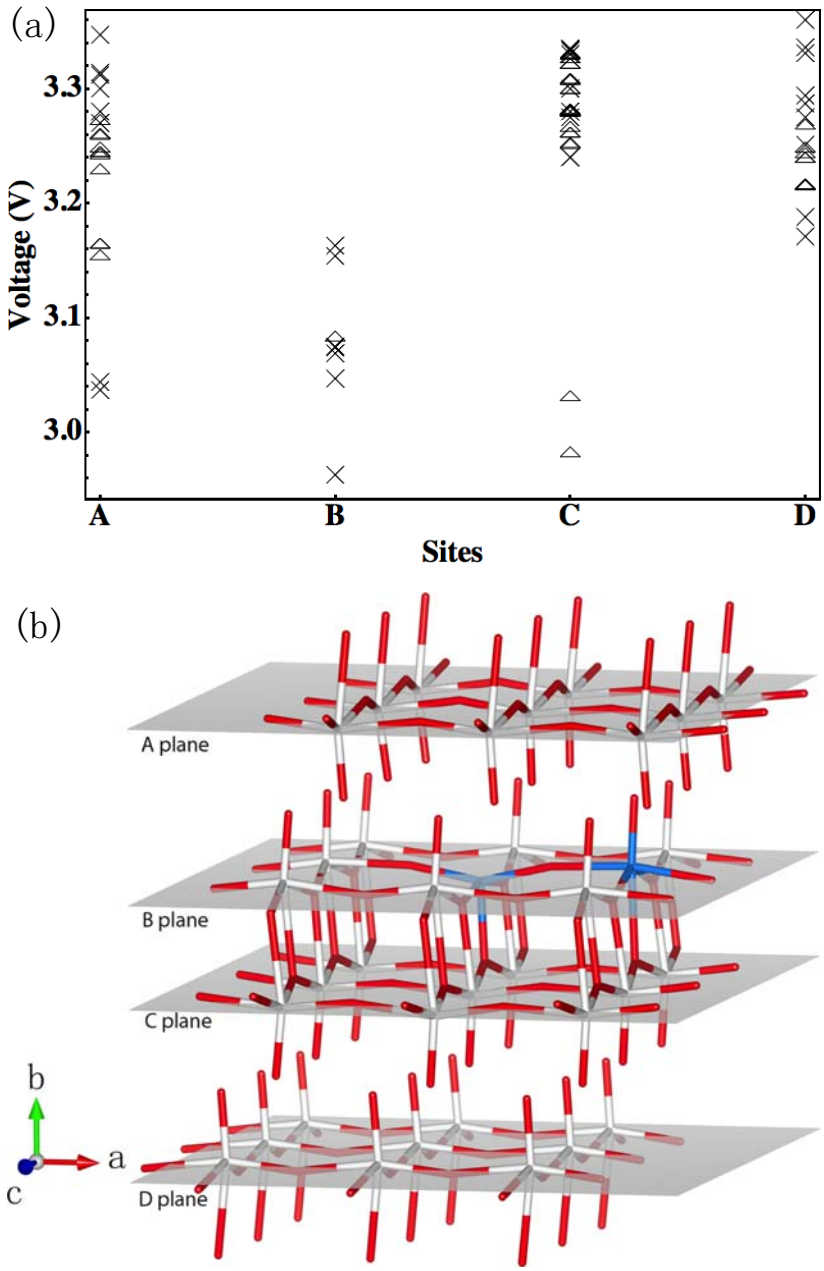

Figure 2.11. (a) Calculated lithium intercalation voltages at interlayer sites (cross) and intralyer sites (triangle) of reduced MoO_{3-x}. A, B, C, D sites indicate the positions of an additional polaron introduced by lithium intercalation. For example, the A site means that the additional polaron is located at the A plane which provides intralayers sites as shown in (b). (Figures from Hao Lin)

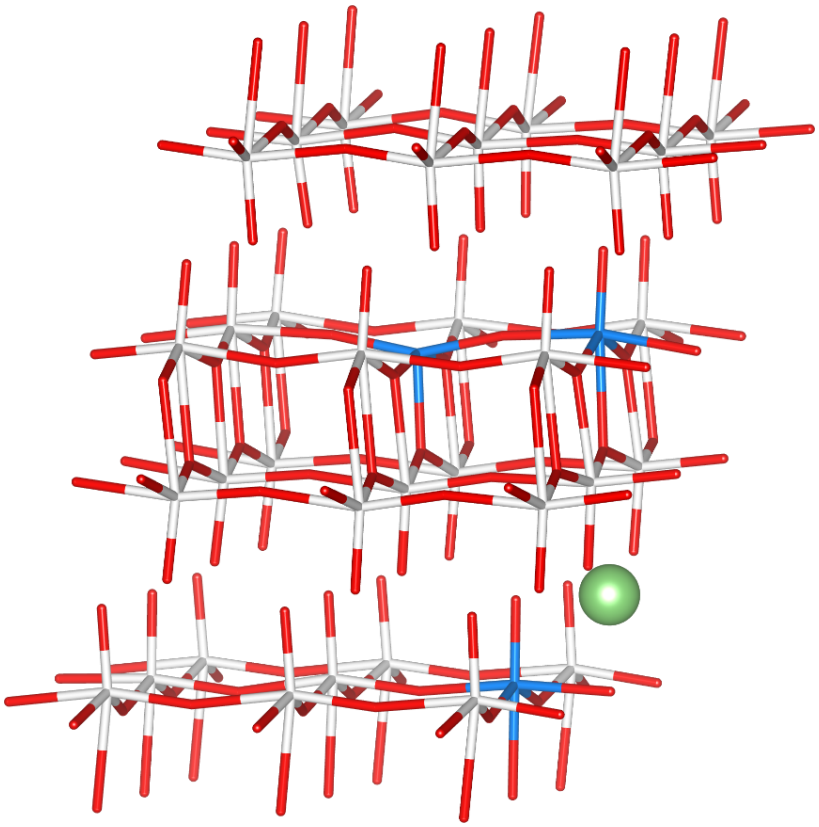

Figure 2.12. The lithium intercalation sites for the highest lithium intercalation voltage (Figure from Hao Lin)

The introduction of oxygen vacancies and polarons in reduced MoO_{3-x} breaks the symmetry of the crystal. Hence all the interlayer and intralayer sites for lithium insertion no longer have the same energy. We calculated the intercalation energies of all the possible lithium insertion sites together with random initialization of polaron states. The voltages calculated for the reduced MoO_{3-x} are in the range 2.96 to 3.36 V as shown in Figure 2.11 (a). Except for the d_{yz} polaron at the oxygen defect center, all the polarons stabilize at the d_{xz} orbitals in the Mo ions. The distance between lithium intercalation sites and the oxygen vacancy center along with the different polaron configurations contribute to the spread of the intercalation voltages. There are

several factors which contribute to the variation in lithium intercalation voltage: 1) the nature of the lithium intercalation sites; 2) binding between lithium ions and polarons; 3) binding between two polarons; 4) interaction among oxygen vacancies, lithium ions and polarons. The factor which dominates the intercalation voltage is unknown and quantitative understanding of these effects can be realized by the cluster expansion method, which is beyond the scope of this study. Nevertheless, we expect that after structural relaxation, it is more likely that one observes the intercalated structures with higher voltages (>3.30 V) because these structures are thermodynamically more stable. As shown in Figure 2.11 (b), our results indicate that the additional polaron introduced by lithium intercalation does not favor the B plane, where the oxygen defect induced polarons are located. In other words polarons are unlikely to remain together as the polaron concentration increases from 0.22 to 0.33 within the same plane. The highest intercalation energy corresponds to the structure in which the lithium ion at the interlayer site is far from the oxygen vacancy center (6.3 Å) and the additional polaron introduced along with the lithium ion is not in the same layer as those polarons introduced by an oxygen vacancy (see Figure 2.12). The new peak at 3.0 V in the CV of reduced MoO_{3-x}, reflects the increase of voltage in the calculations. Compared to lithium intercalation in the fully oxidized MoO_3, oxygen vacancies in the reduced MoO_{3-x} might assist the structural relaxation which occurs during the lithium intercalation, leading to higher voltages. Therefore, a new peak is only observed in the reduced MoO_{3-x}. In the discharge process, this peak is less distinctive because lithium ions might not migrate directly from the electrolyte to the high voltage sites in reduced MoO_{3-x}. Instead only the diffusion of lithium from the electrolyte to the most stable sites existing near the interface between electrode and electrolyte can contribute to the weak signal of the new peak.

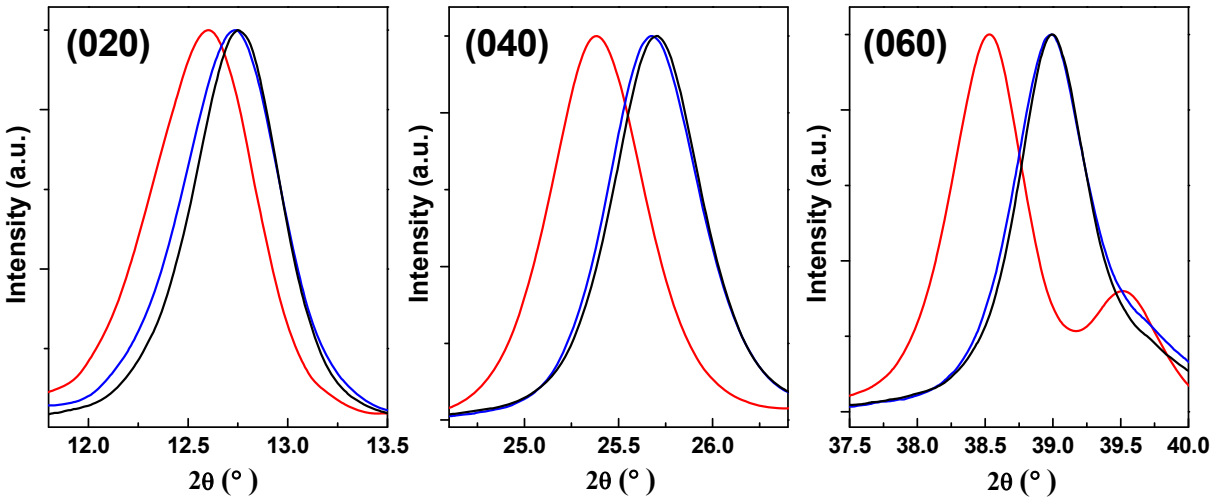

Figure 2.13. Comparison of (020), (040), and (060) diffraction peaks in reduced MoO_{3-x} (red), partly reduced MoO_3 (blue), and fully oxidized MoO_3 (black). (Peak positions were calibrated using an internal silicon standard at 28.4°)

Structure and chemical effects

The creation of oxygen vacancies in α-MoO_3 leads to a material which exhibits higher capacity, faster kinetics and better electrochemical stability compared to the fully oxidized material. In this section, we discuss the structural and chemical features which influence and determine these properties. One significant structural effect associated with the development of oxygen vacancies is an increase in the van der Waals gap, a feature which will certainly lead to improved electrochemical kinetics. The X-ray diffraction data (Figure 2.13) shows that the (020), (040), and (060) reflections, which correspond to the *b*-lattice plane interlayers, are shifted to lower angles in the reduced MoO_{3-x} sample.

Sample	(020) d (Å)	(040) d (Å)	(060) d (Å)
Reduced MoO_{3-x}	**7.031**	**3.505**	**2.335**
Partly reduced MoO_3	**6.954**	**3.465**	**2.308**
Fully Oxidized MoO_3	**6.943**	**3.462**	**2.307**

Table 2.1. Calculated d-spacing values for the (020), (040), and (060) reflections

	a(Å)	b(Å)	c(Å)
Pure-MoO_3	**11.686**	**13.904**	**11.357**
Reduced-$MoO_{2.972}$	**11.650**	**13.930**	**11.393**

Table 2.2. Calculated lattice parameters by DFT calculation when one oxygen vacancy is introduced

The *b*-lattice cell parameter, calculated from the (020) reflections, expands from 13.886 Å for the fully oxidized MoO_3 to 14.062 Å in the reduced MoO_{3-x} material (Table 2.1). The development of a wider van der Waals gap arising from oxygen vacancies was previously reported[29] and seems to occur here as well. DFT calculations (Table 2.2) indicate that the van der Waals gap will expand in reduced MoO_{3-x} due to an oxygen vacancy at the O_t site with two accompanying Mo^{5+} ions.

A second structural consideration is the difference in phase behavior between reduced MoO_{3-x} and fully oxidized MoO_3. The irreversible electrochemical changes shown in Figure 2.13 (a)

were also observed using *ex situ* XRD (Figure 2.14 (a)). Upon lithiation, the α-MoO_3 becomes nearly featureless. The (040) and (060) reflections were absent and the (020) was shifted and broadened, which is consistent with previous reports[24, 42]. Peak broadening is an indication that the long range atomic order is destroyed or that the domain size is extremely small. In addition, at 1.5 V, the (020) reflection is shifted to a lower angle indicating that a lattice expansion occurred after the structural change at 2.7 V. After de-lithiation (3.5V), the (020) peak does not return to the original position of 12.74 (2θ), consistent with there being a phase change. Moreover, the (040) and (060) peaks were still missing. The absence of the higher order peaks of (020) after cycling can be attributed to irreversible lithium insertion into the intralayers of fully oxidized MoO_3, which causes a structural rearrangement that diminishes long range order[22].

In contrast, reduced MoO_{3-x} does not undergo a phase transformation upon lithiation to 1.5V (Figure 2.14 (b)). The (040) diffraction peak for reduced MoO_{3-x}, is at nearly the same position as the pristine material, while the XRD pattern for the lithiated state of fully oxidized MoO_3 is characterized by the development of broad featureless peaks. After full de-lithiation, the diffraction peaks return to approximately the same positions of the pristine material indicating that the lithiation/delithiation processes are reversible and that there is little if any structural deterioration from Li^+ insertion/de-insertion. Quantitatively, the *b*-lattice parameter, as calculated from the (020) reflection after 10 cycles, returns to 14.08Å which is in reasonable agreement with the *b*-lattice parameter of 14.06Å determined for the initial material. The difference in phase stability explains why reduced MoO_{3-x}, exhibits stable cycling performance compared to fully oxidized MoO_3. Finally, it is important to note that there is no indication of diffraction peaks related to monoclinic MoO_2 in the XRD patterns for reduced MoO_{3-x} even though *ex situ* XPS shows a significant amount of Mo^{4+} at 1.5 V as discussed in the following paragraph.

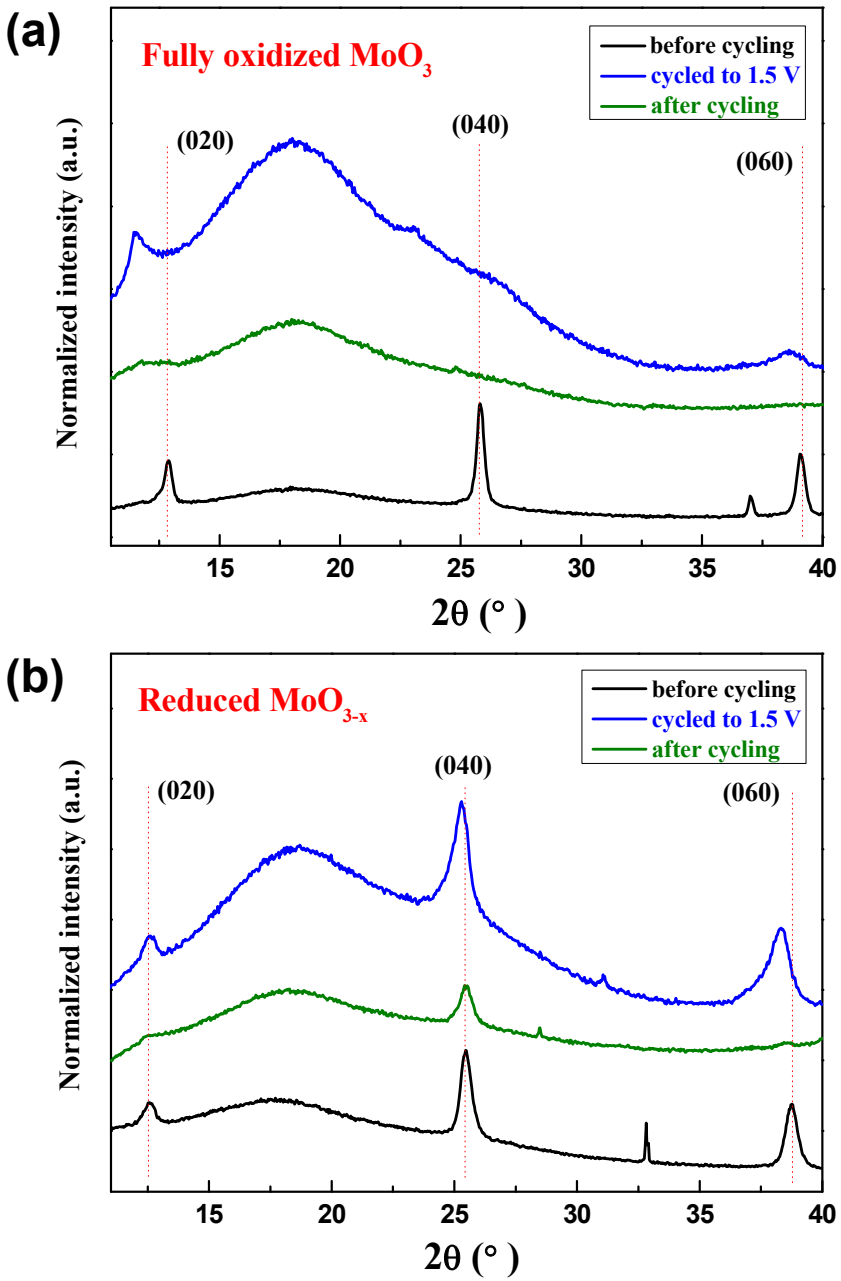

Figure 2.14. *Ex situ* XRD at various charge states for (a) reduced MoO_{3-x}, and (b) fully oxidized MoO_3.

An intriguing feature with the electrochemical properties of reduced MoO_{3-x} is that the material clearly exhibits a higher capacity than fully oxidized MoO_3 despite the fact that the

MoO_{3-x} has a lower average oxidation state. That is, the improved rate capability and electrochemical stability of reduced MoO_{3-x} can be explained by structural modifications which result from the formation of oxygen vacancies, however, it is not clear whether oxygen vacancies would also lead to the higher capacity observed with this material (Figure 2.8 (b)). To address this issue, *ex situ* XPS was performed on both fully oxidized MoO_3 and reduced MoO_{3-x} at the same potentials (Figure 2.15): after full lithiation at 1.5 V (vs. Li/Li^+) and after delithiation at 3.5 V.

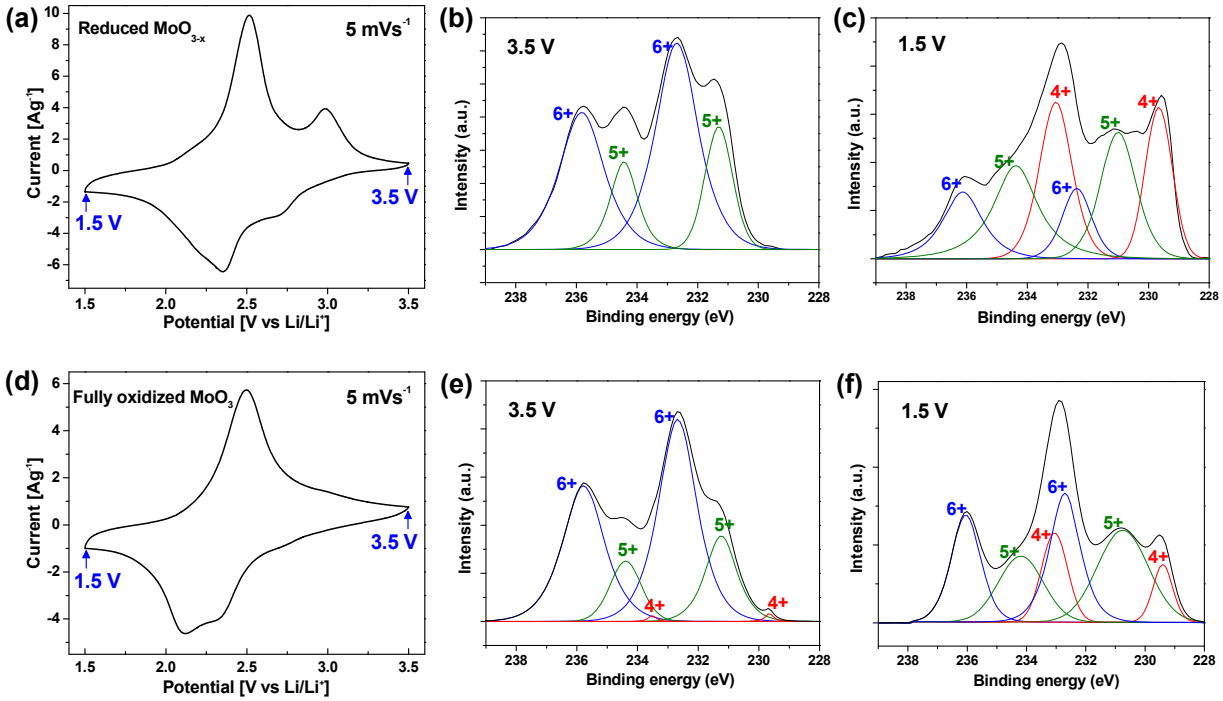

Figure 2.15. *Ex situ* XPS of reduced MoO_{3-x}, and fully oxidized MoO_3: Cyclic voltammetry of (a) reduced MoO_{3-x}, and (b) fully oxidized MoO_3 at 5 mVs^{-1}. XPS at (b) 3.5 V, and (c) 1.5 V in reduced MoO_{3-x}. XPS at (e) 3.5 V and (f) 1.5 V in fully oxidized MoO_3

The most interesting feature in the XPS spectra is the presence of Mo^{4+} upon lithiation for both the reduced MoO_{3-x} and the fully oxidized MoO_3. For the reduced MoO_{3-x}, the fraction of Mo^{4+}

is ~ 40 % (Figure 2.15 (c)). Despite this significant amount, the α-MoO_3 structure was retained and XRD showed no evidence of MoO_2 (Figure 2.14 (b)). By comparison, the fully oxidized MoO_3 exhibited only ~ 20 % (Figure 2.15 (f)). Another interesting characteristic is the ratio of Mo^{4+}/ Mo^{6+} in each of the materials. For the reduced MoO_{3-x}, this ratio is ~ 2 whereas for the fully oxidized MoO_3, the ratio is ~ 0.8. These results indicate that the difference in capacity between reduced MoO_{3-x} and fully oxidized MoO_3 arises from the greater amount of conversion to Mo^{4+} upon lithiation. In this regard, the existence of polarons in the MoO_{3-x} is likely to be beneficial in achieving the higher degree of Mo^{4+}.

The *ex situ* XPS spectra also provide insight concerning the electrochemical reversibility of the two materials. When de-lithiated at 3.5V, the reduced MoO_{3-x} shows that only Mo^{6+} and Mo^{5+} are present whereas fully oxidized MoO_3 indicates the presence of these ions along with a small amount of Mo^{4+} (Figure 2.18 (b) and 2.18 (e)). The latter is an indication that some Li^+ remains trapped in the MoO_3 structure, which is likely to be associated with the phase change that occurs on the first lithiation (Figure 2.17 (a)).

Chapter 2.5. Conclusion

In this work we have demonstrated a simple method for introducing oxygen vacancies into the MoO_3 lattice that lead to improved electrochemical properties. The introduction of oxygen vacancies leads to a larger interlayer spacing along the *b*-axis that promotes faster kinetics and enables the α-MoO_3 structure to be retained during the insertion and removal of Li-ions. The preservation of the as-synthesized MoO_{3-x} structure seems to be related to the good cycle life of reduced MoO_{3-x}. The higher specific capacity in reduced MoO_{3-x} was explained through *ex situ* XPS and XRD. These techniques showed that a significant amount of Mo^{4+} was formed upon lithiation, reversibly and without the development of the monoclinic MoO_2 phase.

This work demonstrates that the energy storage properties of MoO_3 are improved substantially from the introduction of oxygen vacancies. In the future, we believe that the incorporation of oxygen vacancies into other transition metal oxides will lead to a wide range of materials whose properties are extremely attractive for pseudocapacitive charge storage.

Chapter 3. Development of pseudocapacitive properties in MoO_2 nanoparticles

Chapter 3.1. Introduction

Capacitive energy storage is distinguished from other electrochemical energy storage approaches by short charging times and the delivery of significantly more power than batteries[1]. A key limitation to this technology is its low energy density and, for this reason, there is growing interest in pseudocapacitive materials that store charge through faradaic reactions at or near the surface[11, 43] thus leading to energy densities which approach those of batteries (~100 Wh kg^{-1})[7]. In recent papers, we have suggested that pseudocapacitive materials can be classified as extrinsic or intrinsic[13, 14]. Examples of intrinsic pseudocapacitive materials are $RuO_2 \cdot nH_2O$[9], MnO_2[10], and T-Nb_2O_5[10, 44]. The electrochemical properties of extrinsic pseudocapacitor materials are dependent on particle size, with fundamental changes in redox reactions occurring in finite sized systems. Phase transformations and solid-state ion diffusion in these materials limit fast kinetics. However, pseudocapacitance can be achieved by developing nanostructures with short ion diffusion path lengths, since the diffusion time is proportional to the square of diffusion length and inversely proportional to diffusivity[45].

In addition, phase transformations associated with battery-type energy storage may be inhibited in nanostructured materials. We hypothesize that the suppression of phase transformations is required in the cross-over from battery-like charge storage to extrinsic pseudocapacitive charge storage because nucleation and growth of new phases are kinetically slow[13]. For example, $LiCoO_2$ shows extrinsic pseudocapacitive properties, e.g. a sloping galvanostatic voltage profile, when the material is nanostructured. However, as a micron-sized material, the sloped voltage profile changes to a flat discharge curve, indicative of a bulk material undergoing a phase transformation[46].

Chapter 3.2. Technical background

Chapter 3.2.1. Molybdenum dioxide (MoO_2)

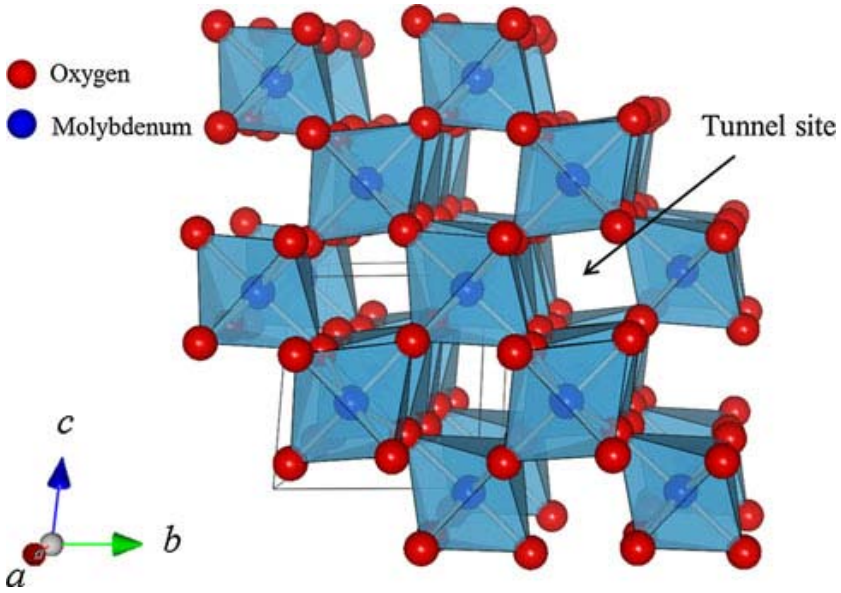

Figure 3.1. The structure of monoclinic MoO_2

Molybdenum dioxide (MoO_2) is a promising negative electrode material for lithium ion batteries because of its low metallic resistivity (8.8×10^{-5} Ω cm at 300 K), capacity up to 840 mAh/g (if four-electron redox reactions are considered), and high density (6.5 g/cm^3)[47, 48, 49]. The pseudocapacitance in MoO_2 was mentioned in a previous report[50]; however, this material has only been investigated for high energy density battery applications because of poor kinetic behavior. MoO_2 belongs to the space group of $P2_1/c$, which is constructed from a tunnel structure framework (Figure 3.1). The framework possesses a rutile-type structure which consists of MoO_6 octahedra linkages that form one dimensional channels along the a-axis where Li-ions can be inserted/extracted reversibly[51, 52]. Li^+ ion-based charge storage in MoO_2 occurs by two different mechanisms: (i) Li^+ ion insertion/deinsertion into the tunnel sites between 1.0 to 3.0 V (vs.

Li/Li^+)[52], and (ii) a conversion reaction below 1 V (vs. Li/Li^+)[53]. The electrochemical conversion reaction[54] in MoO_2 leads to a much higher theoretical capacity of 630 mAh/g compared to 210 mAh/g for the one-electron insertion/deinsertion process.

In most previous studies on MoO_2 both the intercalation process and the conversion reaction were utilized to achieve high capacity[47, 48, 49]. The conversion reaction, however, is generally slow and the reversibility is poor due to a large volume expansion during the conversion. Thus, the one-electron lithium intercalation reaction is a more promising charge storage mechanism for pseudocapacitive energy storage. Unfortunately, the one-electron intercalation process suffers from poor rate capability because the material undergoes a phase transformation between the monoclinic and orthorhombic phases during charging and discharging. The phase transition decreases the metallic conductivity by disrupting the pairing of molybdenum along the Mo atom chains in the monoclinic phase, resulting in reduced conductivity for Li_xMoO_2[52]. Potentially, however, the rate capability could be improved by nanostructuring MoO_2, as was shown in the case of $LiCoO_2$[55].

The synthesis of MoO_2 has generally has been achieved by reduction of MoO_3 under reducing conditions (using H_2 gas) at high temperature (> 600 °C) leading to large particle sizes[56, 57, 58]. Nanostructured MoO_2 has also been previously synthesized by reducing phosphomolybdic acid (Mo^{6+}) to MoO_2 (Mo^{4+}) in hydrogen while controlling the particle size in hard templates such as SBA 15[49]. This method requires multiple steps: synthesis of the hard template followed by synthesis of the nanostructured MoO_2 and template removal[48, 49]. Hydrothermal synthesis has several advantages compared to these high temperature reduction methods. The key advantage is that crystalline nanoparticles can be synthesized at relatively low temperature (180 °C) within a day[59].

Chapter 3.2.2. Intrinsic vs. Extrinsic pseudocapacitance

Pseudocapacitive properties can be intrinsic or extrinsic to a material[13]. Intrinsic pseudocapacitance has been demonstrated in $RuO_2 \cdot nH_2O$[9], MnO_2[10], and T-Nb_2O_5[10, 44] as these materials showed pseudocapacitive behavior regardless of their size and shape. However, with an extrinsic pseudocapacitor, reduction of size can lead to pseudocapacitive charge storage in some materials[46, 60]. Charge storage in the microsize of these materials such as $LiCoO_2$ and $LiFePO_4$ is limited by solid-state diffusion due to the phase transformation and long diffusion pathway for both ions and electrons. This ions intercalation induced phase transformation can be suppressed and also ions and electrons can have shorter diffusion length through reducing their size when they are connected to the electrical conductive matrix (e.g. carbon additives). A good example of an extrinsic pseudocapacitor is $LiCoO_2$ which is a well-known cathode material in bulk form[61]. $LiCoO_2$ has a flat voltage profile at 3.9 V which is indicative of a two-phase material arising from lithium intercalation. Okubo et al. investigated the effect that nanosizing has on the lithium ion intercalation behavior of this material. These authors revealed that when they decreased the size below 17 nm, the flat voltage profile was replaced with a sloped voltage profile, which is one of the electrochemical signatures of pseudocapacitance[46]. They also achieved high rate capability, for example, 100 mAh/g at 30 C rate (discharge in 2 min) and 75 mAh/g at 100 C rate (discharge in 36 S) using the 17 nm crystallite size $LiCoO_2$ nanoparticles. The research goal in the current study is the development of pseudocapacitive properties in MoO_2 by decreasing its particle size.

Chapter 3.2.3. Nanostructured materials for pseudocapacitive energy storage

As mentioned above, an effective method to develop pseudocapacitance is to reduce crystallite size. Nanomaterials for energy storage applications have the following advantages: i)

Short path lengths for ions and electrons enabling materials with low electronic or ionic conductivity, ii) Better accommodation of the strain during ion insertion/de-insertion leading to improved cycle life, iii) Higher electrode/electrolyte contact area resulting in higher charge/discharge rates. An additional benefit of nano-structuring is that phase transformations can potentially be suppressed. Charge storage not only exhibits better reversibility but also more rapid kinetics when not limited by a phase transformation. Thus, by decreasing the size of MoO_2, we expect to have better electrochemical performance such as high rate capability, suppression of phase transition, and better cyclability

Chapter 3.3. Experimental

Chapter 3.3.1 Nanosized-MoO_2, microsized-MoO_2, and MoO_2-RGO hybrid synthesis

MoO_2 and MoO_2-RGO synthesis - All starting materials were obtained from commercial suppliers and used without further purification. Nanosized-MoO_2 and MoO_2-RGO hybrids were synthesized by hydrothermal synthesis. The nanosized-MoO_2 was prepared in a 45 ml Teflon liner by dissolving 270 mg anhydrous $MoCl_5$ (Strem Chemicals) in a mixture of 5 ml ethanol and 15 ml deionized water. The hydrothermal reaction occurred at 180°C for 6 hrs. The MoO_2-GO hybrid was prepared similarly to nanosized-MoO_2 except that graphene oxide (GO) was added to the $MoCl_5$ solution prior to heat treatment. In detail synthesis, 270 mg anhydrous $MoCl_5$ (Strem Chemicals) was dissolved in a mixture of 5 ml ethanol and 5 ml deionized water. Then 10 ml of GO solution (30 mg of GO in DI water) was added to the first solution. Then this solution was hydrothermally treated at 180°C for 6 hrs. The GO was synthesized by the modified Hummer's method[62, 63]. Microsized-MoO_2 was prepared by high energy ball milling (24 hrs, 300 rpm) commercial MoO_2 powder (Sigma Aldrich).

Chapter 3.3.2. Structural and chemical characterization

Powder X-ray Diffraction (XRD) - XRD was performed in a Rigaku Miniflex-II diffractometer operating with Cu-Kα (λ=1.54 Å) radiation using (30 kV, 15 mA, 0.05° step size). The XRD patterns were collected in the range of $10° < 2\theta < 80°$. Transmission electron microscopy (TEM) was performed using a FEI Technai T12 operating at 120 kV. Raman spectroscopy was carried out using a Renishaw InVia micro-Raman spectrometer (514 nm laser source) equipped with an 1800 lines mm^{-1} grating. Thermogravimetric analysis (TGA) was performed using the SDT Q600 from TA Instruments. The samples were heated to 650 °C at a rate of 10 °C min^{-1} in air (flow rate: 100 ml/min). X-ray Photoelectron Spectroscopy (XPS) was performed using a Kratos Axis Ultra DLD with a monochromatic Al (Kα) radiation source. The charge neutralizer filament was used to control charging of the sample, 20 eV pass energy was used with a 0.05 eV step size, and scans were calibrated using the C 1s peak shifted to 284.8 eV. The samples were etched with an Ar beam (raster size 5 mm x 5 mm) for 30 seconds.

Chapter 3.3.3. Electrochemical characterization

Ex situ XRD – *Ex situ* XRD measurements were performed on nanosized-MoO_2 and microsized-MoO_2 slurry electrodes (termed 'thick electrodes', *vide infra*) after electrochemical cycling. The electrode slurries were prepared by mixing MoO_2 active materials with carbon black (Alfa Aesar) and polyvinylidene fluoride (PVdF, Kynar) in N-methyl-2-pyrrolidinone (NMP, Sigma Aldrich) in an 80:10:10 weight ratio. These slurries were coated on stainless steel foils by doctor blading and subsequently dried in vacuum at 110 °C for 24 hrs giving mass loadings of ~ 1 mg/cm^2. These working electrodes were cycled in 1M $LiClO_4$ in propylene carbonate (PC) with lithium metal foils used as reference and counter electrode. The MoO_2 electrodes were cycled galvanostatically at C/10-rate (C-rate based on a theoretical capacity of 210 mAh/g) to the

desired potential followed by a potentiostatic hold to reach equilibrium. The cycled working electrodes were washed thoroughly with dimethyl carbonate (DMC, Sigma-Aldrich) before sealing the samples in a 64 μm polyimide pouch to prevent exposure to the environment. X-ray diffraction was performed in a Bruker Discover D8 in reflection geometry operating with Cu Kα (λ = 1.5418 Å) using a 0.035° step size, a voltage of 40kV, and a current of 40 mA. XRD patterns were recorded in the range of $24° < 2\theta < 43°$.

Electrochemical analysis - Both thin film and thick film electrodes were prepared. The former contained no carbon or binder as this enabled us to determine the electrochemical properties of the MoO_2 material or the RGO-MoO_2 directly. With these electrodes, each MoO_2 sample (~ 30 μg) was drop cast on an oxygen plasma treated stainless steel foil (1 cm^2) and dried under vacuum at 120 °C for 1 hour. The mass of these samples was measured using a microbalance (Cahn C-31, 0.1 μg). Electrochemical measurements of the thin film electrodes were carried out in a three-electrode cell using lithium foil as a counter and reference electrode in 1M $LiClO_4$ in propylene carbonate (PC). Cyclic voltammetry was used to investigate the capacity and kinetics of MoO_2 between 1.1 and 3.0 V (vs. Li/Li^+) using a PAR EG&G 273A Potentiostat. All tests were performed in an Ar-filled glovebox. Thick electrodes were prepared as described above. Electrochemical testing of the thick film electrodes was performed using a Swagelok cell. The cells were assembled using these thick film electrodes as the working electrode, lithium metal as a reference and counter electrode, a glass fiber separator (Advantec), and 1M $LiClO_4$ in PC was used as the electrolyte. Assembly of the Swagelok cells was done in an Argon-filled glovebox.

Chapter 3.4. Results and discussion

Figure 3.2 (a) and (b) show XRD patterns of hydrothermally synthesized MoO_2 and ball milled MoO_2 particles. Both XRD patterns can be indexed as monoclinic MoO_2 (space group = $P2_1/c$, JCPDS 032-0671) without the presence of secondary phases. The diffraction peaks of hydrothermally synthesized MoO_2 particles were broader compared to the much narrower peaks of the ball milled MoO_2 particles, indicating that the crystallite size of the hydrothermally synthesized MoO_2 particles (nanosized-MoO_2) were much smaller than ball milled MoO_2 particles (microsized-MoO_2). The shape and size of nanosized-MoO_2 and microsized-MoO_2 were observed by TEM. Figure 3.3 (a) and (b) show TEM images of nanosized-MoO_2 which confirmed that these MoO_2 particles have spherical like shape with sizes in the range of 10 to 15 nanometers. Figure 3.3 (c) and 3.3 (d) show the TEM images of microsized-MoO_2 particles that consist of particles that are 0.2 to 1 μm in size.

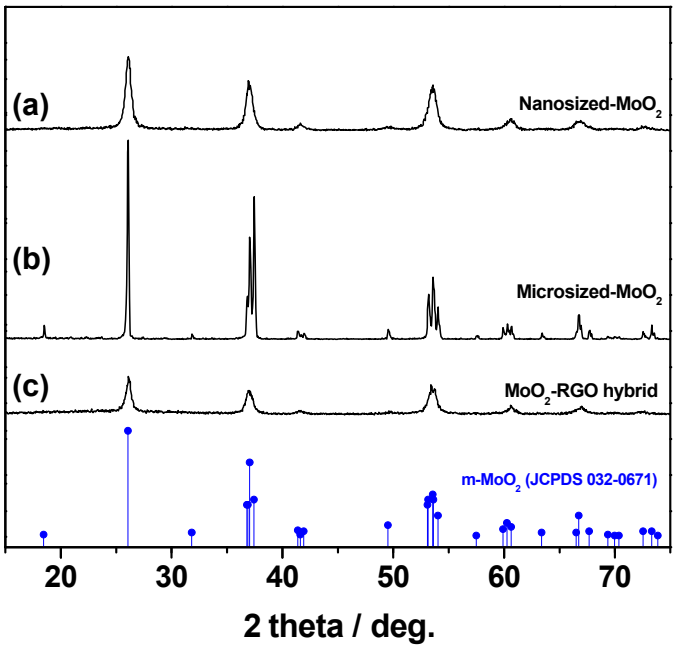

Figure 3.2. XRD patterns of (a) nanosized-MoO_2, (b) microsized-MoO_2, and (c) MoO_2-RGO hybrid.

Ex situ XRD was used to investigate the relationship between structure and electrochemistry for microsized- and nanosized-MoO_2. These experiments were carried out using thick composite electrodes (active material, binder, and carbon) in which loading of the MoO_2 electrodes was ~1 mg/cm^2. As mentioned previously, cycling in a voltage window between 1.1 and 3.0 V (vs Li/Li$^+$) corresponds to Li-ion insertion into the channels of monoclinic-MoO_2. The monoclinic phase is reported to be a metallic conductor[48] because Mo-Mo pairing along the Mo atom chains in the lattice gives rise to metallic conductivity. Insertion of Li-ions into the monoclinic phase of MoO_2 has been reported to lead to a phase transformation from the monoclinic to the orthorhombic phase when the amount of Li (x in Li_xMoO_2) is above 0.5[51]. This phase change disrupts the Mo-Mo pairing and consequently lowers the electronic conductivity[51].

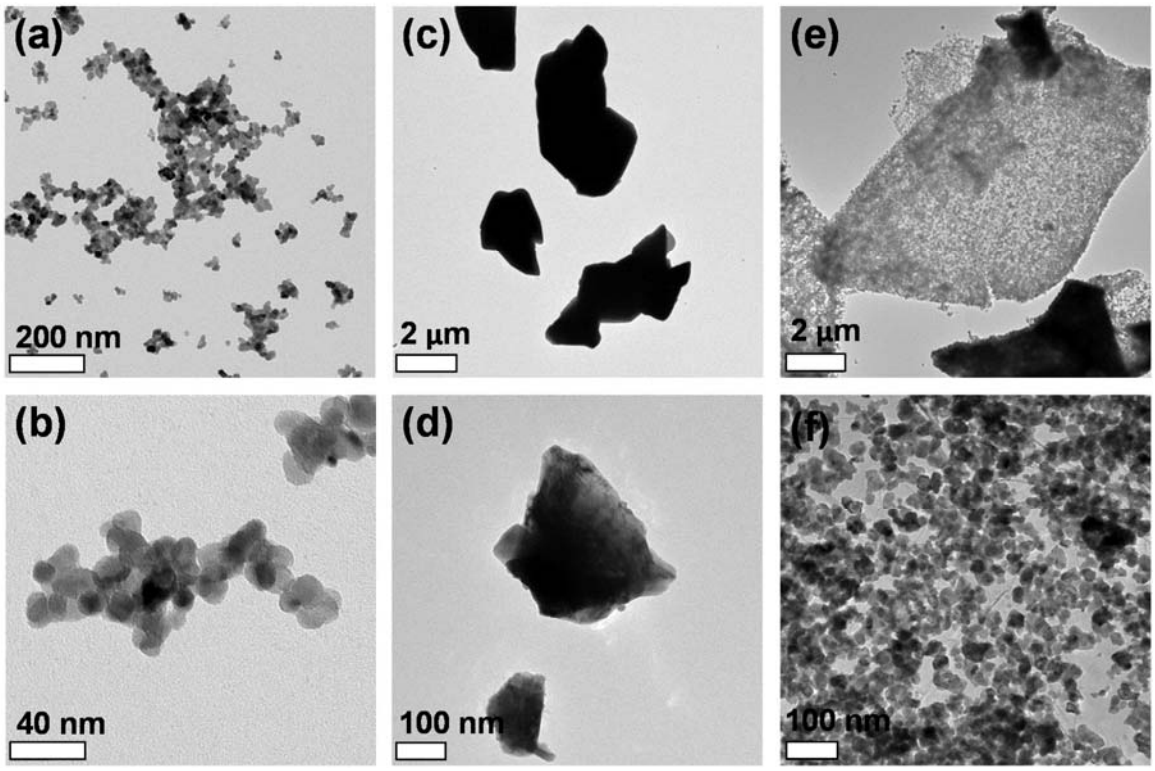

Figure 3.3. TEM images of (a, b) nanosized-MoO_2, (c, d) microsized-MoO_2, (e, f) MoO_2-RGO hybrid.

Figure 3.4 (a) displays the *ex situ* XRD patterns associated with the galvanostatic charge and discharge profiles for microsized-MoO_2. The galvanostatic plot in Figure 3.4 (a) shows two plateau regions which are related to two different Li^+ ion sites along the MoO_2 tunnels. In the diffraction patterns shown in Figure 3.4 (a), it was confirmed that during discharge a new phase (orthorhombic) appeared at 1.25 V (vs. Li/Li^+) and that during charge, this phase (orthorhombic) completely returned to the initial phase (monoclinic) at 1.85 V. The first order nature of the phase transition is clearly evidenced by the discontinuous change in peak position, and by the coexistence of both phases at voltages near the transition point. The phase transformation occurring with microsized-MoO_2 precludes its use as an electrode material for capacitive energy storage[13]. Markedly different electrochemically induced structural behavior occurs for nanosized-MoO_2. Specifically, the monoclinic-to-orthorhombic phase transition seen in microsized-MoO_2 is completely suppressed in nanosized-MoO_2 (Figure 3.4 (b)). We postulate that suppression of the phase transition is a nanosize effect, in which nucleation of the new phase in the confined space of the nanoparticle is unfavorable, resulting in an increase in transition voltage. Similar nanosize effects have been demonstrated in other nanocrystal systems. For example, in CdSe nanocrystals, the transition pressure for pressure-induced solid-solid phase transitions becomes elevated in finite size systems[64]. Also enhanced solubility of Li in the anatase Li_xTiO_2 nanoparticles was observed in the previous study[65]. This is because molar Gibbs free energy for mixing (ΔG_{mix}) increases as the particles size decreases. In detail, ΔG_{mix} increases with the term '$A(x)\gamma_A/(v_{Li}V)$' which is related to the energy penalty from the strain of a phase boundary and this term increases with decreasing particle sizes. This is because the surface of the interface between two phases, A(x), will scale with r^2 and the volume, V, with r^3, where r is the particle radius[65]. (γ_A: surface tension, v_{Li}: molar volume of Li-ion)

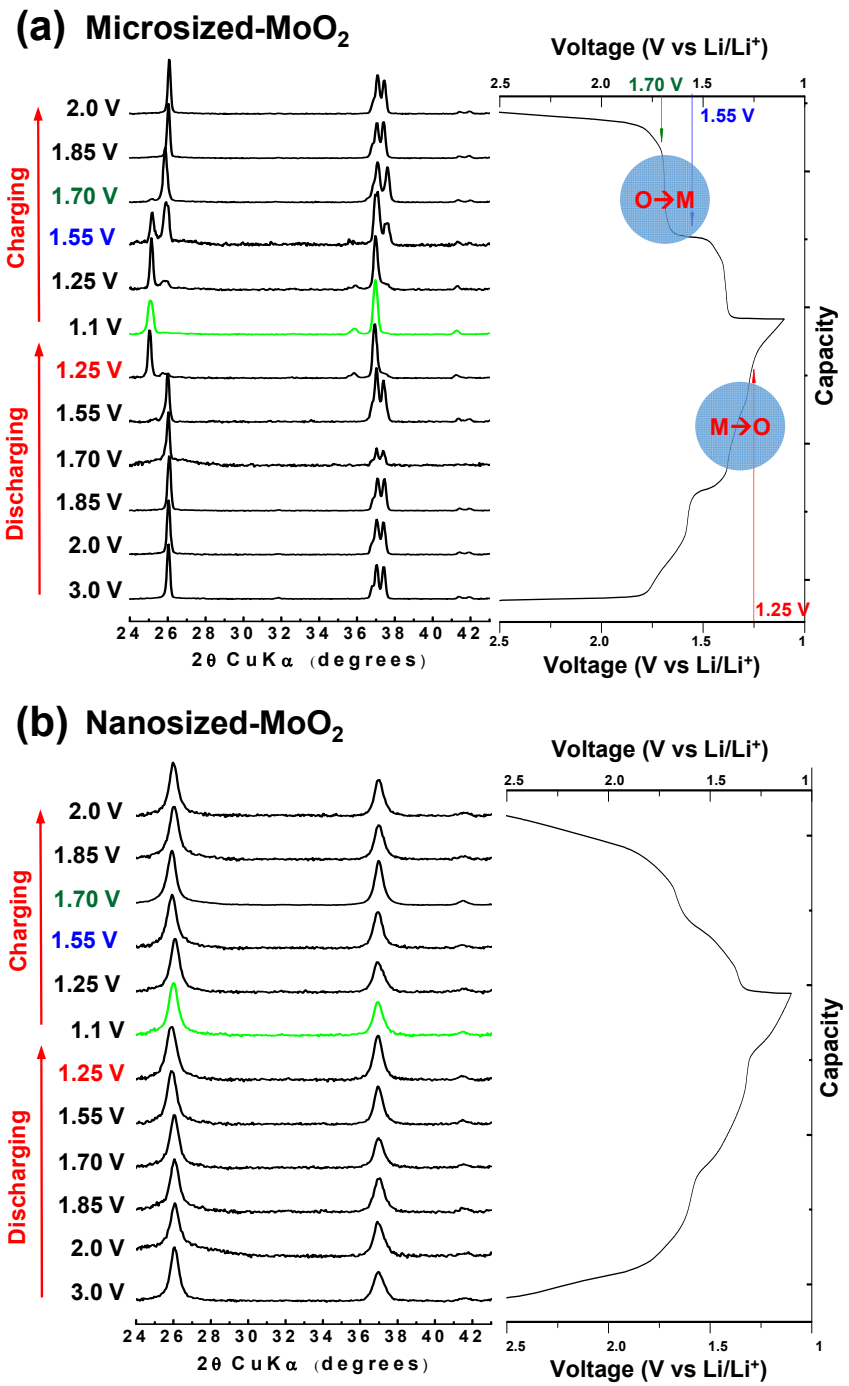

Figure 3.4. *Ex situ* XRD patterns of (a) microsized-MoO_2 and (b) nanosized-MoO_2 collected at various potentials between 1.1 – 3V (V vs. Li/Li^+). The galvanostatic plots (C/10) are included in order to compare the *ex situ* XRD patterns with the electrochemical signatures.

While the phase transition is suppressed in nanosized-MoO_2, some small and continuous changes in XRD peak positions are observed, with a small lattice expansion upon Li^+ insertion, followed by a recompression on Li^+ extraction. These small changes imply that the 1-D tunnels provide fast diffusion pathways and ample Li^+ sites without need for structural rearrangement. In establishing the relationship between electrochemical properties and structural variations, the complete suppression of a first order solid-solid phase transition implies that nanosized-MoO_2 behaves as an extrinsic pseudocapacitor material.

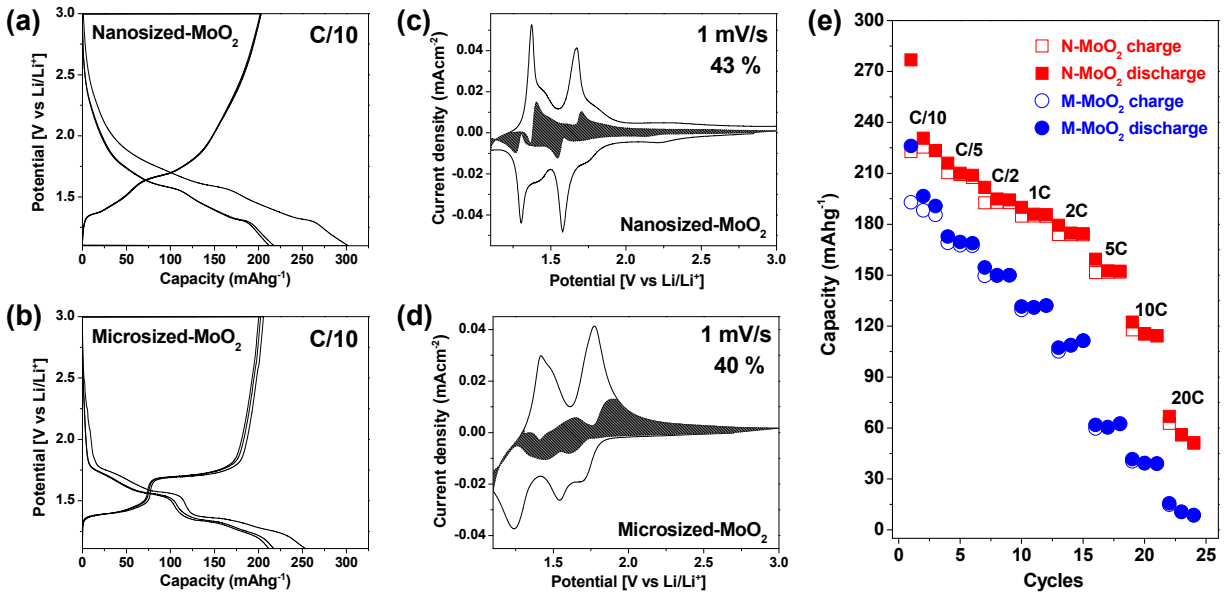

Figure 3.5. Electrochemical performance characteristics: galvanostatic charge-discharge profile at C/10 rate and kinetic analysis for nanosized-MoO_2 (a, c) and microsized-MoO_2 (b, d), and (e) rate capability comparisons between nanosized-MoO_2 (N-MoO_2) and microsized-MoO_2 (M-MoO_2) with the thick electrodes.

Galvanostatic cycling and cyclic voltammetry measurements were carried out on both thin and thick film electrodes of nanosized-MoO_2 and microsized-MoO_2 to provide greater insight regarding their respective electrochemical properties. Figure 3.5 (a) and (b) (thick film electrodes) show galvanostatic charge/discharge cycling at C/10 for nanosized-MoO_2 and microsized-MoO_2, respectively. Higher capacity is observed for the first discharge in nanosized-MoO_2 due to a greater amount of solid electrolyte interface (SEI) layer being formed on the nanoparticles. The absence of a phase transformation in nanosized-MoO_2 leads to a sloped voltage profile which is a typical feature of pseudocapacitive charge storage[13] (Figure 3.5 (a)). In contrast, the voltage profile in microsized-MoO_2 has two plateau regions during the charge and discharge process (Figure 3.5 (b)). Figure 3.5 (c) and (d) display voltammetric sweeps for thin film electrodes at 1 mV/s where the measured current has been separated into two parts; one is diffusion-controlled ($\upsilon^{-½}$ dependence) and the other is capacitor-like (υ dependence)[66, 67]. The grey areas in Figure 3.5 (c) and (d) represent the potential dependence for the latter and show that there is very little difference between the two materials; approximately 60 % of the charge storage was diffusion-controlled in both nanosized-MoO_2 and microsized-MoO_2. Even though both materials show numerically similar diffusion-controlled current contributions, we show below that processes other than Li^+ diffusion are limiting the kinetics in the nanosized-MoO_2 sample. Fundamentally, redox processes in nanosized-MoO_2 are pseudocapacitive, whereas the process in microsized-MoO_2 is not.

Thick electrode samples (~1 mg/cm^2) were prepared to examine the effect of higher mass loadings as these results are more pertinent for device applications. As shown in Figure 4 (e), the nanosized-MoO_2 showed higher capacity and better rate capability than microsized-MoO_2. Nanosized-MoO_2 stored more than 100 mAh/g at a 10 C-rate which represents fast

charge/discharge kinetics for a battery material. Microsized-MoO_2 exhibits ~ 40 mAh/g at this C-rate, thus substantiating the better kinetic properties for nanosized-MoO_2. It is evident, however, that nanosized-MoO_2 has limitations as the capacity dropped to about 50 mAh/g at 20 C-rate. Even though nanosized-MoO_2 exhibits several characteristic features of pseudocapacitance such as sloping voltage profiles, no phase transformation, and small peak voltage separation (Figure 3.5 (c)), the material does not meet a key criterion for high-power devices applications, where the materials need to be able to store substantial amounts of charge in 1 min (~ 60 C-rate) or less[4]. For this reason, in the next section we explore the surface chemistry of these particles as a way to explain this apparent contradiction.

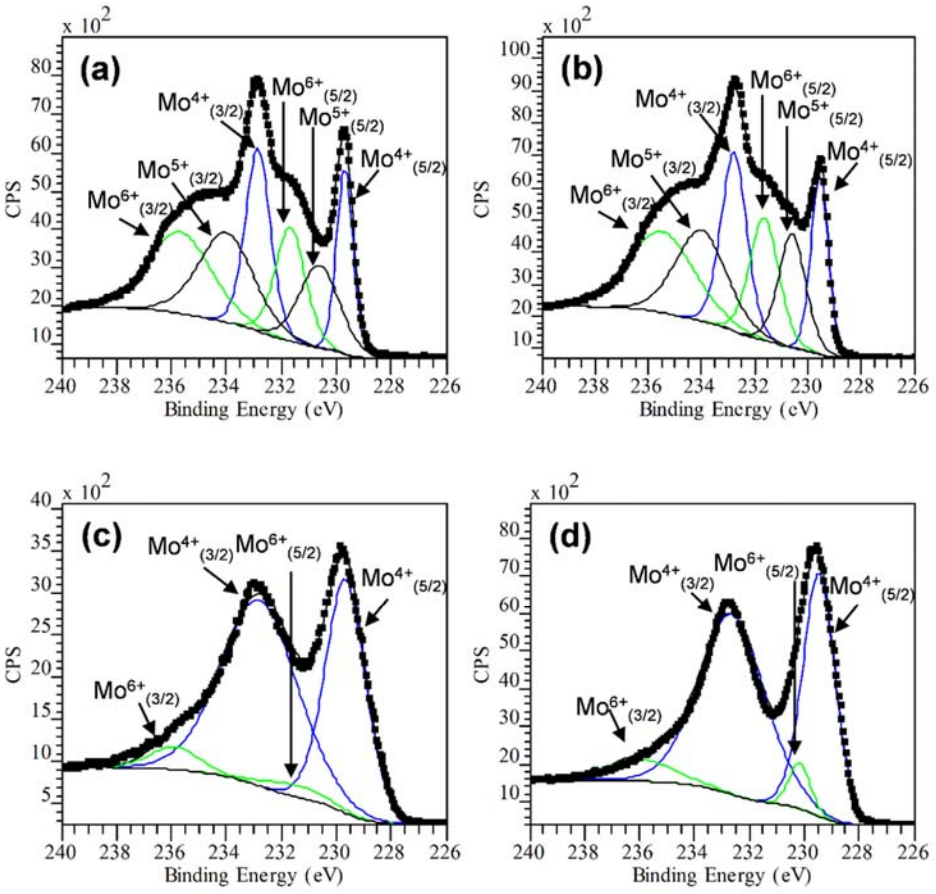

Figure 3.6. XPS spectra of (a) nanosized-MoO_2 and (b) RGO-MoO_2 composites and XPS spectra after plasma etching of (c) nanosized-MoO_2 (d) RGO-MoO_2 composites.

Surface oxidation of nanosized-MoO_2

There is an indication in the literature that the MoO_2 nanoparticles are susceptible to surface oxidation. Monoclinic MoO_2 is a metallic conductor, however, the material oxidizes readily because of the high surface area of the MoO_2 nanoparticles[68]. The surface oxide coating results in formation of a less electronically conducting material which critically impedes the charge transfer reactions. In order to examine this issue, XPS measurements were performed on nanosized-MoO_2. Indeed, higher oxidation states of Mo (Mo^{5+} and Mo^{6+}) were observed on the surface of nanosized-MoO_2. After argon-ion etching, these higher oxidation states decrease significantly, leaving Mo^{4+} as the dominant oxidation state (as expected for MoO_2), thus confirming that the oxidized Mo is indeed in surface sites (Figures 3.6 (a) and (c)). These results allow us to understand the electrochemical data in Figure 3.5: both microsized and nanosized samples show predominantly diffusion controlled behavior, but it stems from very different phenomena. Charge transfer rates for nanosized-MoO_2 are limited by the poorly conducting surface layer, while the kinetics in micron sized particles are likely limited by the slow kinetics of solid-solid phase transitions.

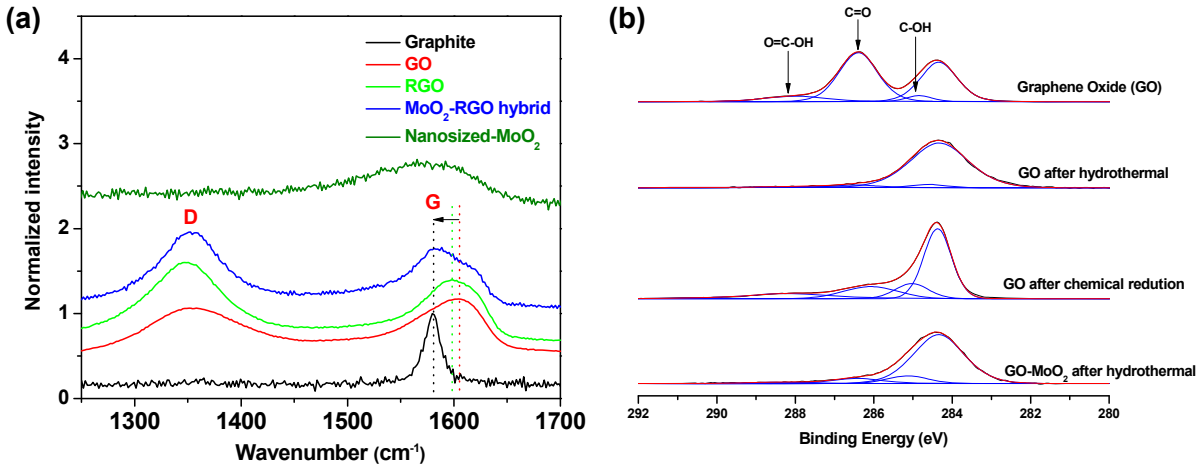

Figure 3.7. (a) Raman spectra comparison (b) high resolution carbon XPS spectra of GO, RGO-MoO_2, and RGO reduced by various methods

Hybrid material with graphene oxide

One route to solving the problem of surface oxidation in nanosized-MoO_2, is to synthesize MoO_2 nanoparticles on reduced graphene oxide (RGO) sheets. Prior research on MoO_2 with graphene or carbon was focused on improving the stability of conversion reactions[69, 70, 71, 72], but the same system can be used to address the oxidation problems discussed above. High angle XRD of as-synthesized MoO_2-RGO hybrid materials (Figure 3.2 (c)) can again be indexed as monoclinic MoO_2 (JCPDS 032-0671) with similar peak broadening to that observed in the XRD pattern of nanosized-MoO_2 in the absence of RGO. TEM images (Figures 3.3 (e) and (f)) indicate there is uniform nucleation and growth of 15 to 20 nm MoO_2 nanoparticles on the RGO sheets. XPS spectra for MoO_2-RGO (Figures 3.6 (b) and (d) indicate that MoO_2 nanoparticles on the RGO sheets also have an oxidized shell on the surface that can again be removed by argon-ion etching, but the fact that the MoO_2 appears to nucleate directly on the GO means that the interface between RGO and MoO_2 is likely to remain unoxidized and thus highly conductive.

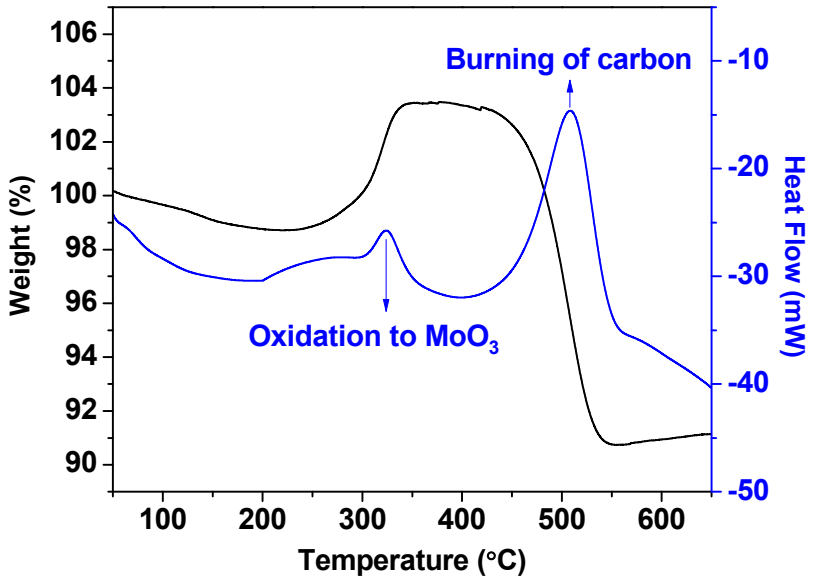

Figure 3.8. TGA analysis on MoO_2-RGO hybrid.

Another advantage of this system is the ease of synthesis. The use of hydrothermal reactions to reduce the GO has been shown to produce materials with a high electrical conductivity. Following the work of Zhou et. al.[73] we thus reduced GO to RGO during the same hydrothermal reaction used to synthesize the nanosized-MoO_2, without the need for an additional reducing agent. Raman spectroscopy and XPS were used to characterize the reduction of GO in the MoO_2-RGO hybrid. The Raman spectrum for the MoO_2-RGO hybrid shown in Figure 3.7 (a) is compared with spectra of GO and RGO. A key characteristic feature of Raman spectra in RGO is that the D peak intensity (I_D) is higher than G peak intensity (I_G) due to the presence of unpaired defects remaining after removal of the oxygen containing functional group[74]. Both the RGO sample shown in Figure 3.7 (a) and the MoO_2-RGO hybrid exhibit higher I_D than I_G. Another feature in the Raman spectrum for the MoO_2-RGO hybrid is a shift of the G peak to lower wavenumber. This is due to the restoration of the conjugation which can be seen from the Raman spectra[75]. XPS data further confirms the reduction of GO to RGO by showing that the majority of the oxygen is removed from the carbon (Figure 3.7 (b)). Finally we used TGA results (Figure 3.8) to determine the amount of RGO in the MoO_2-RGO hybrid. The weight increase observed at 350°C was due to the oxidation to MoO_3 while the weight decrease at 450°C was due to the oxidation and subsequent volatilization of carbon. The amount of RGO was determined to be 12 % from the weight change of the MoO_2-RGO material.

Electrochemistry of the MoO_2-RGO hybrid

Cyclic voltammetry (CV) experiments carried out with the MoO_2-RGO hybrid show the benefit of the hybrid approach. In comparing the MoO_2-RGO hybrid with nanosized-MoO_2 (Figures 3.9 (a) and (b)), thin film electrodes were used so that we can establish the fundamental properties of the active material (i.e., nanosized-MoO_2 and the MoO_2-RGO hybrid). The results

reported for the hybrid include the weights of both components. The voltammetry scans indicate that each material exhibits oxidation and reduction peaks at comparable potentials (Figures 3.9 (a) and (b)). One interesting difference is that nanosized-MoO_2 exhibits a diminishing current response over the first 10 cycles while the current response increased with cycling for the MoO_2-RGO hybrid. The different behaviors could be the result of more stable SEI formation from the graphene oxide in the MoO_2-RGO hybrid sample[76].

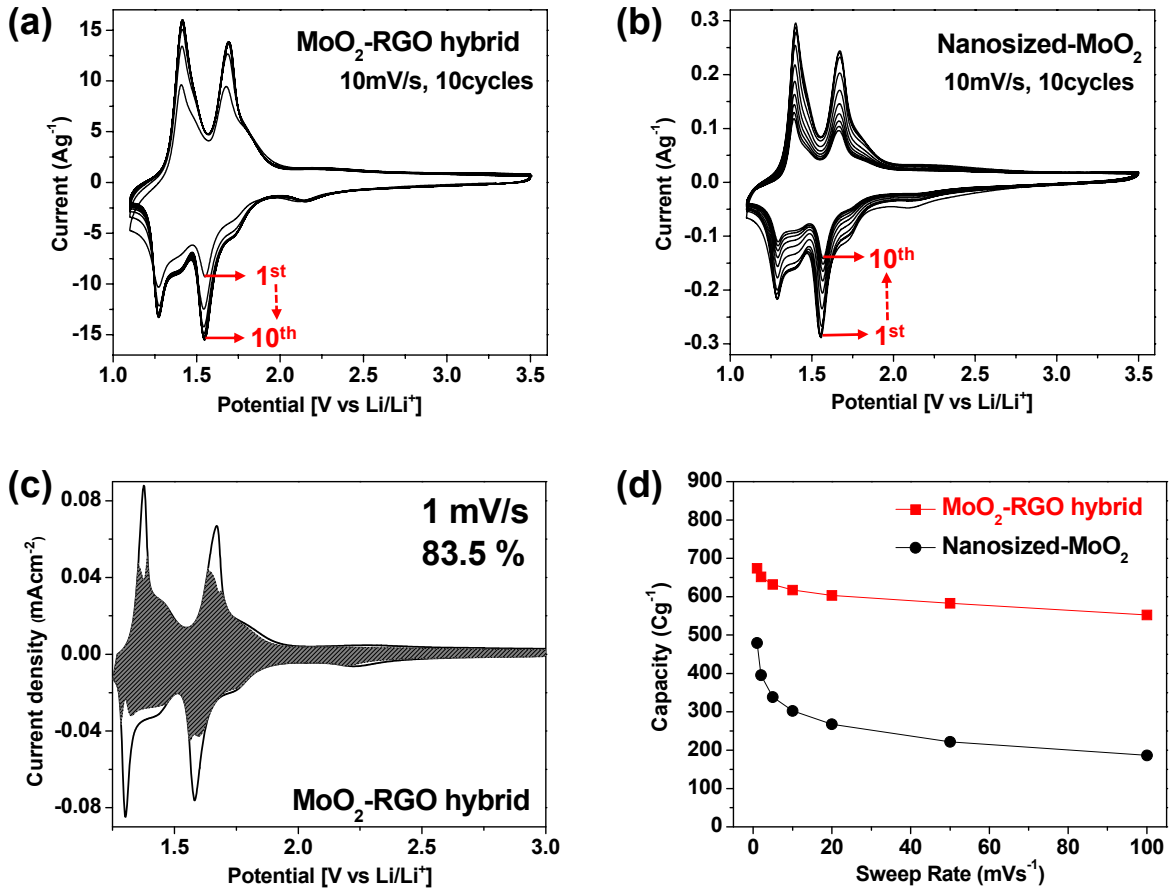

Figure 3.9. Electrochemical performance characteristics with thin film electrodes: cyclic voltammetry at 10 mV/s sweep in (a) MoO_2-RGO hybrid and (b) nanosized-MoO_2, kinetic analysis on (c) MoO_2-RGO hybrid, and (d) rate capability comparisons.

An analysis of the CV in terms of diffusion-controlled and capacitor-like currents shows a significant change from that of Figure 3.5 (c). The fraction of current which is capacitive is more than 80 % for the MoO_2-RGO hybrid (Figure 3.9 (c)), which is about two times greater than that of nanosized-MoO_2. Dispersing the MoO_2 onto RGO circumvents the poor particle-to-particle conductivity that occurs with the oxidized surfaces of the MoO_2 nanoparticles. A better kinetic response is observed for the MoO_2-RGO hybrid because the MoO_2 nanoparticles are directly connected to a conductive scaffold which facilitates the charge transfer process and impedes oxidation at the RGO-MoO_2 interface. Figure 3.9 (d) shows how the mass-normalized charge storage (in C/g) varies with sweep rate. At a sweep rate of 10 mV/s, the MoO_2-RGO hybrid exhibits about two times greater charge storage compared to nanosized-MoO_2 (615 C/g vs. 300 C/g). This level of charge storage corresponds to a specific capacitance of 615 F/g (voltage window of 1 V) for the hybrid material. At 100 mV/s this value has decreased by only ~ 10 % to 550 C/g. Since a 1-electron redox reaction associated with MoO_2 gives 210 mAh/g (756 C/g), these results show that the MoO_2-RGO hybrid is able to charge to nearly 75 % of the theoretical capacity of MoO_2 in < 30 seconds.

To complement the thin film electrode studies, Swagelok cells containing a thick electrode (~1mg/cm^2) of MoO_2-RGO hybrid were assembled. The intent here was to provide a better indication of how this hybrid material would function under conditions closer to those of an operating charge storage device. The results in Figure 3.10 represent the mass-normalized capacities for the active materials, namely nanosized-MoO_2 and the MoO_2-RGO hybrid. The galvanostatic charge-discharge curves shown in Figure 8 (a) exhibit the potential-dependent sloping profile which is characteristic of a pseudocapacitor material. The rate capability for the MoO_2-RGO hybrid is far better than that of nanosized-MoO_2 (Figure 3.10 (b)). This behavior is

especially evident at high rates. At 50C, the MoO_2-RGO hybrid exhibits a discharge capacity of nearly 150 mAh/g while the nanosized-MoO_2 is ~ 25 mAh/g. It is interesting to note that the discharge capacity at C/10 for the MoO_2-RGO hybrid exceeds the theoretical capacity (210 mAh/g) of MoO_2 in this voltage window. The additional capacity arises mainly from the contribution of RGO (35 mAh/g in this voltage range[77]). These results show that the electrochemical performance of nanosized-MoO_2 is greatly enhanced due to the improved charge transfer from the RGO in combination with a more stable SEI layer.

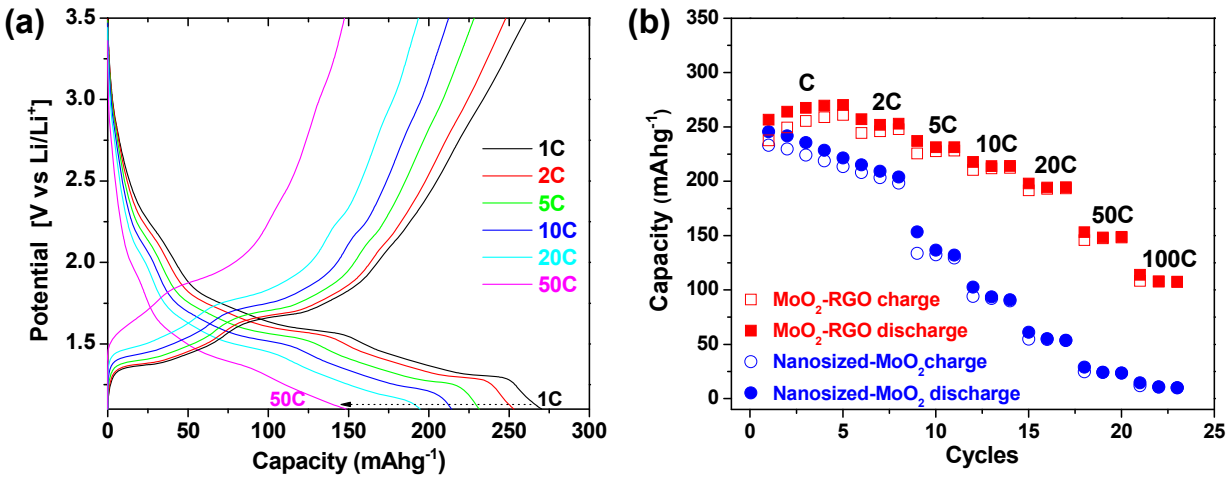

Figure 3.10. Electrochemical performance characteristics with thick electrodes: (a) galvanostatic charge-discharge profiles from 1 – 50 C rate, (b) rate capability comparison between MoO_2-RGO hybrid and nanosized-MoO_2.

Discussion

We have used MoO_2 as a model system in which to provide insight regarding the origins of an extrinsic pseudocapacitor material. Microsized-MoO_2 undergoes a phase transformation upon lithium insertion and exhibits the characteristics of diffusion-controlled insertion/de-

insertion kinetics. In contrast, nanosized-MoO_2 displays several features which are signatures for pseudocapacitive charge storage:[14, 44] No phase transformation is observed upon lithiation (or de-lithiation from Li_xMoO_2) (Figure 3.4 (b)), a sloping voltage profile in galvanostatic experiments (Figure 3.5 (a)) and peak potentials that do not shift significantly with sweep rate (Figure 3.9). One explanation that is often provided for the pseudocapacitive response with nanoscale particles is the large number of surface states available which enable faster lithium ion storage reactions than occur in the bulk material.[13, 46] Thus, it is not surprising that the nanosized-MoO_2 exhibits significantly better kinetics than microsized-MoO_2 (Figure 3.5 (e)). In addition to fast Li-ion storage near the surface, MoO_2 stores charge through intercalation pseudocapacitance, where the entirety of the MoO_2 nanocrystal participates in the faradaic charge storage process. It is evident that the charge storage process is not limited to a thin surface shell of the nanoparticle because nearly 75 % of theoretical capacity is achieved over short charging times. The diffraction data presented in Figure 3.4, allows us to begin to differentiate between diffusion controlled intercalation and intercalation pseudocapacitance based on the corresponding structural changes occurring within the particles. For this system, the rate limiting diffusive step is not apparently Li^+ diffusion within the channel network of MoO_2. Instead it is the diffusive propagation of the monoclinic-to-orthorhombic phase transition front. When that phase transition process is suppressed, Li^+ intercalation can proceed much more quickly. While some structural changes do occur upon Li^+ intercalation (e.g. the diffraction peaks in Figure 3.4 (b) move to smaller 2 values during Li-ion insertion, which indicates that the crystallites undergo a lattice expansion), the change is continuous and thus does not apparently provide a kinetic barrier. In general, MoO_2 provides the clearest picture to date on the changes needed to convert a bulk material that is not pseudocapacitive into an extrinsic pseudocapacitor in finite sized systems.

The data presented here also provides another lesson for the creation of extrinsic pseudocapacitors: even if a system can be created that displays fast Li^+ insertion kinetics, if those kinetics are not accompanied by good electrical conductivity, pseudocapacitive behavior will not result. Here, for pure nanosized-MoO_2, only 40 % of the current was capacitive because MoO_2 is a reduced transition metal oxide that is susceptible to surface oxidation and MoO_3 is quite insulating. MoO_3 layers between grains inhibited electron transport through the network, despite the metallic conductivity of MoO_2. When this oxidation problem was overcome by synthesizing MoO_2-RGO hybrid materials, the kinetics were significantly better, especially at high sweep rates (Figure 3.10 (b)). This behavior occurred even though both pure nanosized-MoO_2 and MoO_2-RGO hybrid samples exhibited similar surface oxidation. We attribute this behavior to having the MoO_2 nanoparticles in direct contact with a conducting scaffold, which prevents oxidation at the one interface that is important for electronic conductivity. Using the hybrid approach, pseudocapacitance was enhanced; the measured current was more than 80 % capacitor-like in nature (Figure 3.9 (c)) and charge storage reached 75 % of the theoretical value of MoO_2 in less than 30 seconds (Figure 3.9 (d)).

A key question with an extrinsic pseudocapacitor material is whether such nanoscale materials can be appropriately scaled to achieve practical electrode architectures. The present work indicates that the hybrid approach is beneficial here. The morphology seems ideal in that MoO_2 nanoparticles are exposed to the electrolyte and yet are attached to the RGO conducting scaffold, which provides effective 'wiring' to the electrode. Fast kinetics are achieved with active material loadings of 1 mg/cm^2 (Figure 3.10). A reversible capacity of nearly 150 mAh/g at 50C clearly demonstrates that hybrid materials can be scaled with little compromise in kinetics.

These results underscore the promise of using extrinsic pseudocapacitance as a strategy for designing electrochemical energy storage devices.

Chapter 3.5. Conclusion

The present work uses MoO_2 as a model system in which to characterize the development of an extrinsic pseudocapacitor material. Unlike microsized-MoO_2, nanosized-MoO_2 does not undergo a monoclinic-to-orthorhombic phase transformation during the lithium intercalation process. As a nanoscale material, MoO_2 possesses electrochemical features representative of pseudocapacitive behavior including a sloping voltage profile rather than flat discharge curves and peak potentials that do not shift significantly with sweep rate. Moreover, nanosized-MoO_2 exhibits significantly better charge storage kinetics than microsized-MoO_2, a fact that likely arises because suppression of the monoclinic-to-orthorhombic phase transformation preserves ion diffusion tunnels in the monoclinic structure, which provide pathways for fast ion transport. XPS studies show that nanosized-MoO_2 is susceptible to surface oxidation, which limits the high power capability of the pure material. This limitation is overcome by synthesizing MoO_2-RGO hybrid materials in which monoclinic MoO_2 nanoparticles (15 to 20 nm) are attached to the conducting RGO scaffold. Only a relatively small fraction of RGO (12 wt %) improves the high rate charge storage properties, leading to lithium capacities of nearly 150 mAh/g at 50C. The hybrid approach demonstrates that the extrinsic pseudocapacitor properties of MoO_2 can be extended to practical electrode architectures, thus facilitating the design of electrodes containing pseudocapacitive materials.

Chapter 4. $Na_{1.5}VPO_{4.8}F_{0.7}$ nanoparticles for high rate, high voltage sodium ion battery

Chapter 4.1. Introduction

Research on the lithium ion batteries (LIBs) began in the early 1980s, which was then commercialized in 1991 by Sony. The first commercialized LIBs were comprised of a carbon (graphite) anode and $LiCoO_2$ cathode, separated by a lithium-ion conducting electrolyte. In the early stages of this technology's commercialization, LIBs were used primarily for energy storage for applications in the area of portable electronics. Continuous demand for high performance LIBs has led to the development of many cathode materials for increasing the energy and power density as well as cycling performance. Consequently, the cost of developing LIBs has now become an issue as this technology is used to power electric vehicles [2]. In addition, there is now a demand for large-scale applications, in particular, for electric grid applications, where batteries are expected to help with peak demand and load leveling when used in conjunction with renewable energy sources such as solar and wind[7].

The high manufacturing cost of LIBs is a concern for future applications. As shown in Figure 4.1, lithium is not an abundant element and its price has been gradually increasing during the last decade. In addition, lithium resources are mainly imported from South America and this can control the economics of LIBs in the future[2]. In contrast, sodium is one of the most abundant elements (Figure) and sodium resources can be found in the Earth's crust as well as in the ocean. In addition, sodium ions show similar electrochemical intercalation chemistry as that of lithium ions and potentially can achieve energy densities on par with LIBs. These advantages make sodium ion batteries (SIBs) as a promising technology to replace current energy storage devices based on LIBs.

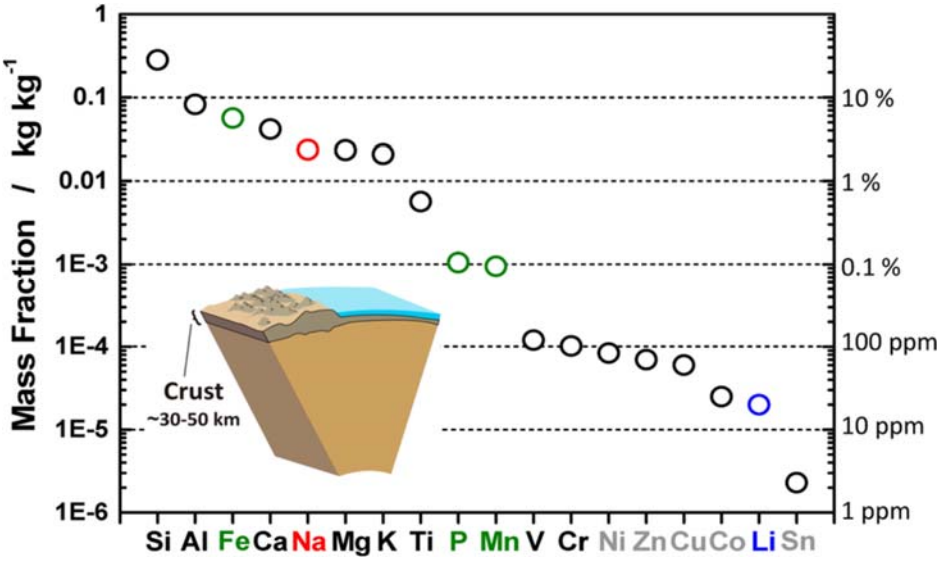

Figure 4.1. Elemental abundance in the Earth's crust[2].

Research on LIBs and SIBs started in the same era however the low energy density of SIBs, due to their low standard electrochemical potential (Na: 2.71 V, Li: 3.04 V), resulted in a loss of interest and for the next several decades, research mainly focused on LIBs. In addition, with its larger size, sodium ions cannot intercalate into graphite, which is the most commonly used negative electrode material. Graphite has several advantages: (i) Low and flat operating potential (0.1 – 0.2 V vs Li/Li^+), (ii) high reversible capacity (theoretical capacity of 372 mAh/g), (iii) low cost. Several candidate materials[78, 79, 80] were investigated for SIBs anode but their capacity was less than that of graphite in LIBs. Fortunately, the discovery of hard carbon[81] which can reversibly intercalate (theoretically 300 mAh/g) sodium ions, increased the feasibility of SIBs. As for the cathode materials, new chemistries based on $NaFeO_2$ that utilize Fe^{3+}/Fe^{4+} redox couple, have made SIBs more attractive as an alternative for LIBs [82]. In addition, the relatively large ion size of Na^+ leads to more candidate materials suitable as cathodes for SIBs because the ion size gap between sodium and 3d transition metal has resulted in a rich literature

of many different layered materials. Thus various crystal structures in the form of polyanionic compounds have been found for sodium systems[2].

Category	Lithium	Sodium
Cation radius (Å)	**0.76**	**1.06**
Atomic weight	**6.9 g/mol**	**23 g/mol**
E° (vs. Li/Li^+)	**0**	**0.3 V**
Capacity (mAh/g) metal	**3829**	**1165**
Capacity (mAh/cm^3) metal	**2062**	**1132**
Cost, carbonates	**$ 6000/ton**	**$ 200/ton**

Table 4.1. Comparison between lithium and sodium[2].

In this research, I focused on high voltage positive electrode materials (Figure 4.2) since intrinsically low standard electrochemical potentials lead to low energy densities. This problem can be solved with the choice of a high potential positive electrode material for SIBs. Among the possible candidate materials, the sodium vanadium fluorophosphate system ($Na_{1.5}VPO_4F_{0.5}$) reported in 2006[83] has been widely investigated because of its high redox potential and reasonable capacity (theoretical capacity: 130 mAh/g)[84, 85, 86, 87, 88]. In order to increase the theoretical capacity of this system, recent research has shown that the $Na_{1.5}VPO_{4.8}F_{0.7}$ system, which has the same crystal structure as $Na_{1.5}VPO_4F_{0.5}$, has more reduced vanadium oxidation states ($V^{3.8+}$) when replacing some of oxygen with fluorine.[4, 89]. For this system, high temperature solid state reaction has been the primary route for obtaining this material and this results in large particle sizes (> 1μm), which limits the rate capability of this material. Thus in

this study, we tried to solve the slow kinetics problem of sodium ion transport by decreasing particle size.

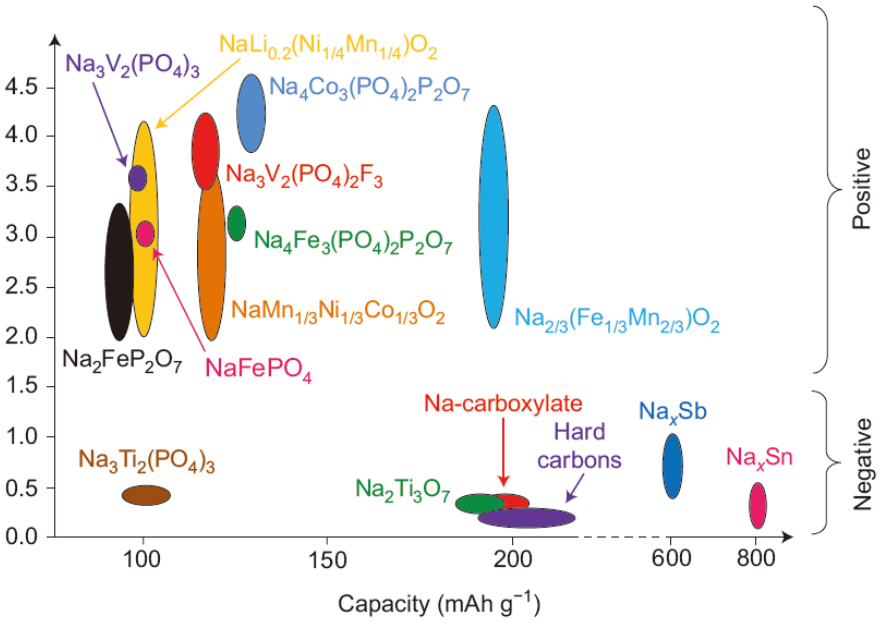

Figure 4.2. Candidate electrode materials for SIBs depending on their voltage and capacity[3]

Chapter 4.2. Technical background

Chapter 4.2.1 $Na_{1.5}VPO_5F_{1.5}$ family systems for sodium-ion batteries

Sodium super ionic conductor (NASICONs) type phases have exhibited attractive lithium and sodium insertion/extraction characteristics due to their open framework enabling fast diffusion of mobile ions[90, 91, 92, 93] Among them, a vanadium-containing fluorophosphate compound, $Na_{1.5}VPO_5F_{0.5}$, has been investigated with many attractive features such as 1.5 mobile ions (Na^+) per transition metal, the presence of multivalent transition metal ions, and an open crystal structure with a high redox voltage (3.8 V vs Na/Na^+)[83]. $Na_{1.5}VPO_5F_{0.5}$ has a

pseudo-layered structure in which the sodium and vanadium layers are roughly separated in an alternate manner along the c direction (Figure 4.3).

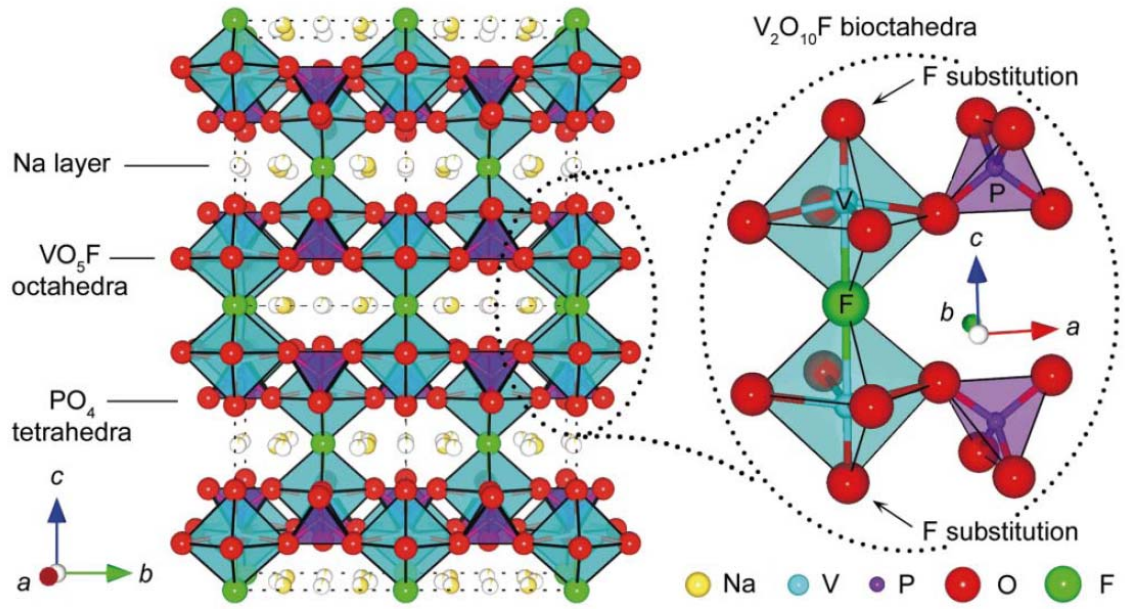

Figure 4.3. Crystal structure of $Na_{1.5}VPO_4F_{0.5}$ system[4]

This framework consists of VO_5F and PO_4 units and bridging fluorine ions to link two VO_5F octahedra to form a $V_2O_{10}F$ bioctahedron[4, 83]. The $V_2O_{10}F$ units are continuously connected following the *ab* plane via PO_4 tetrahedra sharing oxygen atoms and this forms an open framework for Na^+ ion intercalation[4]. However, this material can utilize only one electron via the V^{4+}/V^{5+} redox couple and this results in a relatively low theoretical energy density (130 mAh/g). In order to increase the theoretical capacity, $Na_{1.5}VPO_{4.8}F_{0.7}$ was prepared by controlling the stoichiometry ratio between oxygen and fluorine while keeping the original crystal structure[89]. In this study, $Na_{1.5}VPO_{4.8}F_{0.7}$ showed high rate capability with reasonable capacity (~ 120 mAh/g).

Also, a lithium derivative ($Li_{1.1}Na_{0.4}VPO_{4.8}F_{0.7}$) was prepared by ion-exchange between Na^+ and Li^+ for a LIBs cathode[4]. $Li_{1.1}Na_{0.4}VPO_{4.8}F_{0.7}$ could achieve a high capacity of 153 mAh/g at a C/20 rate as well as high voltage (4 V) and high rate capability (100 mAh/g at 25 C rate)[4].

Chapter 4.2.2. The effect of fluoroethylene carbonate (FEC) as an electrolyte additive

Previous studies on the use of electrolyte additives in LIBs showed that these are necessary for practical LIBs[94, 95, 96]. Recently, electrolyte additives for LIBs such as fluoroethylene carbonate (FEC)[97], transdifuoroethyhene carbonate (DFEC)[98], and ethylene sulfite (ES)[99] were also investigated for SIBs[100]. In this previous study, when FEC was used as an electrolyte additive (~ 5%) in the electrolyte (1M $NaClO_4$ in propylene carbonate), the coulombic efficiency and cyclability of hard carbon negative electrode were greatly improved. Komaba et al. explain this by stating that the FEC addition enables the modification of the solid electrolyte interphase (SEI)[100]. In addition, these authors observed some decomposition compounds such as sodium propyl carbonate only in the cell with FEC-free electrolyte. This explains the effect of decomposition suppression in FEC containing electrolyte and leads to an increase in coulombic efficiency by avoiding undesirable reactions between sodium metal and the organic solvent (PC). In the same study, it was shown that the addition of FEC could improve the stability of positive electrodes such as $NaNi_{0.5}Mn_{0.5}O_2$. Without FEC, sodium propyl carbonate from the reductive decomposition of PC started to be oxidized at above 2.8 V (vs. Na/Na^+) and this resulted in low coulombic efficiency and poor cyclability. Thus in our study, we used 1M $LiClO_4$ PC electrolyte with and without FEC and compared the electrochemistry of $Na_{1.5}VPO_{4.8}F_{0.7}$.

Chapter 4.3. Experimental

Chapter 4.3.1. The synthesis of $Na_{1.5}VPO_{4.8}F_{0.7}$ nanoparticles

Preparation of precursor powder - The synthesis of the precursor material was modified from the previously reported synthesis of $NaVOPO_4$[101]. Equal amounts of NH_4VO_3 (Sigma-Aldrich), NaAc (Sigma-Aldrich), $(NH_4)_2HPO_4$ (Sigma-Aldrich), and citric acid (Sigma-Aldrich) were mixed by grinding with a mortar and pestle. The mixture was transferred into a vial and stirred with distilled water to form a sticky uniform slurry. The slurry was dried at 80 °C until a blue gel was formed. The gel was then heated at 300 °C for 4hr and subsequently at 500 °C for 4 hr in air. The resulting $NaVOPO_4$ powder was green. For the synthesis of $Na_{1.5}VPO_{4.8}F_{0.7}$ nanoparticles, after heat treatment at 300 °C, this gel was heated at 500 °C for 1hr in air to retain residual carbon on the particles.

Crystalline $Na_{1.5}VPO_{4.8}F_{0.7}$ nanoparticles synthesis – 400 mg of as prepared precursor powder (blue colored) was mixed with NaF (Sigma-Aldrich) and NaOH (Sigma-Aldrich) (10:1 ratio) and dissolved in 20 ml of deionized (DI) water. This solution was then sealed in a 45 ml Teflon liner and slid into a stainless steel autoclave and treated at 200 °C for 5 days. After washing with DI water and centrifugation, the particles were then stirred in DI water for 24 hrs to remove possible byproducts (e.g. $NaCO_3$, white color), then dried at 100 °C under vacuum.

Carbon coating of $Na_{1.5}VPO_{4.8}F_{0.7}$ nanoparticles – As prepared $Na_{1.5}VPO_{4.8}F_{0.7}$ nanoparticles were coated with carbon using high energy ball milling (HEBM). Specifically, the $Na_{1.5}VPO_{4.8}F_{0.7}$ nanoparticles were mixed with carbon black (Super P, Alfa Aesar) in a 8:2 ratio using mortar and pestle and ball milled using HEBM (Planetary micro mill PULVERISETTE 7, Fritsch) at 500 rpm for 12 hrs.

Chapter 4.3.2. Structural and chemical characterization

Powder X-ray Diffraction (XRD) - XRD was performed in a Rigaku Miniflex-II diffractometer operating with Cu-Kα (λ=1.54 Å) radiation using (30 kV, 15 mA, 0.05° step size). The XRD patterns were collected in the range of $10° < 2\theta < 80°$. Rietveldt refinement was done by Dr. Guillaume A Muller. Transmission electron microscopy (TEM) was performed using a FEI Technai T12 operating at 120 kV. High resolution-TEM was performed using FEI Titan S/TEM operating at 300 kV. Brunauer-Emmett-Teller (BET) surface areas measurement was performed by using nitrogen adsorption isotherms at 77 K using a gas adsorption analyzer (Micromeritics ASAP 2010). Fourier transform infrared spectroscopy (FT-IR) was measured using FT/IR–670 PLUS (Jasco) in transmission mode using silicon substrates. Thermogravimetric analysis (TGA) was performed using the SDT Q600 from TA Instruments to measure the amount of carbon. The samples were heated to 650 °C at a rate of 10 °C min^{-1} in air (flow rate: 100 ml/min) and stayed at this temperature for 15min.

Chapter 4.3.3. Electrochemical characterization

Electrochemical analysis **-** For electrochemical characterization, carbon coated $Na_{1.5}VPO_{4.8}F_{1.5}$ nanoparticles were mixed with polyvinylidenefluoride (PVDF) dissolved in N-methyl-2-pyrrolidone (NMP) with 9:1 ratio and this slurry was cast onto a carbon coated aluminum foil using a doctor blade. The electrodes were then dried at 100 °C for 12 hr in the vacuum oven. The mass loading of active material ($Na_{1.5}VPO_{4.8}F_{0.7}$ nanoparticles) was around 1 ~ 1.5 mg/cm^2. Swagelok-type electrochemical cells were assembled in an Ar-filled glove box. The cell consisted of sodium metal as a counter electrode, separator (Glass fiber, Advantec), and electrolyte (1M $NaClO_4$ in propylene carbonate (PC) or PC/fluorinated ethylene carbonate (FEC)) For the rate capability test, galvanostatic charge/discharge cycling was performed at rates

ranging from C/10 to 20C with a voltage window of 1.7 – 4.5 V (vs. Na/Na^+). For cycling evaluation, a rate of 1C was used. For cyclic voltammetry, the scan rate 0.1 to 10 mV/s was used within a voltage window of 1.7 – 4.5 V (vs. Na/Na^+).

Chapter 4.4 Results and discussion

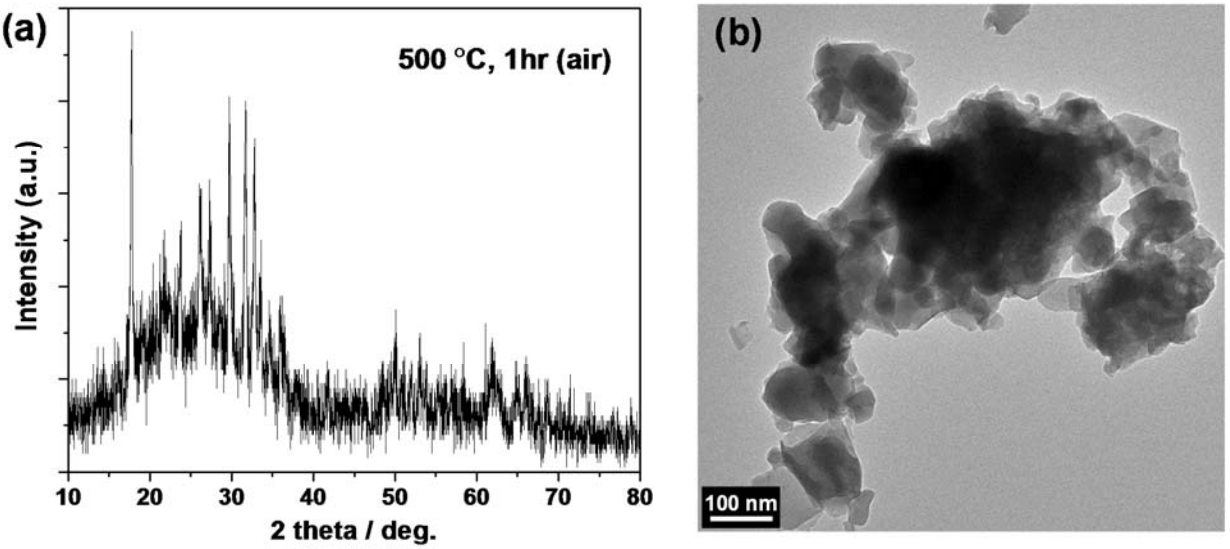

Figure 4.4. (a) XRD pattern and (b) TEM image of precursor mixtures after heat treatment at 500 °C fir 1hr in the air

Structural characterization

In order to synthesize $Na_{1.5}VPO_{4.8}F_{0.7}$ nanoparticles, we introduced a two-step process: (1) modified Pechini method (2) hydrothermal synthesis. We tried several way to synthesis this material with a one step process, however, we could not incorporate fluorine ions into the structure consist of Na, V, and PO_4. First, we used a modified Pechini method[101] to prepare the precursor material. The advantage of this method is that we can prepare small crystalline particles by using citric acid as a chelating agent. During the Pechini synthesis, citric acid and metal ions form a metallic citrate in the water and these metallic citrates are mixed with

phosphate ions which form a mixture of precursors. After drying this solution at 90 °C, the obtained gel-like blue-colored amorphous powder was heat treated at 500 °C for 1hr. A heat-treatment duration of 1 hr was chosen to retain some carbon sources on the particles since these carbon sources are expected to carbonize during the 2nd process all the while maintaining small particle size. XRD patterns in Figure 4.4 (a) show that this powder consists of a mixed crystalline phase containing $NaVO_3$, $VOPO_4$, and V_4O_9 based on JCPDS, but was mainly amorphous. The TEM images in Figure 4.4 (b) show that the particles are aggregated and individual particle size was less than 100 nm. The existence of residual organics or carbon residues are not observed in the TEM images. The heat treatment procedure (500 °C, 1hr) is an important step to synthesize $Na_{1.5}VPO_{4.8}F_{0.7}$ nanoparticles because we need carbon or organics as a capping agent to suppress the growth of particles during the 2nd step. Upon heat treating for more than 2 hours at 500 °C, the carbon sources get oxidized and after the 2nd step, $Na_{1.5}VPO_{4.8}F_{0.7}$ particle sizes are larger than 1 μm. In fact, we were able to prepare micron-sized $Na_{1.5}VPO_{4.8}F_{0.7}$ particles using precursor powder heat treated for 12 hrs at 500 °C.

In the second processing step, fluorine ions were incorporated into the as-prepared precursor powder. For this, we employed a hydrothermal reaction by using sodium fluoride (NaF) as the fluorine source. In addition, during the synthesis we maintained the pH of the solution to alkaline conditions by using 1 equivalent of sodium hydroxide (NaOH) due to the possibility of hydrofluoric acid (HF) formation. After the 2nd processing step, the resulting powder was washed with deionized water for 1 day to remove the sodium carbonate ($NaCO_3$, white color) which is a possible byproduct during the hydrothermal synthesis. The phase of the washed and dried powder was examined by XRD as shown in Figure 4.5. All the reflections were completely indexed with space group $p4_2/mnm$ and no other extra phases were observed.

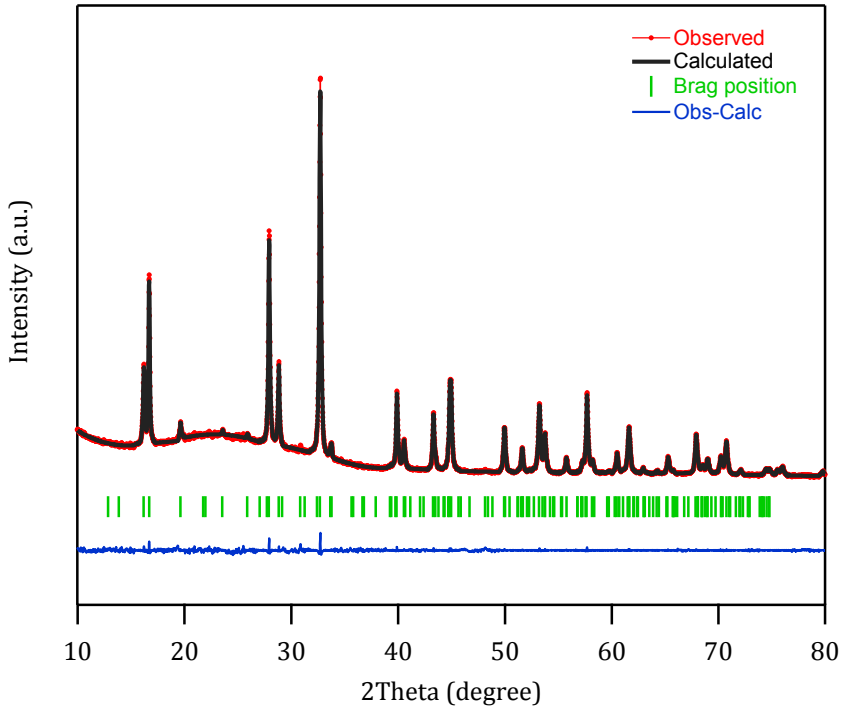

Figure 4.5. XRD pattern and Rietveld refinement of as-synthesized $Na_{1.5}VPO_{4.8}F_{0.7}$ nanoparticles

Symmetry	Tetragonal
Space group	$P4_2/mnm$
Lattice parameters	A=9.030(4) Å, b=9.030(4) Å, c=10.631(6) Å, V=866.99(3) $Å^3$
Rwp (%)	12.9
Rp (%)	10.1
Rbragg (%)	4.3
χ^2	1.02

Table 4.2. XRD powder diffraction and Rietveld refinement results for $Na_{1.5}VPO_{4.8}F_{0.7}$ nanoparticles

The lattice parameters and cell volume of the $Na_{1.5}VPO_{4.8}F_{0.7}$ powder were calculated from the Rietvelt refinement in Table 4.2. These values are in close agreement with the values found in previous studies[4, 89]. This result is interesting because the $Na_{1.5}VPO_{5-x}F_{0.5+x}$ structure can have several different stoichiometries depending on the ratio between oxygen and fluorine. After hydrothermal synthesis, we only observed the structure with the stoichiometry of x=2 ($Na_{1.5}VPO_{4.8}F_{0.7}$). Presumably, this stoichiometry ($Na_{1.5}VPO_{4.8}F_{0.7}$) is the thermodynamically stable phase, so during the long hydrothermal synthesis (5 days), only the $Na_{1.5}VPO_{4.8}F_{0.7}$ phase was formed.

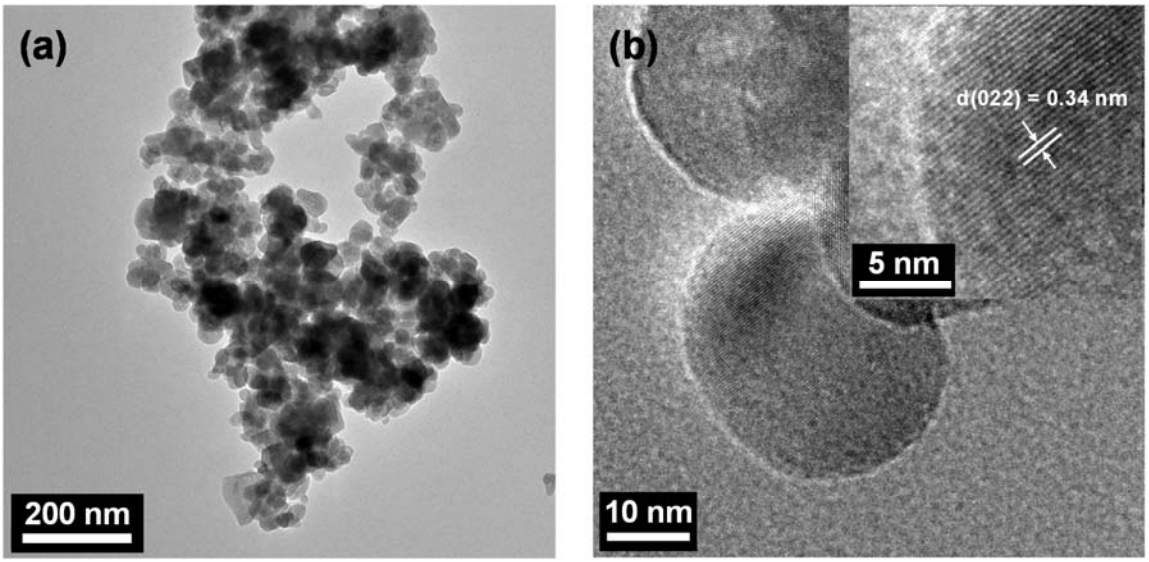

Figure 4.6. (a) TEM and (b) HR-TEM images of as-synthesized $Na_{1.5}VPO_{4.8}F_{0.7}$ nanoparticles (inset shows lattice fringe of (022) and d(022))

The TEM images in Figure 4.6 (a) of the as-synthesized $Na_{1.5}VPO_{4.8}F_{0.7}$ nanoparticles show that their particles sizes are in the range of 20 – 50 nm with irregular shape. In the HR-TEM image, we could observe the (002) plane and the distance between these planes was

approximately 0.34 nm. This value corresponds well with the calculated d(022) value (~ 0.344 nm) from the Rietvled refinement measurements (Table 4.2). Therefore, by using a two-step process, we were able to successfully synthesize pure phase $Na_{1.5}VPO_{4.8}F_{0.7}$ nanoparticles. Next, we began to investigate the electrochemical properties of $Na_{1.5}VPO_{4.8}F_{0.7}$ nanoparticles. As known from the previous report, the family of $Na_{1.5}VPO_{5-x}F_{0.5+x}$ compositions is electrically insulating. In order to overcome this problem, carbon coating on the family of $Na_{1.5}VPO_{5-x}F_{0.5+x}$ materials has generally been used to increase this material's electrical conductivity[85, 89]. Thus, $Na_{1.5}VPO_{4.8}F_{0.7}$ nanoparticles were carbon coated with super P carbon black using HEBM in this study. After HEBM, additional heat treatment was done to increase the contact between $Na_{1.5}VPO_{4.8}F_{0.7}$ nanoparticles and also recover the loss in crystallinity. In this treatment, the ball-milled, carbon-coated $Na_{1.5}VPO_{4.8}F_{0.7}$ nanoparticles were heat treated at 450 °C under argon for 2hr.

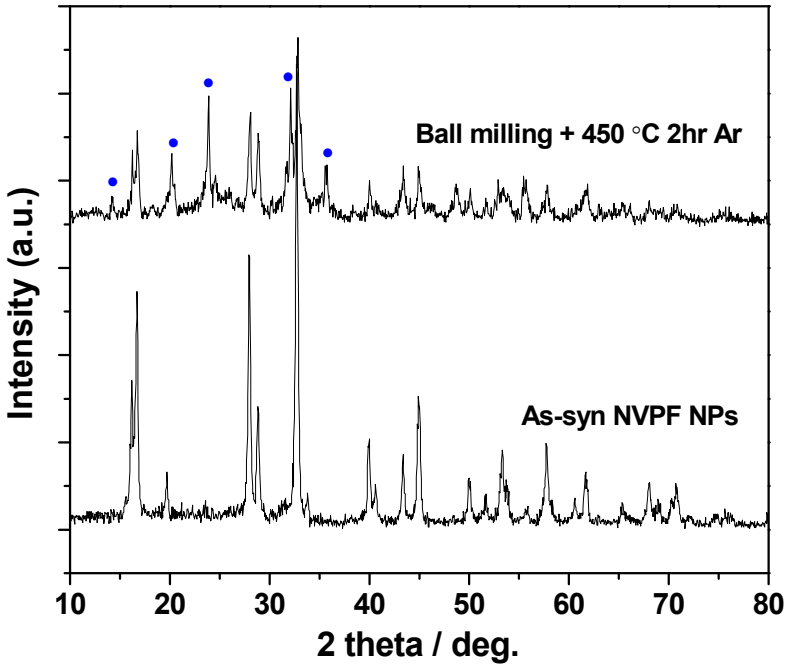

Figure 4.7. XRD patterns of as-synthesized $Na_{1.5}VPO_{4.8}F_{0.7}$ nanoparticles and after ball milling and heat treatment 450 °C for 2hr in Argon atmosphere

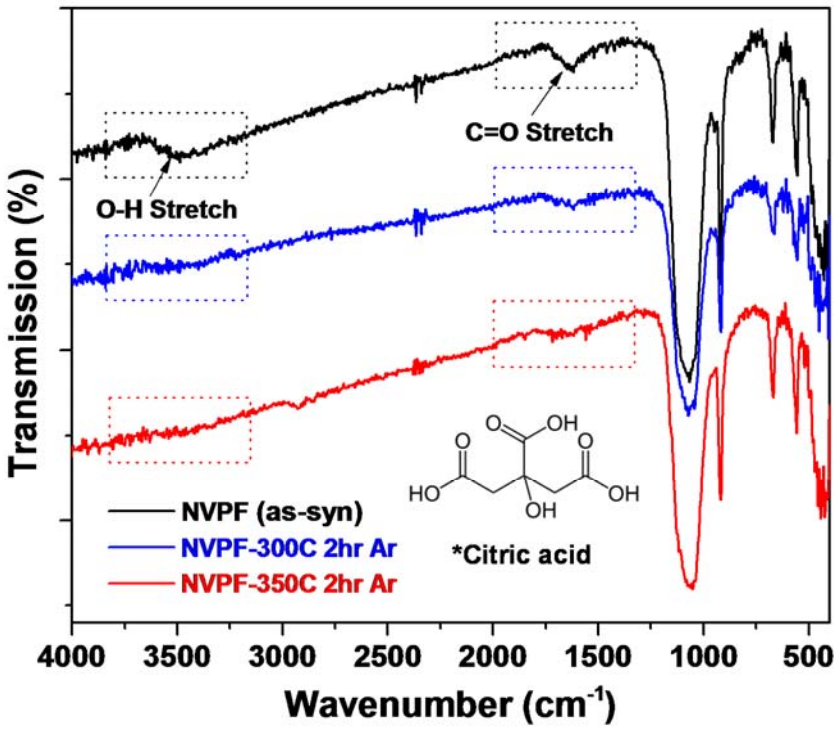

Figure 4.8. FT-IR spectra of as-synthesized $Na_{1.5}VPO_{4.8}F_{0.7}$ nanoparticles and after heat treatment at 300 °C and 350 °C for 2hr in argon atmosphere

The problem of additional heat treatment

In order to determine the phase after heat treatment at 450 °C in argon, we took XRD as shown in Figure 4.7. The XRD pattern indicates the presence of a new phase after heat treatment. We observed several new peaks which may be from the oxidized species (e.g. V_2O_5, V_2O_3) of vanadium ions in $Na_{1.5}VPO_{4.8}F_{0.7}$ nanoparticles. Although the heat treatment was performed in an argon atmosphere, the oxidation problem means that there are oxygen sources in the $Na_{1.5}VPO_{4.8}F_{0.7}$ nanoparticles. The most probable explanation for this is that the oxygen sources may be coming from the organic residues. These organic residues are beneficial to suppress particle growth during hydrothermal synthesis, however, these residues can also act as oxygen

sources that work to oxidize vanadium during heat treatment especially in nanosized $Na_{1.5}VPO_{4.8}F_{0.7}$. In order to prevent this oxidation problem, we tried to remove the organic residues by heat treatment at lower temperatures (300 °C and 350 °C under argon). Figure 4.8 shows the FT-IR spectrum before and after heat treatment at these temperatures. The C=O stretch vibration around 3500 cm^{-1} and O-H stretch vibration around 1600 cm^{-1} were clearly observed in as-synthesized $Na_{1.5}VPO_{4.8}F_{0.7}$ nanoparticles and these spectra mainly came from the carboxylic and hydroxyl functional group of citric acid. (Inset of Figure 4.8). After heat treatment, the signals coming from the carboxylic and hydroxyl functional groups decreased and heat treatment of $Na_{1.5}VPO_{4.8}F_{0.7}$ nanoparticles at 350 °C resulted in near removal of the residues.

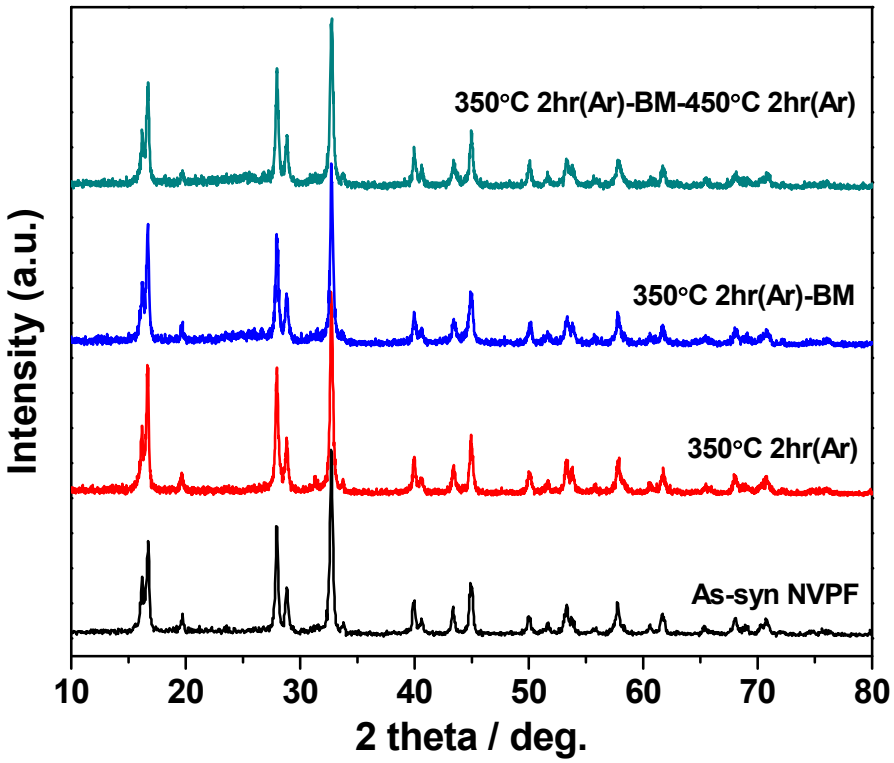

Figure 4.9. XRD patterns of as-synthesized $Na_{1.5}VPO_{4.8}F_{0.7}$ nanoparticles, after each sample preparation step. (pre-heat treatment → ball milling → heat treatment)

We confirmed the removal of organic residues by pre-heat treatment. In the corresponding XRD patterns, no other phases were present during the processes. The $Na_{1.5}VPO_{4.8}F_{0.7}$ nanoparticles and carbon (super P) were well mixed after the last heat treatment (450 °C for 2hr in Argon) as shown in the TEM image found in Figure 4.10.

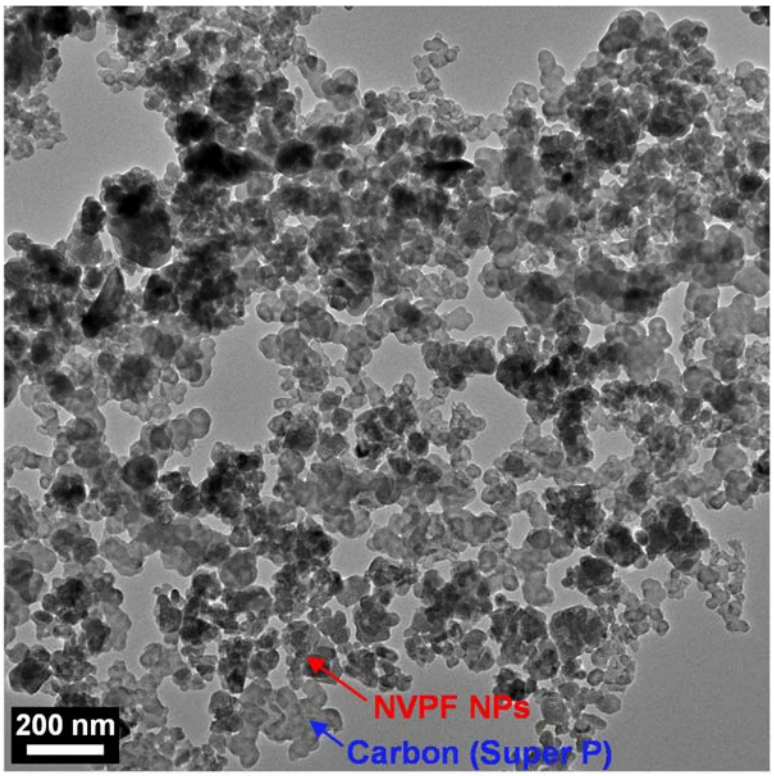

Figure 4.10. TEM image of $Na_{1.5}VPO_{4.8}F_{0.7}$ nanoparticles and carbon after all processes

The amount of organic residue removed during the heat treatment was monitored by TGA (Figure 4.11 (a)) and a considerable amount of residual organics (about 5 ~ 6 %) was removed. Finally, we prepared the electrodes with pure phase $Na_{1.5}VPO_{4.8}F_{0.7}$ nanoparticles (Figure 4.9) and the carbon amount was measured as ~ 24 % (active materials ~ 76 %) by TGA as shown in Figure 4.11 (b).

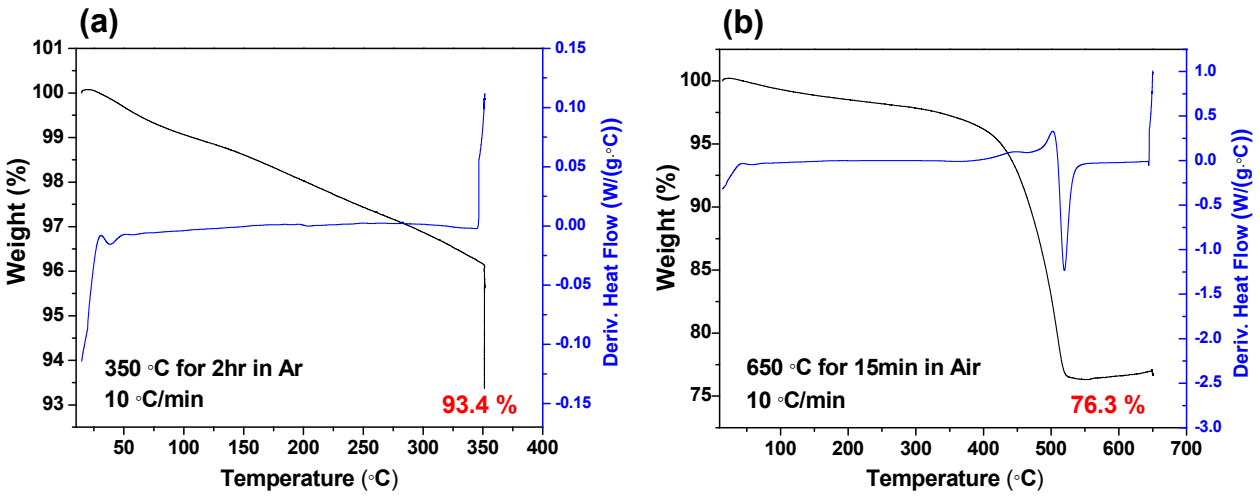

Figure 4.11 (a) TGA on as synthesized $Na_{1.5}VPO_{4.8}F_{0.7}$ nanoparticles during pre-heat treatment (b) TGA on $Na_{1.5}VPO_{4.8}F_{0.7}$ nanoparticles after the final heat treatment

Electrochemical characterization

In order to investigate the electrochemical performance of $Na_{1.5}VPO_{4.8}F_{0.7}$ nanoparticles, we prepared thick electrodes using the doctor blade technique where the carbon slurry containing $Na_{1.5}VPO_{4.8}F_{0.7}$ nanoparticles was coated uniformly onto carbon-coated aluminum foil. The electrodes were formed with 3/8 inch diameter punch. The active material loading was on the order of 1 - 1.5 mg/cm^2. Figure 4.12 (a) shows the galvanostatic charge/discharge profile at C/10 in 1M $LiClO_4$ in PC electrolyte. We can clearly observe two plateaus and each plateau is related to 0.5 mol sodium ion insertion/deinsertion at different sites in the $Na_{1.5}VPO_{4.8}F_{0.7}$ structure[89, 102]. Serras et al. investigated the structural evolution of $Na_{1.5}VPO_{4.8}F_{0.7}$ with sodium ions using *in situ* XRD measurement and showed that the low voltage plateau (at 3.6 V vs. Na/Na^+) is related to a phase transition and high voltage plateau (at 4.0 V vs. Na/Na^+)) is related to the solid-solution behavior[102]. The large capacity during the first charge is related to the oxidative decomposition of electrolyte and corresponding solid electrolyte interface (SEI) layer formation

on the $Na_{1.5}VPO_{4.8}F_{0.7}$ nanoparticles. From the second cycle, the coulombic efficiency is improved, however it still shows low coulombic efficiency (85 %) after the 5th cycle.

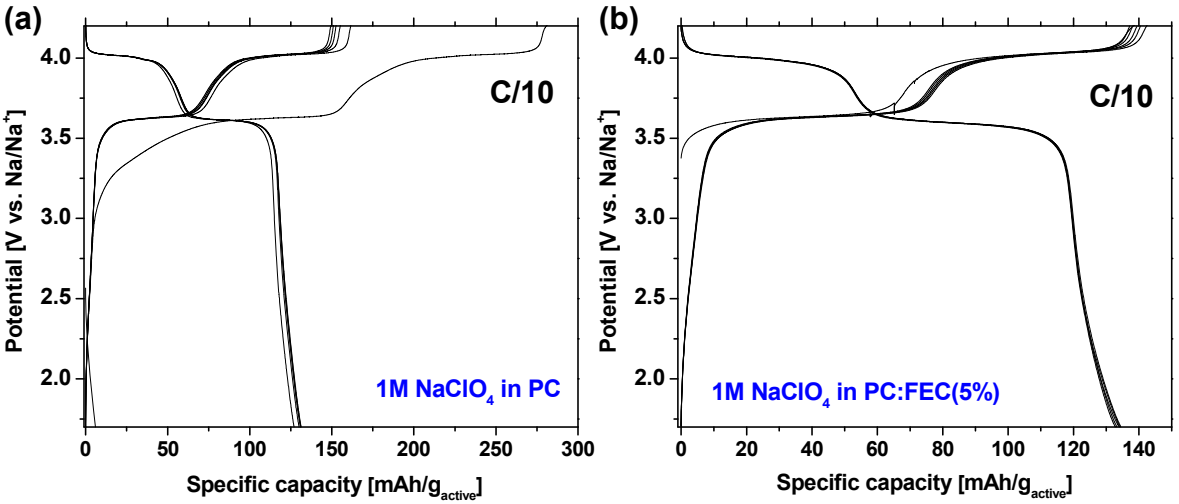

Figure 4.12. Galvanostatic charge/discharge profile of $Na_{1.5}VPO_{4.8}F_{0.7}$ nanoparticles in (a) 1M $NaClO_4$ in PC and (b) 1M $NaClO_4$ in PC:FEC (5%)

There have been several reports on electrolyte additives which can improve the columbic efficiency and cycle life of electrodes for sodium ion batteries[98, 99, 103]. One of the important electrolyte additives is fluoroethylene carbonate (FEC) which has mainly been used for sodium ion battery anodes such as hard carbon. The 5% addition into the polycarbonate electrolyte showed a drastic improvement in both columbic efficiency and the cyclability of a hard carbon electrode[100, 104]. In addition, FEC can also improve the coulombic efficiency of the positive electrode[100]. We compared the first 5 cycles of galvanostatic charge/discharge profiles between the cells using the electrolyte with and without FEC as an additive (5%). Figure 4.12 (b) shows the 5 cycles at C/10 in the cell with FEC in 1M $LiClO_4$ in PC and this clearly shows the positive effect of FEC since there is an increase in the columbic efficiency compared to the cell without

FEC (Figure 4.12 (a)). The large charge capacity due to the electrolyte decomposition observed in the previous electrolyte system (without FEC) totally disappeared in the electrolyte with FEC. In addition, after the 5th cycle, a coulombic efficiency of 98 % with FEC was observed and this is quite an improvement compared to a low columbic efficiency of 87 % without FEC. This result suggests that the addition of FEC helps to form a stable SEI layer with minimal oxidative decomposition of the PC solvent at high potentials. As a result, the rest of the electrochemical characterization was performed using the 1M $LiClO_4$ in PC/FEC (5%) electrolyte.

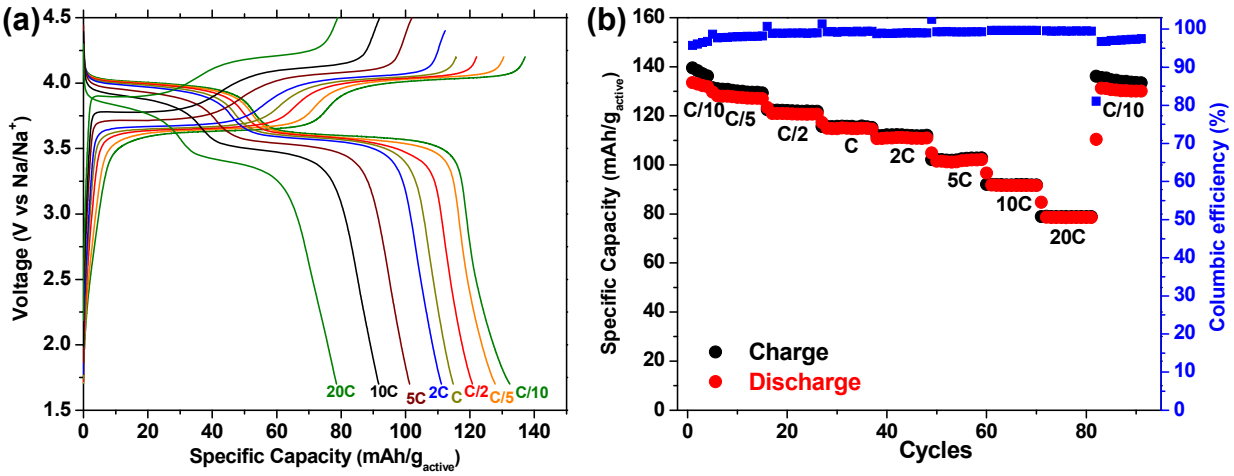

Figure 4.13. (a) Galvanostatic charge/discharge profile of $Na_{1.5}VPO_{4.8}F_{0.7}$ nanoparticles at different C-rate (C/10 ~ 20C) (b) Specific capacity and coulombic efficiency of $Na_{1.5}VPO_{4.8}F_{0.7}$ nanoparticles depending on the C-rates

In order to investigate the rate capability, $Na_{1.5}VPO_{4.8}F_{0.7}$ nanoparticle electrodes were cycled galvanostatically between C/10 and 20 C rate (Figure 4.13) At C/10, the $Na_{1.5}VPO_{4.8}F_{0.7}$ nanoparticle electrode achieved its theoretical capacity of 130 mAh/g which corresponds to a one electron process of the vanadium redox couple ($V^{4+} \leftrightarrow V^{5+}$). It is noteworthy that at a rate of 20 C, which corresponds to a 3 minute charge or discharge, the discharge capacity was about 80

mAh/g and this value is comparable to that of the state of the art sodium ion battery cathode material[105, 106, 107, 108]. Also the rate capability of this material is competitive even with the cathode materials studied for lithium ion batteries. This high rate capability of $Na_{1.5}VPO_{4.8}F_{0.7}$ nanoparticles may be from the suppression of a phase transition. As mentioned earlier, micron-sized bulk $Na_{1.5}VPO_{4.8}F_{0.7}$ undergoes a phase transition at the low voltage plateau (~ 3.6 V vs. Na/Na^+). This phase transition is generally a slow process and suppressing this phase transition is one possible explanation for the observed high rate capability. Another advantage of this material is the relatively high potential where the voltage plateaus exists at 3.6 and 4.0 V vs. Na/Na^+ as shown in the galvanostatic charge/discharge profile (Figure 4.13 (a)). High potential leads to high energy density and this characteristic for $Na_{1.5}VPO_{4.8}F_{0.7}$ stems from the high electronegativity of the fluorine ions, which consequently increases the redox potential of vanadium[4]. The high voltage characteristic as well as high capacity at high rate for $Na_{1.5}VPO_{4.8}F_{0.7}$ nanoparticles make this material a fascinating candidate cathode material for sodium ion batteries. Figure 4.13 (b) shows the specific capacities and coulombic efficiency of 10 cycles at each C-rate. The capacity of $Na_{1.5}VPO_{4.8}F_{0.7}$ nanoparticles was stable at each C-rate and the coulombic efficiency was around 97% at C/10 and higher than 99 % at faster rates. Moreover, when the material is cycled back to C/10 after 20 C (total 90 cycles), the initial capacity of ~130 mAh/g at C/10 is recovered and further supports the good cyclability of the $Na_{1.5}VPO_{4.8}F_{0.7}$ nanoparticles. Figure 4.14 (a) shows the cyclability test of $Na_{1.5}VPO_{4.8}F_{0.7}$ nanoparticles at 1C. A discharge capacity of 123 mAh/g and a coulombic efficiency of 97 % were observed upon the first cycle and after 10 cycles, coulombic efficiency kept increasing until reaching 99 %. This again shows the very stable SEI layer formation with the addition of FEC.

After 100 cycles, 93 % of the initial capacity was maintained (115 mAh/g at 100th cycle) and this proves the superior cycling performance of $Na_{1.5}VPO_{4.8}F_{0.7}$ nanoparticles.

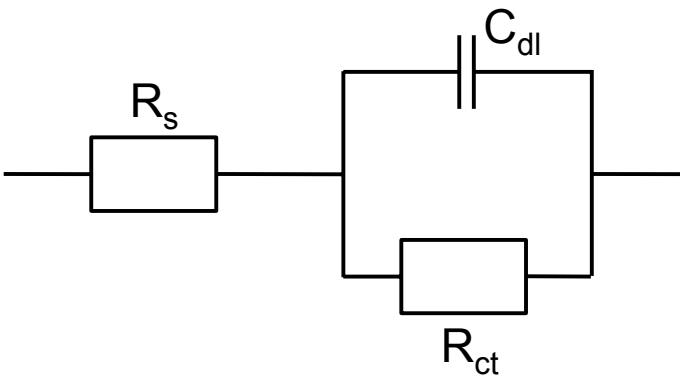

Figure 4.14. Simplified Randles cell schematic diagram

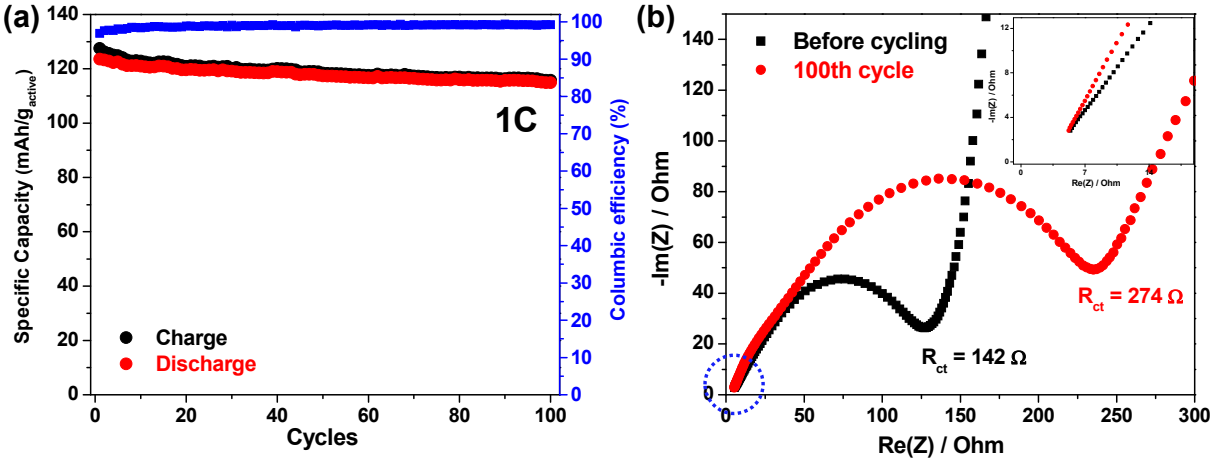

Figure 4.15. (a) Cyclability test of $Na_{1.5}VPO_{4.8}F_{0.7}$ nanoparticles at 1C (b) Impedance measurement before and after 100 cycles at 1C

Impedance spectroscopy was performed to investigate the behavior of $Na_{1.5}VPO_{4.8}F_{0.7}$ nanoparticles before and after cycling. The equivalent circuit for the simplified Randles Cell is shown in Figure 4.14. Figure 4.15 shows that the initial charge transfer resistance (R_{ct}) of 142 Ω

increased to 274 Ω at cycle 100, which is mainly due to SEI formation. More importantly, the solution resistance of 5.5 Ω at the first cycle was unchanged after 100 cycles and this shows that the electrolyte containing FEC is very stable.

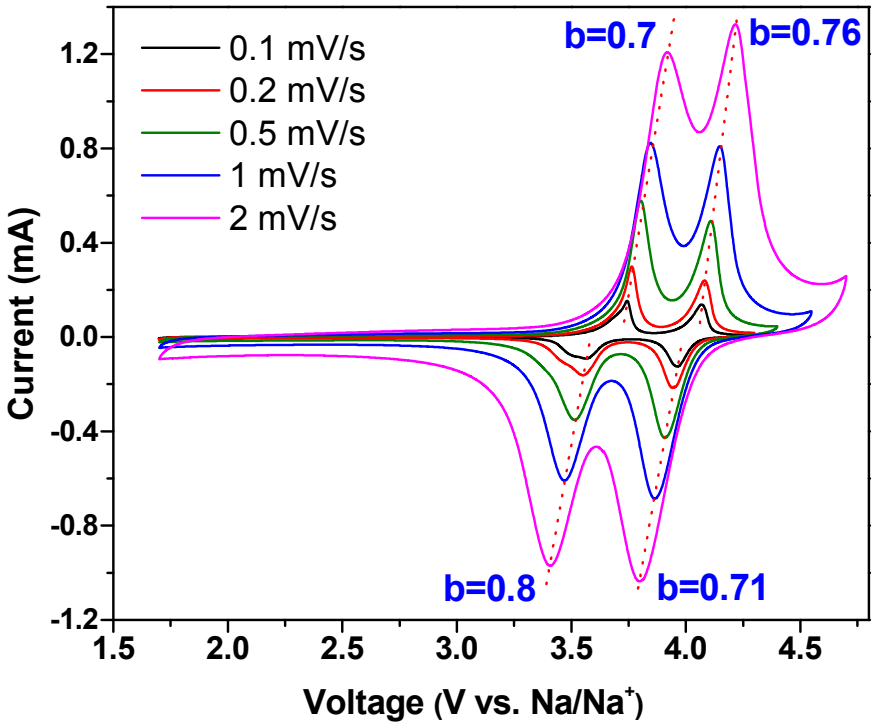

Figure 4.16. Cyclic voltammetry of $Na_{1.5}VPO_{4.8}F_{0.7}$ nanoparticles from 0.1 to 2 mV/s

Cyclic voltammetry experiments were used to investigate the kinetic behavior of $Na_{1.5}VPO_{4.8}F_{0.7}$ nanoparticles. The sweep rates varied between 0.1 to 2 mV/s(Figure 4.16) and the potentials ranged between 4.7 and 1.7V vs Na/Na^+. In the cyclic voltammogram, we could observe two well defined peaks during charge and discharge and this corresponds to the two voltage plateaus in galvanostatic cycling. The b-values were calculated at the peak potentials from the CV and the results are shown in Figure 4.16. (Method is explained in the Chapter 2.4.) The calculated b-values were 0.71 (at 4.0 V) and 0.8 (at 3.6 V) during discharge and 0.76 (at 4.0

V) and 0.7 (at 3.6 V) during charge (Figure 4.16). For typical battery materials, a b-value at the peak potential is around 0.5 because charge storage is limited by solid-state diffusion of ions. Thus, these b-values in $Na_{1.5}VPO_{4.8}F_{0.7}$ nanoparticles demonstrate that there are some capacitive contributions to charge storage and this is why $Na_{1.5}VPO_{4.8}F_{0.7}$ nanoparticles show fast rate capability. (Figure 4.13 (b)) In order to calculate the chemical diffusion coefficient of lithium ions into the $Na_{1.5}VPO_{4.8}F_{0.7}$ nanoparticles, we used the following equation[67].

$$i_p = 0.4958nFAC(D\alpha n\nu F/RT)^{0.5} \qquad \text{eq 4.1}$$

This equation is valid only for diffusion limited irreversible system and to apply this equation we need to calculate the diffusion controlled current contribution from the total current. The measured total current at the specific potential is a summation of two components which are the diffusion controlled current and the capacitive current as shown in Equation 4.2. This is derived from the power law relationship where k_1v is the capacitive current and $k_2v^{0.5}$ is the diffusion-controlled current.

$$i(V) = k_1 \nu + k_2 \nu^{0.5} \qquad \text{eq 4.2}$$

By plotting $i(V)/v$ vs. $1/v^{0.5}$, we can derive k_2 values and determine the diffusion controlled current. Using these current values we were able to calculate the chemical diffusion coefficients at the peak potentials for both the anodic and cathodic sweep. Calculated chemical diffusion coefficients are shown in Table 4.3. The values of around 10^{-12} cm^2/s were calculated and when

we consider the electrode architecture (thick electrode) and the size of the ions (sodium ions), these values are quite high for sodium ion battery systems.

Voltage	b-values	Diffusion coefficient (cm^2/s)
Cathodic at 4.0 V	**0.71**	**1.89×10^{-12}**
Cathodic at 3.6 V	**0.8**	**2.46×10^{-12}**
Anodic at 4.0 V	**0.76**	**5.83×10^{-12}**
Anodic at 3.6 V	**0.7**	**8.54×10^{-12}**

Table 4.3. Calculated b-values and chemical diffusion coefficients at peak potentials

4.5. Conclusion

The present work showed the synthesis and electrochemistry of $Na_{1.5}VPO_{4.8}F_{0.7}$ nanoparticles. In order to synthesize $Na_{1.5}VPO_{4.8}F_{0.7}$ nanoparticles, a two-step process was used. During the electrode preparation process, we introduced pre-heat treatment to solve the oxidation problem of vanadium and by doing so, we were able to synthesize pure phase $Na_{1.5}VPO_{4.8}F_{0.7}$ nanoparticles. For the electrochemistry measurements, we used FEC as an electrolyte additive since the coulombic efficiency was 87 % without FEC and the addition of FEC helped to increase the coulombic efficiency to 97 % after the 5^{th} cycle at a charging rate of C/10. $Na_{1.5}VPO_{4.8}F_{0.7}$ nanoparticles showed high capacity, fast rate capability and superior cyclability. At C/10, $Na_{1.5}VPO_{4.8}F_{0.7}$ nanoparticles achieved a capacity of 134 mAh/g which is higher than the theoretical capacity. The capacity of 79 mAh/g at 20C shows the high rate capability of this material. Also, the cycling behavior indicated very good stability of the electrode and electrolyte. 93 % of the initial capacity was maintained after 100 cycles and the electrolyte resistance did not

increase at all after cycling due to the positive effect of FEC. The nanostructuring of $Na_{1.5}VPO_{4.8}F_{0.7}$ helped to achieve fast kinetics and with the help of FEC, we were able to improve the coulombic efficiency of this material. With the good performance shown in this study, $Na_{1.5}VPO_{4.8}F_{0.7}$ nanoparticles are a promising candidate for use as a cathode for sodium ions batteries.

4.6. Suggestions for future work.

For the future work, I will prepare full cells using Sb as an anode. Some of the other members in my group are working on the anode materials for sodium ion batteries and they have shown that Sb has a high capacity and fast kinetics in half cell testing. Thus, it will be interesting to see how the full cell composed of a $Na_{1.5}VPO_{4.8}F_{0.7}$ nanoparticle cathode and Sb anode performs. In addition to this, I will investigate the structural behavior of $Na_{1.5}VPO_{4.8}F_{0.7}$ nanoparticles. As mentioned in chapter 4.4, $Na_{1.5}VPO_{4.8}F_{0.7}$ undergoes a phase transition at the low-voltage plateau (~ 3.6 V vs. Na/Na^+). However, in some nanostructured battery materials, phase transitions can be suppressed and this results in fast kinetics. It will be interesting to establish whether or not the high rate capability of $Na_{1.5}VPO_{4.8}F_{0.7}$ nanoparticles is coming from the suppression of the low-voltage phase transition. In these experiments, I will perform *ex situ* XRD with $Na_{1.5}VPO_{4.8}F_{0.7}$ nanoparticles.

Chapter 5. Conclusion

Previous studies of mesoporous α-MoO_3 and T-Nb_2O_5 showed promising results for high energy and power density energy storage applications by utilizing the intercalation pseudocapacitance mechanism. For the first two parts of this dissertation, we developed materials that display pseudocapactive properties in α-MoO_3 and MoO_2, which are both well-known battery materials. The reason why we chose the α-MoO_3 system is that it has a high theoretical capacity (~ 300 mAh/g) with lithium ions. Intrinsic constraints of α-MoO_3 such as low electrical conductivity and irreversible phase transitions have limited the applications of α-MoO and by introducing oxygen vacancies, we were able to resolve these limitations. Reduced MoO_{3-x} features fast kinetics (~ 57 % of theoretical capacity in 20 seconds of discharging) with higher capacity than fully oxidized MoO_3. Also, reduced MoO_{3-x} showed better cycling performance than fully-oxidized MoO_3. These outstanding electrochemical characteristics come from the vdWs gap expansion, high electrical conductivity, irreversible lithium insertion/deinsertion without phase transformation, and greater number of Mo^{4+} oxidation states. This research on reduced α-MoO_3 opens up new prospective for oxygen-deficient transition metal oxides. This can be an interesting direction for developing known battery materials and exploiting improved performances just by tailoring defects such as oxygen vacancies.

The second material system we investigated was monoclinic MoO_2. The motivation was that MoO_2 has high theoretical capacity (~ 840 mAh/g) with metallic electrical conductivity. The slow kinetics of MoO_2 are due to a phase transition and micron-sized particles limit the application of this material. In this study, we synthesized nanosized (~ 15 nm) MoO_2 particles and this nanosized-MoO_2 could suppress the corresponding phase transition during the lithium insertion/deinsertion process. The problem of surface oxidation in nanosized-MoO_2 was solved

by incorporating reduced graphene oxide as a conductive medium. Electrochemical measurements indicated that MoO_2-RGO exhibited fast kinetics (~ 84 % was capacitive charge storage at 1 mV/s) with high capacity (~ 200 mAh/g). In order to evaluate the applicability to real devices, thick electrodes were prepared and tested. MoO_2-RGO thick electrodes showed 150 mAh/g at 50 C with good cyclability. Thus the MoO_2-RGO system can be a promising candidate electrode material for pseudocapacitive energy storage applications.

The last part of this dissertation focused on developing high rate sodium ion battery materials. Sodium ions batteries have been attracting a lot of attention for energy storage systems because of the abundance of sodium sources. The larger ion size and lower standard electrochemical potential limit the development of sodium ion batteries. In order to overcome these limitations, we chose the sodium vanadium fluorophosphate system ($Na_{1.5}VPO_{4.8}F_{0.7}$) because this material has a high operating potential (~ 3.8 V) which translates to high energy density. For this project, we synthesized nanosized (~ 30 nm) $Na_{1.5}VPO_{4.8}F_{0.7}$ to achieve fast kinetics. $Na_{1.5}VPO_{4.8}F_{0.7}$ nanoparticles showed high rate capability (~ 80 mAh/g at 20C) with good cycling performance (~ 93 % capacity retention after 100 cycles at 1C). Excellent columbic efficiency (~ 99 %) was achieved by adding fluorinated ethylene carbonate (FEC) into electrolyte. We are currently planning to prepare the full cell using antimony (Sb) anode.

References

1. Simon P, Gogotsi Y. Materials for electrochemical capacitors. *Nature Mater* 2008, **7**(11)**:** 845-854.

2. Yabuuchi N, Kubota K, Dahbi M, Komaba S. Research Development on Sodium-Ion Batteries. *Chem Rev* 2014, **114**(23)**:** 11636-11682.

3. Larcher D, Tarascon JM. Towards greener and more sustainable batteries for electrical energy storage. *Nature Chem* 2015, **7**(1)**:** 19-29.

4. Park YU, Seo DH, Kim B, Hong KP, Kim H, Lee S*, et al.* Tailoring a fluorophosphate as a novel 4 V cathode for lithium-ion batteries. *Sci Rep-Uk* 2012, **2**.

5. Stevenson KJ, Ozolins V, Dunn B. Electrochemical Energy Storage. *Acc Chem Res* 2013, **46**(5)**:** 1051-1052.

6. Miller JR, Simon P. Electrochemical Capacitors for Energy Management. *Science* 2008, **321**(5889)**:** 651-652.

7. Simon P, Gogotsi Y, Dunn B. Where Do Batteries End and Supercapacitors Begin? *Science* 2014, **343**(6176)**:** 1210-1211.

8. Brousse T, Belanger D, Long JW. To Be or Not To Be Pseudocapacitive? *J Electrochem Soc* 2015, **162**(5)**:** A5185-A5189.

9. Zheng JP, Cygan PJ, Jow TR. Hydrous Ruthenium Oxide as an Electrode Material for Electrochemical Capacitors. *J Electrochem Soc* 1995, **142**(8)**:** 2699-2703.

10. Brousse T, Toupin M, Dugas R, Athouel L, Crosnier O, Belanger D. Crystalline MnO2 as possible alternatives to amorphous compounds in electrochemical supercapacitors. *J Electrochem Soc* 2006, **153**(12)**:** A2171-A2180.

11. Brezesinski T, Wang J, Tolbert SH, Dunn B. Ordered mesoporous alpha-MoO3 with iso-oriented nanocrystalline walls for thin-film pseudocapacitors. *Nature Mater* 2010, **9**(2)**:** 146-151.

12. Kim JW, Augustyn V, Dunn B. The Effect of Crystallinity on the Rapid Pseudocapacitive Response of Nb2O5. *Adv Energy Mater* 2012, **2**(1)**:** 141-148.

13. Augustyn V, Simon P, Dunn B. Pseudocapacitive oxide materials for high-rate electrochemical energy storage. *Energy Environ Sci* 2014, **7**(5)**:** 1597-1614.

14. Come J, Augustyn V, Kim JW, Rozier P, Taberna PL, Gogotsi P*, et al.* Electrochemical Kinetics of Nanostructured Nb2O5 Electrodes. *J Electrochem Soc* 2014, **161**(5)**:** A718-A725.

15. Sadakane M, Watanabe N, Katou T, Nodasaka Y, Ueda W. Crystalline Mo3VOx mixed-metal-oxide catalyst with trigonal symmetry. *Angew Chem Int Ed* 2007, **46**(9)**:** 1493-1496.

16. Zheng L, Xu Y, Jin D, Xie Y. Novel Metastable Hexagonal MoO3 Nanobelts: Synthesis, Photochromic, and Electrochromic Properties. *Chem Mater* 2009, **21**(23)**:** 5681-5690.

17. Comini E, Yubao L, Brando Y, Sberveglieri G. Gas sensing properties of MoO3 nanorods to CO and CH3OH. *Chem Phys Lett* 2005, **407**(4-6)**:** 368-371.

18. Lee SH, Kim YH, Deshpande R, Parilla PA, Whitney E, Gillaspie DT*, et al.* Reversible Lithium-Ion Insertion in Molybdenum Oxide Nanoparticles. *Adv Mater* 2008, **20**(19)**:** 3627-+.

19. Zheng L, Xu Y, Jin D, Xie Y. Well-aligned molybdenum oxide nanorods on metal substrates: solution-based synthesis and their electrochemical capacitor application. *J Mater Chem* 2010, **20**(34)**:** 7135-7143.

20. Chernova NA, Roppolo M, Dillon AC, Whittingham MS. Layered vanadium and molybdenum oxides: batteries and electrochromics. *J Mater Chem* 2009, **19**(17)**:** 2526-2552.

21. Li W, Cheng F, Tao Z, Chen J. Vapor-Transportation Preparation and Reversible Lithium Intercalation/Deintercalation of α-MoO3 Microrods. *J Phys Chem B* 2005, **110**(1)**:** 119-124.

22. Tsumura T, Inagaki M. Lithium insertion/extraction reaction on crystalline MoO3. *Solid State Ionics* 1997, **104**(3–4)**:** 183-189.

23. Zhou L, Yang L, Yuan P, Zou J, Wu Y, Yu C. α-MoO3 Nanobelts: A High Performance Cathode Material for Lithium Ion Batteries. *J Phys Chem C* 2010, **114**(49)**:** 21868-21872.

24. Kang JH, Paek SM, Choy JH. In Situ X-ray Absorption Spectroscopic Study for alpha-MoO3 Electrode upon Discharge/Charge Reaction in Lithium Secondary Batteries. *Bull Korean Chem Soc* 2010, **31**(12)**:** 3675-3678.

25. Mai LQ, Hu B, Chen W, Qi YY, Lao CS, Yang RS*, et al.* Lithiated MoO3 Nanobelts with Greatly Improved Performance for Lithium Batteries. *Adv Mater* 2007, **19**(21)**:** 3712-3716.

26. Wang X-J, Nesper R, Villevieille C, Novák P. Ammonolyzed MoO3 Nanobelts as Novel Cathode Material of Rechargeable Li-Ion Batteries. *Adv Energy Mater* 2013, **3**(5)**:** 606-614.

27. Balendhran S, Deng JK, Ou JZ, Walia S, Scott J, Tang JS*, et al.* Enhanced Charge Carrier Mobility in Two-Dimensional High Dielectric Molybdenum Oxide. *Adv Mater* 2013, **25**(1)**:** 109-114.

28. Hu XK, Qian YT, Song ZT, Huang JR, Cao R, Xiao JQ. Comparative Study on MoO3 and HxMoO3 Nanobelts: Structure and Electric Transport. *Chem Mater* 2008, **20**(4)**:** 1527-1533.

29. Dieterle M, Weinberg G, Mestl G. Raman spectroscopy of molybdenum oxides Part I. Structural characterization of oxygen defects in MoO3-x by DR UV/VIS, Raman spectroscopy and X-ray diffraction. *Physical Chemistry Chemical Physics* 2002, **4**(5)**:** 812-821.

30. Wang G, Ling Y, Li Y. Oxygen-deficient metal oxide nanostructures for photoelectrochemical water oxidation and other applications. *Nanoscale* 2012, **4**(21)**:** 6682-6691.

31. Lu X, Wang G, Zhai T, Yu M, Gan J, Tong Y*, et al.* Hydrogenated TiO2 Nanotube Arrays for Supercapacitors. *Nano Lett* 2012, **12**(3)**:** 1690-1696.

32. Shin J-Y, Joo JH, Samuelis D, Maier J. Oxygen-Deficient TiO2−δ Nanoparticles via Hydrogen Reduction for High Rate Capability Lithium Batteries. *Chem Mater* 2011, **24**(3)**:** 543-551.

33. Nazri G, Thackeray M, Ohzuku T, Electrochemical Society. Battery Division., Electrochemical Society. Energy Technology Division. *Intercalation compounds for battery materials : proceedings of the international symposium*. Electrochemical Society: Pennington, NJ, 2000.

34. Xu L, Ding Y-S, Chen C-H, Zhao L, Rimkus C, Joesten R*, et al.* 3D Flowerlike α-Nickel Hydroxide with Enhanced Electrochemical Activity Synthesized by Microwave-Assisted Hydrothermal Method. *Chem Mater* 2007, **20**(1)**:** 308-316.

35. Murugan AV, Muraliganth T, Manthiram A. Comparison of Microwave Assisted Solvothermal and Hydrothermal Syntheses of LiFePO4/C Nanocomposite Cathodes for Lithium Ion Batteries. *J Phys Chem C* 2008, **112**(37)**:** 14665-14671.

36. Cook JB, Kim C, Xu L, Cabana J. The Effect of Al Substitution on the Chemical and Electrochemical Phase Stability of Orthorhombic LiMnO2. *J Electrochem Soc* 2013, **160**(1)**:** A46-A52.

37. Lou XW, Zeng HC. Hydrothermal synthesis of alpha-MoO3 nanorods via acidification of ammonium heptamolybdate tetrahydrate (vol 14, pg 4781, 2002). *Chem Mater* 2002, **14**(11)**:** 4880-4880.

38. Lindström H, Södergren S, Solbrand A, Rensmo H, Hjelm J, Hagfeldt A*, et al.* Li+ Ion Insertion in TiO2 (Anatase). 2. Voltammetry on Nanoporous Films. *J Phys Chem B* 1997, **101**(39)**:** 7717-7722.

39. Wang J, Polleux J, Lim J, Dunn B. Pseudocapacitive Contributions to Electrochemical Energy Storage in TiO2 (Anatase) Nanoparticles. *J Phys Chem C* 2007, **111**(40)**:** 14925-14931.

40. Augustyn V, Come J, Lowe MA, Kim JW, Taberna P-L, Tolbert SH*, et al.* High-rate electrochemical energy storage through Li+ intercalation pseudocapacitance. *Nature Mater* 2013, **12**(6)**:** 518-522.

41. Bard AJ, Faulkner LR. *Electrochemical methods : fundamentals and applications*, 2nd edn. Wiley: New York, 2001.

42. Iriyama Y, Abe T, Inaba M, Ogumi Z. Transmission electron microscopy (TEM) analysis of two-phase reaction in electrochemical lithium insertion within alpha-MoO3. *Solid State Ionics* 2000, **135**(1-4)**:** 95-100.

43. Conway BE, Birss V, Wojtowicz J. The role and utilization of pseudocapacitance for energy storage by supercapacitors. *J Power Sources* 1997, **66**(1-2)**:** 1-14.

44. Augustyn V, Come J, Lowe MA, Kim JW, Taberna PL, Tolbert SH*, et al.* High-rate electrochemical energy storage through Li+ intercalation pseudocapacitance. *Nature Mater* 2013, **12**(6)**:** 518-522.

45. Balke N, Jesse S, Morozovska AN, Eliseev E, Chung DW, Kim Y*, et al.* Nanoscale mapping of ion diffusion in a lithium-ion battery cathode. *Nature Nanotech* 2010, **5**(10)**:** 749-754.

46. Okubo M, Hosono E, Kim J, Enomoto M, Kojima N, Kudo T*, et al.* Nanosize effect on high-rate Li-ion intercalation in LiCoO2 electrode. *J Am Chem Soc* 2007, **129**(23)**:** 7444-7452.

47. Yang LC, Gao QS, Tang Y, Wu YP, Holze R. MoO2 synthesized by reduction Of MoO3 with ethanol vapor as an anode material with good rate capability for the lithium ion battery. *J Power Sources* 2008, **179**(1)**:** 357-360.

48. Shi YF, Guo BK, Corr SA, Shi QH, Hu YS, Heier KR*, et al.* Ordered Mesoporous Metallic MoO2 Materials with Highly Reversible Lithium Storage Capacity. *Nano Lett* 2009, **9**(12)**:** 4215-4220.

49. Guo BK, Fang XP, Li B, Shi YF, Ouyang CY, Hu YS*, et al.* Synthesis and Lithium Storage Mechanism of Ultrafine MoO2 Nanorods. *Chem Mater* 2012, **24**(3)**:** 457-463.

50. Conway BE. Transition from Supercapacitor to Battery Behavior in Electrochemical Energy-Storage. *J Electrochem Soc* 1991, **138**(6)**:** 1539-1548.

51. Auborn JJ, Barberio YL. Lithium Intercalation Cells without Metallic Lithium - Moo2/Licoo2 and Wo2/Licoo2. *J Electrochem Soc* 1987, **134**(3)**:** 638-641.

52. Dahn JR, Mckinnon WR. Structure and Electrochemistry of Lixmoo2. *Solid State Ionics* 1987, **23**(1-2)**:** 1-7.

53. Ku JH, Jung YS, Lee KT, Kim CH, Oh SM. Thermoelectrochemically Activated MoO2 Powder Electrode for Lithium Secondary Batteries. *J Electrochem Soc* 2009, **156**(8)**:** A688-A693.

54. Bruce PG, Scrosati B, Tarascon JM. Nanomaterials for rechargeable lithium batteries. *Angew Chem Int Ed* 2008, **47**(16)**:** 2930-2946.

55. Arico AS, Bruce P, Scrosati B, Tarascon JM, Van Schalkwijk W. Nanostructured materials for advanced energy conversion and storage devices. *Nature Mater* 2005, **4**(5)**:** 366-377.

56. Andersson A, Hansen S. Ammoxidation of Toluene over Molybdenum Oxides. *Catal Lett* 1988, **1**(11)**:** 377-383.

57. Sloczynski J. Kinetics and Mechanism of Molybdenum(Vi) Oxide Reduction. *J Solid State Chem* 1995, **118**(1)**:** 84-92.

58. Ellefson CA, Marin-Flores O, Ha S, Norton MG. Synthesis and applications of molybdenum (IV) oxide. *J Mater Sci* 2012, **47**(5)**:** 2057-2071.

59. Cook JB, Kim C, Xu LP, Cabana J. The Effect of Al Substitution on the Chemical and Electrochemical Phase Stability of Orthorhombic LiMnO2. *J Electrochem Soc* 2013, **160**(1)**:** A46-A52.

60. Gibot P, Casas-Cabanas M, Laffont L, Levasseur S, Carlach P, Hamelet S*, et al.* Room-temperature single-phase Li insertion/extraction in nanoscale Li(x)FePO(4). *Nature Mater* 2008, **7**(9)**:** 741-747.

61. Whittingham MS. Lithium batteries and cathode materials. *Chem Rev* 2004, **104**(10)**:** 4271-4301.

62. Hummers WS, Offeman RE. Preparation of Graphitic Oxide. *J Am Chem Soc* 1958, **80**(6)**:** 1339-1339.

63. Cote LJ, Kim F, Huang JX. Langmuir-Blodgett Assembly of Graphite Oxide Single Layers. *J Am Chem Soc* 2009, **131**(3)**:** 1043-1049.

64. Tolbert SH, Alivisatos AP. Size Dependence of a First-Order Solid-Solid Phase-Transition - the Wurtzite to Rock-Salt Transformation in Cdse Nanocrystals. *Science* 1994, **265**(5170)**:** 373-376.

65. Wagemaker M, Borghols WJH, Mulder FM. Large impact of particle size on insertion reactions. A case for anatase LixTiO2. *J Am Chem Soc* 2007, **129**(14)**:** 4323-4327.

66. Liu TC, Pell WG, Conway BE, Roberson SL. Behavior of molybdenum nitrides as materials for electrochemical capacitors - Comparison with ruthenium oxide. *J Electrochem Soc* 1998, **145**(6)**:** 1882-1888.

67. Wang J, Polleux J, Lim J, Dunn B. Pseudocapacitive contributions to electrochemical energy storage in TiO2 (anatase) nanoparticles. *J Phys Chem C* 2007, **111**(40)**:** 14925-14931.

68. Sun YM, Hu XL, Yu JC, Li Q, Luo W, Yuan LX, *et al.* Morphosynthesis of a hierarchical MoO2 nanoarchitecture as a binder-free anode for lithium-ion batteries. *Energy Environ Sci* 2011, **4**(8)**:** 2870-2877.

69. Liu B, Zhao XY, Tian Y, Zhao D, Hu CW, Cao MH. A simple reduction process to synthesize MoO2/C composites with cage-like structure for high-performance lithium-ion batteries. *Phys Chem Chem Phys* 2013, **15**(22)**:** 8831-8837.

70. Sun YM, Hu XL, Luo W, Huang YH. Self-Assembled Hierarchical MoO2/Graphene Nanoarchitectures and Their Application as a High-Performance Anode Material for Lithium-Ion Batteries. *ACS Nano* 2011, **5**(9)**:** 7100-7107.

71. Ji XL, Herle S, Rho YH, Nazar LF. Carbon/MoO2 composite based on porous semi-graphitized nanorod assemblies from in situ reaction of tri-block polymers. *Chem Mater* 2007, **19**(3)**:** 374-383.

72. Han PX, Ma W, Pang SP, Kong QS, Yao JH, Bi CF, *et al.* Graphene decorated with molybdenum dioxide nanoparticles for use in high energy lithium ion capacitors with an organic electrolyte. *J Mater Chem A* 2013, **1**(19)**:** 5949-5954.

73. Zhou Y, Bao QL, Tang LAL, Zhong YL, Loh KP. Hydrothermal Dehydration for the "Green" Reduction of Exfoliated Graphene Oxide to Graphene and Demonstration of Tunable Optical Limiting Properties. *Chem Mater* 2009, **21**(13)**:** 2950-2956.

74. Eigler S, Dotzer C, Hirsch A. Visualization of defect densities in reduced graphene oxide. *Carbon* 2012, **50**(10)**:** 3666-3673.

75. Kudin KN, Ozbas B, Schniepp HC, Prud'homme RK, Aksay IA, Car R. Raman spectra of graphite oxide and functionalized graphene sheets. *Nano Lett* 2008, **8**(1)**:** 36-41.

76. Chen G, Rodriguez R, Fei L, Xu Y, Deng SG, Smirnov S*, et al.* A facile hydrothermal route to iron(III) oxide with conductive additives as composite anode for lithium ion batteries. *J Power Sources* 2014, **259:** 227-232.

77. Nursanto EB, Nugroho A, Hong SA, Kim SJ, Chung KY, Kim J. Facile synthesis of reduced graphene oxide in supercritical alcohols and its lithium storage capacity. *Green Chem* 2011, **13**(10)**:** 2714-2718.

78. Doeff MM, Ma YP, Visco SJ, Dejonghe LC. Electrochemical Insertion of Sodium into Carbon. *J Electrochem Soc* 1993, **140**(12)**:** L169-L170.

79. Jow TR, Shacklette LW, Maxfield M, Vernick D. The Role of Conductive Polymers in Alkali-Metal Secondary Electrodes. *J Electrochem Soc* 1987, **134**(7)**:** 1730-1733.

80. Ma YP, Doeff MM, Visco SJ, Dejonghe LC. Rechargeable Na Naxcoo2 and Na15pb4 Naxcoo2 Polymer Electrolyte Cells. *J Electrochem Soc* 1993, **140**(10)**:** 2726-2733.

81. Stevens DA, Dahn JR. High capacity anode materials for rechargeable sodium-ion batteries. *J Electrochem Soc* 2000, **147**(4)**:** 1271-1273.

82. Okada ST, Y.; Kiyabu, T.; Doi, T.; Yamaki, J.-I.;, Nishida T. Layered transition metal oxides as cathodes for sodium secondary battery. *210th ECS Meeting Abstracts* 2006, **MA2006**(2)**:** 201.

83. Sauvage F, Quarez E, Tarascon JM, Baudrin E. Crystal structure and electrochemical properties vs. Na+ of the sodium fluorophosphate Na1.5VOPO4F0.5. *Solid State Sci* 2006, **8**(10)**:** 1215-1221.

84. Serras P, Palomares V, Goni A, Kubiak P, Rojo T. Electrochemical performance of mixed valence Na3V2O2x(PO4)(2)F3-2x/C as cathode for sodium-ion batteries. *J Power Sources* 2013, **241:** 56-60.

85. Serras P, Palomares V, Kubiak P, Lezama L, Rojo T. Enhanced electrochemical performance of vanadyl (IV) Na-3(VO)(2)(PO4)(2)F by ex-situ carbon coating. *Electrochem Commun* 2013, **34:** 344-347.

86. Bianchini M, Brisset N, Fauth F, Weill F, Elkaim E, Suard E*, et al.* Na3V2(PO4)(2)F-3 Revisited: A High-Resolution Diffraction Study. *Chem Mater* 2014, **26**(14)**:** 4238-4247.

87. Sharma N, Serras P, Palomares V, Brand HEA, Alonso J, Kubiak P*, et al.* Sodium Distribution and Reaction Mechanisms of a Na3V2O2(PO4)(2)F Electrode during Use in a Sodium-Ion Battery. *Chem Mater* 2014, **26**(11)**:** 3391-3402.

88. Jiang T, Chen G, Li A, Wang CZ, Wei YJ. Sol-gel preparation and electrochemical properties of Na3V2(PO4)(2)F-3/C composite cathode material for lithium ion batteries. *J Alloys Compd* 2009, **478**(1-2)**:** 604-607.

89. Park YU, Seo DH, Kwon HS, Kim B, Kim J, Kim H*, et al.* A New High-Energy Cathode for a Na-Ion Battery with Ultrahigh Stability. *J Am Chem Soc* 2013, **135**(37)**:** 13870-13878.

90. Aono H, Imanaka N, Adachi G. High Li+ Conducting Ceramics. *Acc Chem Res* 1994, **27**(9)**:** 265-270.

91. Cushing BL, Goodenough JB. Li2NaV2(PO4)(3): A 3.7 V lithium-insertion cathode with the rhombohedral NASICON structure. *J Solid State Chem* 2001, **162**(2)**:** 176-181.

92. Goodenough JB, Hong HYP, Kafalas JA. Fast Na+-Ion Transport in Skeleton Structures. *Mater Res Bull* 1976, **11**(2)**:** 203-220.

93. Manthiram A, Goodenough JB. Lithium Insertion into Fe2(So4)3 Frameworks. *J Power Sources* 1989, **26**(3-4)**:** 403-408.

94. Zhang SS. A review on electrolyte additives for lithium-ion batteries. *J Power Sources* 2006, **162**(2)**:** 1379-1394.

95. Zhang SS. The effect of the charging protocol on the cycle life of a Li-ion battery. *J Power Sources* 2006, **161**(2)**:** 1385-1391.

96. Komaba S, Mikumo T, Yabuuchi N, Ogata A, Yoshida H, Yamada Y. Electrochemical Insertion of Li and Na Ions into Nanocrystalline Fe3O4 and alpha-Fe2O3 for Rechargeable Batteries. *J Electrochem Soc* 2010, **157**(1)**:** A60-A65.

97. McMillan R, Slegr H, Shu ZX, Wang WD. Fluoroethylene carbonate electrolyte and its use in lithium ion batteries with graphite anodes. *J Power Sources* 1999, **81:** 20-26.

98. Kobayashi M, Inoguchi T, Iida T, Tanioka T, Kumase H, Fukai Y. Development of direct fluorination technology for application to materials for lithium battery. *J Fluorine Chem* 2003, **120**(2)**:** 105-110.

99. Wrodnigg GH, Besenhard JO, Winter M. Ethylene sulfite as electrolyte additive for lithium-ion cells with graphitic anodes. *J Electrochem Soc* 1999, **146**(2)**:** 470-472.

100. Komaba S, Ishikawa T, Yabuuchi N, Murata W, Ito A, Ohsawa Y. Fluorinated Ethylene Carbonate as Electrolyte Additive for Rechargeable Na Batteries. *ACS Appl Mater Inter* 2011, **3**(11)**:** 4165-4168.

101. Song J, Xu MW, Wang L, Goodenough JB. Exploration of NaVOPO4 as a cathode for a Na-ion battery. *Chem Comm* 2013, **49**(46)**:** 5280-5285.

102. Serras P, Palomares V, Rojo T, Brand HEA, Sharma N. Structural evolution of high energy density V3+/V4+ mixed valent Na3V2O2x(PO4)(2)F3-2x (x=0.8) sodium vanadium fluorophosphate using in situ synchrotron X-ray powder diffraction. *J Mater Chem A* 2014, **2**(21)**:** 7766-7779.

103. Nakai H, Kubota T, Kita A, Kawashima A. Investigation of the Solid Electrolyte Interphase Formed by Fluoroethylene Carbonate on Si Electrodes. *J Electrochem Soc* 2011, **158**(7)**:** A798-A801.

104. Komaba S, Murata W, Ishikawa T, Yabuuchi N, Ozeki T, Nakayama T*, et al.* Electrochemical Na Insertion and Solid Electrolyte Interphase for Hard-Carbon Electrodes and Application to Na-Ion Batteries. *Adv Funct Mater* 2011, **21**(20)**:** 3859-3867.

105. Barpanda P, Oyama G, Nishimura S, Chung SC, Yamada A. A 3.8-V earth-abundant sodium battery electrode. *Nat Commun* 2014, **5**.

106. Jiang Y, Yang ZZ, Li WH, Zeng LC, Pan FS, Wang M*, et al.* Nanoconfined Carbon-Coated Na3V2(PO4)(3) Particles in Mesoporous Carbon Enabling Ultralong Cycle Life for Sodium-Ion Batteries. *Adv Energy Mater* 2015, **5**(10).

107. Yu CY, Park JS, Jung HG, Chung KY, Aurbach D, Sun YK*, et al.* NaCrO2 cathode for high-rate sodium-ion batteries. *Energy Environ Sci* 2015, **8**(7)**:** 2019-2026.

108. Oh SM, Myung ST, Yoon CS, Lu J, Hassoun J, Scrosati B*, et al.* Advanced Na[Ni0.25Fe0.5Mn0.25]O-2/C-Fe3O4 Sodium-Ion Batteries Using EMS Electrolyte for Energy Storage. *Nano Lett* 2014, **14**(3)**:** 1620-1626.